DEVELOPMENT OF AN IN VITRO TBI MODELS AND VALIDATION OF NANODELIVERY FOR RESTORATION OF DISRUPTED BRAIN ENDOTHELIUM

By

EDIDIONG INWANG INYANG

DISSERTATION

Submitted in partial fulfillment of the requirements

for the degree of Doctor of Philosophy at

The University of Texas at Arlington

August 2019

Arlington, Texas

Supervising Committee:

Michael Cho, Supervising Professor
Kytai Nguyen
Yi Hong
Young-Tae Kim
Eileen Clements

Table of Contents

ACKNOWLEDGMENT

My gratitude to goes to my advisor Dr. Michael Cho (Prof.), for his persistent help, supervision, guidance, patience, and understanding during my Ph.D. study, research, and in the writing of this dissertation. I am indeed grateful for his support.

I want to thank my dissertation committee members, (Drs. Kytai Nguyen, Yi Hong, Young-Tae Kim, and Eileen Clements) for their excellent advice, suggestions, and insights. I would also like to thank Dr. Vinay Abhyankar for his help with fabricating the in vitro culture device.

Also, I would like to thank the directors and staff of the Louis Stokes Alliance for Minority Participation Bridge to doctorate (LSAMP – BD) program for their financial and academic support.

I thank Dr. Bo Chen, Research assistant professor, for his training on microcavitation, which is the core of my research. Thanks to my lab mates (Caleb Liebman, Andrew McColloch and Annie Phillips) for their great support and encouragement. I also want to thank my colleagues, Linda Noukeu Njiki, Qionghua Shen, and Aneetta Kuriakose for their help when needed. In particular, Aneetta in the Nguyen laboratory provided me with the necessary training to produce, characterize, and manipulate nanoparticles. Cortical neuron isolation and culture would not have been possible without the generous assistance from Dr. Kim.

Additionally, I would like to thank the staff of the Bioengineering department for their help throughout my graduate study.

Lastly, I thank my family and friends for their support and understanding all these years.

DEDICATION

I dedicate this dissertation to God, who is the source of my strength and inspiration.

I also dedicate this work to my beloved parents Michael and Petronilla Isemin for their love, patience, support, kindness, and above all for selling their lands to sponsor me to the United States for higher learning.

LIST OF FIGURES

x

LIST OF TABLES

LIST OF ABBREVIATIONS

BBB …………………………………………………………. Blood-brain barrier

TBI……………………………………………………………Traumatic brain injury

BECs…………………………………………………………… Brain endothelial cells

ZO-1…………………………………………………………….. Zonular occludin

PSDs ………………………………………………………… Psychostimulants drugs

GLUT1……………………………………………………………. Glucose transporter 1

MMPs……………………………………………………………Matrix metalloproteinases

TNF-α……………………………………………………………Tumor necrotic factor-alpha

NPs……………………………………………………………Nanoparticles

ABSTRACT

DEVELOPMENT OF IN VITRO TBI MODELS AND VALIDATION OF NANODELIVERY

FOR RESTORATION OF DISRUPTED BRAIN ENDOTHELIUM

EDIDIONG INWANG INYANG

The University of Texas at Arlington, 2019

Supervising Professor: Dr. Michael Cho

Blast-induced traumatic brain injury (bTBI) is a serious concern among military personnel and their families. Although the mechanisms responsible for disruption to the brain are not well understood, the development of reliable diagnosis along with effective therapeutic treatment is urgently warranted. Recent findings suggest that shockwaves produced by a blast can generate micron-size bubbles that subsequently collapse in the brain tissue. The collapse of microbubbles (referred to as microcavitation) may compromise the integrity of the blood-brain barrier (BBB). Moreover, addiction to the psycho-stimulant drugs (PSDs), e.g. cocaine and alcohol which are known to cause toxicity due to oxidative stress, can also adversely affect the BBB. One specific mechanism that has been proposed postulates the brain endothelium is compromised by traumatic events and therefore, the biotransport properties across the BBB are modulated. The injured brain endothelial cells (BECs) appear to express a high level of E-Selectins (CD62e), which typically indicates inflammation and activation of endothelial cells. Upregulation of this protein following a traumatic injury can be exploited for diagnosis and potential therapy through targeted drug nanodelivery. We, therefore, hypothesized that the collapsed microbubbles in the blood vessel and psychostimulants can modulate its structure and function, alter the glucose uptake and transport, and disrupt the energy requirement of the BBB as well as neurons. To test and validate this hypothesis, we applied tissue engineering techniques to fabricate a custom-designed cell culture chamber to mimic the structure and biotransport properties of the BBB and used it as a model to determine the effect of microcavitation and PSDs on the physical, mechanical, chemical, and biological changes in the brain endothelium and neurons. We also engineered

nanoparticles that are (1) decorated with ligands to specifically bind the injured endothelial cells; and (2) loaded with therapeutic reagents (e.g., poloxamers and antioxidant) to facilitate restoration of BECs. In summary, engineering a biomimetic interface is proven to provide a systematic approach to replicate the structure and function of BBB and determine its alteration in response to mechanical and chemical traumas to the brain.

Chapter 1
1.1   INTRODUCTION

1.1.1   The blood-brain barrier

The blood-brain barrier (BBB) is a selective barrier that is formed by the brain endothelial cells that line blood vessels [1]. Because of the complex tight junctions between adjacent endothelial cells, it plays the role of a physical barrier controlling transcellular and paracellularly transport [2]. Gaseous molecules like O_2 and CO_2, small lipophilic agents, and ethanol can diffuse freely through the lipid membranes, but transcellular transport of small hydrophilic molecules are regulated (e.g., selectivity) [1]. Specific receptor-mediated transcytosis or less specific adsorptive mediated transcytosis may be the mechanism through which large hydrophilic molecules (peptides and proteins) can be transported [3]. It is worth noting that brain endothelium has a lower degree of transcytosis and endocytosis activity than does peripheral endothelium. Therefore, the blood-brain barrier covers a range of passive and active features of the brain endothelium. The BBB is a dynamic system, and its permeability and transport properties have been shown to be modulated either biochemically or mechanically.

1.1.2   Functions of the BBB

The BBB supplies the brain with essential nutrients and mediates transport of many waste products, separate the pools of neurotransmitters and neuroactive agents that act centrally (in the CNS) and peripherally (in the peripheral tissues and blood), controls fluid and ionic movements between the blood and the brain, more importantly, the BBB protects the brain from fluctuations in ionic composition that can occur after a meal or exercise [4]. The major role of brain endothelium is to regulate the brain microenvironment. The BBB is a vascular structure that separates the central nervous system (CNS) from the peripheral blood circulation. Influx and efflux are actively regulated at the blood-brain interface by tightly controlling the passage of molecules and ions, instantaneously delivering nutrients and oxygen according to current neuronal needs and protecting the brain from toxins and pathogens. As such the BBB maintains an environment that allows neurons to function properly.

1.1.3 The BBB phenotype

The core anatomical element of the BBB is the cerebral blood vessel formed by endothelial cells (ECs). ECs of the BBB are unique compared to other ECs in different tissues. For example, they have continuous intercellular tight junctions (TJs), lack fenestrations and undergo extremely low rates of transcytosis, which greatly limits both the paracellular and transcellular movement of molecules through the EC layer [5, 6]. Passage of molecules through the BBB is regulated by a series of specific transporters, which allow delivery of nutrients to the brain and extrusion of potential toxins. ECs also have low expression of leukocyte adhesion molecules, abrogating immune cell infiltration into the healthy CNS [7]. The main features of the brain endothelium that contribute to its barrier properties is the tight junctions. Tight junctions are complex structures of the network in the brain endothelium, formed by intramembranous particles and it significantly restricts the movement of ions such as Na^+ and Cl^-, to keep the trans-endothelial electrical resistance (TEER) >1,000 ohms/cm^2 [8]. The transmembrane proteins that make important contributions to tight junction structure include zonula occludens protein 1 (ZO-1), Occludin, and the claudins. They all contribute to the high TEER level of the brain endothelium [9]. Junctional adhesion molecules JAM-A, JAM-B, and JAM-C are also involved in the formation and maintenance of the endothelium tight junctions.

There are other proteins that form complexes within the tight junctions and mediate the cell-to-cell interactions and anchor tight junction proteins to the cytoskeleton. These include, the adaptor proteins, such as, ZO-2 and ZO-3; the partitioning defective proteins PAR3 and PAR6; and MUPP1 (multi-PDZ-protein 1); the Ca^{2+}-dependent serine protein kinase (CASK); MAGI-1, MAGI-2 and MAGI-3 (membrane-associated guanylate kinase with inverted orientation of protein-protein interaction domains); regulatory and signaling molecules (including the small GTPases) and their regulators, such as the regulator of G-protein signaling 5 (RGS5), and the transcription regulator the ZO-1-associated nucleic acid-binding protein (ZONAB).

Function of the tight junction is not limited to only restricting the paracellular permeability, but also in separating the apical and basal domains of the cell membrane, which allows the endothelium to maintain polarized (apical-basal) properties [10]. The PAR3 and PAR6 complex are speculated to be involved in regulating the formation of tight junction in

establishing cell polarity. GLUT1 glucose carrier, including LAT1, and transporters for nucleosides are the brain endothelial transporters that supply the brain with nutrients [1]. GLUT1 and LAT1 are bidirectional, moving substrates down the concentration gradient, and can be present on both the luminal and abluminal membranes. The energy may come from ATP when molecules or compounds are moved against a concentration gradient. GLUT1 is brain endothelial and facilitates the transport of glucose from the circulation into the brain. It has the highly glycosylated 55 kDa GLUT1 and the less glycosylated 45 kDa GLUT1 isoforms [11] and is localized 11% in the luminal, 45% in the intracellular pool, and 44% in the abluminal side of the microvessel [12]. The BBB exists at all levels of the vasculature within the CNS, including the penetrating arteries and arterioles, the dense capillary bed, the postcapillary venules, and the draining venules and veins [13] and there are specializations within the vascular bed that are crucial for BBB function, such as nutrient transport that is highly specialized to the capillaries that come in close proximity of neurons and postcapillary venule regulate leukocyte trafficking and immune modulation [14, 15].

1.2   BBB alteration by biochemical and mechanical induction

Cellular and non-cellular elements that interact with the ECs controls the development and maintenance of the BBB. Astrocytes, pericytes and extracellular matrix (ECM) components provide both structural and functional support to the BBB. Neurovascular unit (NVU) (neurons, microglial cells and, optionally, peripheral immune cells) are all contributing to the BBB [5, 16] (Fig. 1.1). The abluminal surface of brain capillaries is covered by a basement membrane that separates ECs from pericytes and astrocytes [17]. There are different ways that the function of the BBB can be altered. Either biochemically or mechanically, it involves disturbances of endothelial cell-cell interaction. Thus, leading to leakier endothelium than those of normal brain tissue. The endothelium disturbance involves the up-regulation of MMPs and downregulation of tight junction proteins (ZO-1) and GLUT1. The release of different inflammatory agents during inflammation, leads to an increased permeability of the brain endothelium. The activation of brain endohelium leads to the release of interleukin-6 (IL-6), which can amplify the effect by acting back on the endothelium [18]. Tumor necrosis factor-α (TNFα) can also increase BBB permeability directly on the endothelium [19] or by indirectly affecting the

production of endothelial endothelin 1 and IL-1β [20]. An example of mechanical disruption of the BBB that is the focus of this thesis is the formation of micron-size bubbles in the brain induced by exposure to a blast. These transient and unstable microbubbles are formed as the shock waves propagate through a liquid medium [63], and when they collapse (i.e., microcavitation), they produce secondary but localized shock waves (known as microjets, [60]) that are capable of causing necrotic cell death and apoptosis. Microcavitation is postulated as a plausible biophysical mechanism by which tight junctions are modulated and its functions are disrupted. Dysfunctional tight junctions can also result in an imbalance of ions, transmitters, and metabolic products in the interstitial fluid, causing abnormal neuronal activity and seizures (Fig. 1.2). Brain disorders such as epilepsy can manifest from repeated seizures over time. It is also noted that seizures can also occur in other neurological disorders that are characterized by a compromised BBB, including stroke, CNS infections, and neurodegenerative diseases [21].
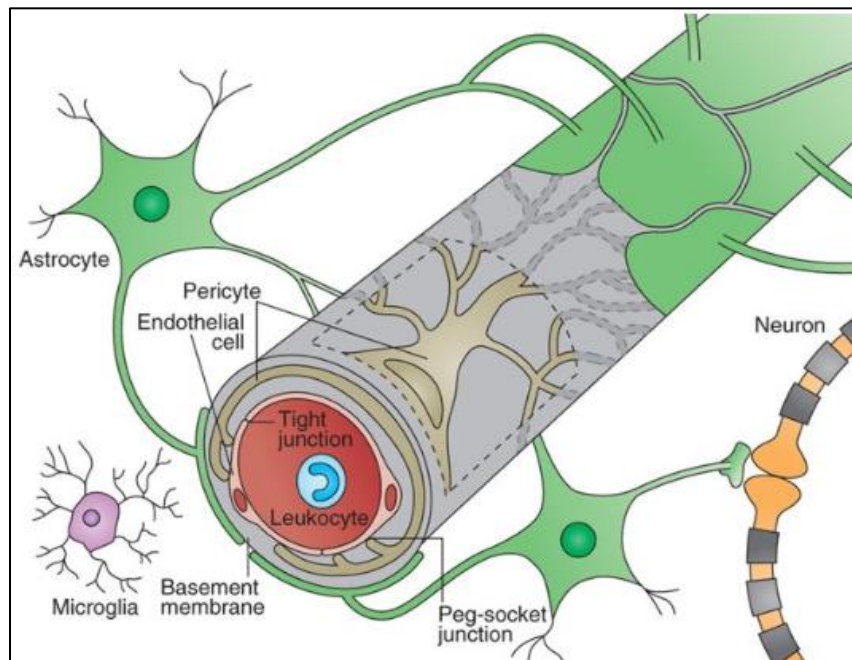
Figure 1. 1 - Schematics showing vascular endothelial cells sealed by tight junctions and basement membrane separating the luminal and abluminal sections of the blood vessel. Pericytes, astrocytes and their processes are in direct contact with endothelial cells.
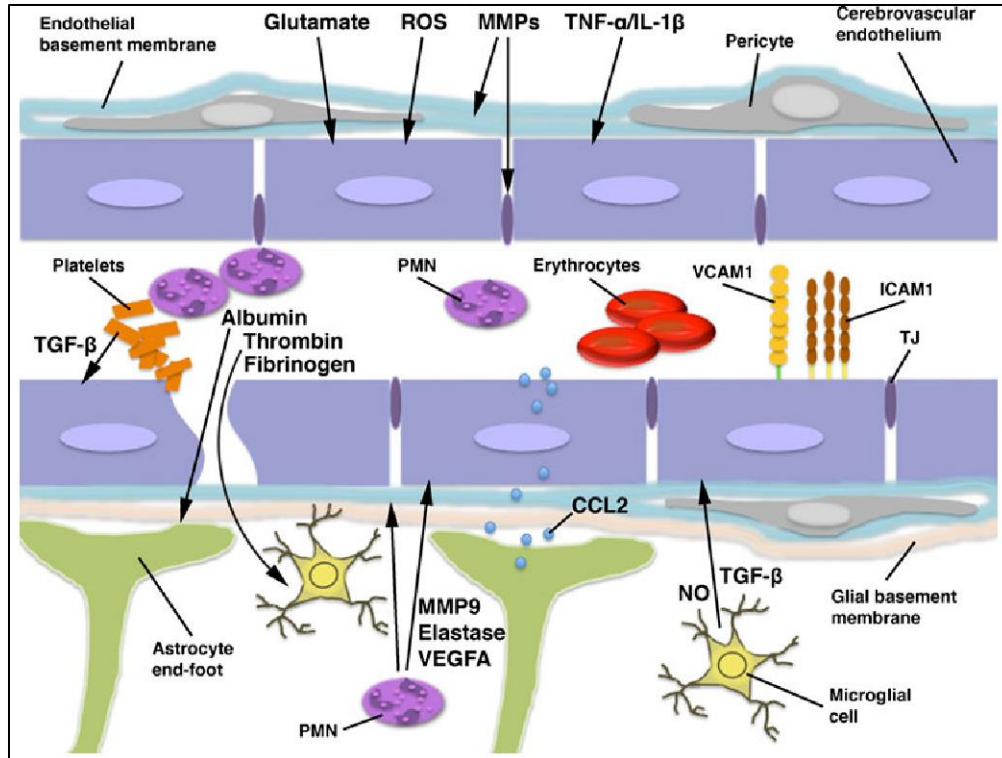
Figure 1. 2 - Schematic representation of injured blood-brain barrier (BBB). Tight junctions are disrupted, and permeability is increased. Chodobski et al., [31].

1.3   In Vitro Models

Transwells (Corning Inc., Corning, NY) are the most commonly used in vitro models [22, 23]. It allows the use of one or more cell types, with endothelial cells cultured in the upper (luminal) compartment of the Transwell and either astrocytes or pericytes cultured on the lower (abluminal) side of the membrane, providing a suitable technique to develop an in vitro model to study the effects of microcavitation. There are different sources of endothelial cells and cell lines, and human umbilical vascular endothelial cells are often used. However, they result in low TEER and high permeability. Brain-derived endothelial cells, on the other hand, will retain some of their BBB phenotypic expressions. Human brain microvascular endothelial cells (HBMECs) have been shown to give the best barrier properties for permeability studies using Transwells [24]. There are some advantages to using immortalized animal cell lines, which includes the ease of culture and increased fidelity of the in vitro models [25]. The major drawback of using such cell cultures is

that they lose some of their phenotypic expressions with each passage, resulting in weakened tight junctions.

In vitro models can be engineered to mimic the BBB and adequately represent the functional and physiological features found in the BBB. A tissue engineered platform can be designed to study in detail the BBB-related responses in normal and pathological states. The platform may also be utilized to screen the potential therapeutic treatments to minimize or reverse the adverse effects caused by microcavitation and other traumas to the brain. The model is expected to possess a realistic tissue architecture, display the functional expression of tight junctions, and should be easy to engineer and handle [26]. In recent years, there have been many introductions of improved cell culture models for BBB, and some even advocating coculture [27, 28]. However, both financial burdens and laborious procedures often impose limiting factors for easily producing these models. An overview of the advantages and disadvantages of some of the models currently in use are summarized in Table 1.

Table 1 - Advantages and limitations of commonly used in vitro BBB models

Models	Advantages	Limitations	References
Trans-well system	1. Cost and time effective 2. Easy to control	1. Suited for short term culture only 2. Loses BBB characteristics quickly 3. Mechanism responsible for traumatic brain injury cannot be studied	183
Microfluidic system	1. Application of shear stress 2. Mimics structural and functional features of BBB	1. Requires technical skills 2. It is expensive 3. Mechanism responsible for traumatic brain injury cannot be studied	184
Brain micro-vessels	1. Mimics structural and functional features of BBB 2. It is well established	1. Difficult to isolate 2. Poor viability 3. Mechanism responsible for traumatic brain injury cannot be studied	185
Spheroids	1. No scaffold needed 2. 3-D cell organization	1. No application of shear stress 2. Limited control 3. Mechanism responsible for traumatic brain injury cannot be studied	185, 186

Despite the strict behavior of the BBB in restricting of particles across the BBB, it can be compromised either biochemically, mechanically, or both. There are a couple of techniques that have been applied to mimic mechanical TBI, including the use of ultrasound, microcavitation, and even in the combination of both [29, 30]. Blast-induced microcavitation can mechanically depict TBIs that are caused by explosive blasts on the battle field, for example, and blunt force. Therefore, engineering a controllable biosystem to model such traumatic events to the brain is expected to advance the current understanding in TBI. In this thesis, we have induced microcavitation by creating a controlled blast. The approach has been proven to mimic the blast-induced TBI, characterize the effects on the brain endothelium, and validate a few therapeutic treatments. Most TBI injuries go undiagnosed, and by the time the symptoms are detected, effective treatments are lacking. One of the main concerns is on-time diagnosis and targeted treatment. Most treatment regimens are not targeted therefore drug targeting to the brain by circumventing the physiological barriers is a prerequisite for drugs acting on the central nervous system (CNS) and therapeutic potential of many drugs can be improved by effectively targeting injury sites.

1.4   Targeting compromised BBB

The brain endothelial cells (BECs) represent a therapeutic target. The type of proteins that are activated in the brain endothelial cells during injury or inflammation needs to be considered in developing drug delivery strategies to target sites in the brain in treating BBB disruptions. The idea is to reduce, halt, or reverse BBB dysfunction. Polymers such as poloxamer 188 (P188) are widely used to seal leaking cells (Fig. 1.3) and are FDA approved. Among its other uses are as an emulsifier for artificial blood and as an anticoagulant in the microcirculation [32]. It is also a known surfactant and wetting agent for antibiotics [33]. It is now known that P188 can improve the barrier function not only by restoring the brain endothelial tight junctions but also by upregulating ZO-1, GLUT 1, and downregulating MMP-2&9 (see below). This implies that brain endothelium is a target for drug action on BBB. Another drug with excellent therapeutic applications that would work well in combination with P188 is N-acetylcysteine (NAC), which has been used as an antioxidant to decrease the membrane damage by superoxide-generating systems and diminishes endotoxin [34]. It was also approved by the FDA to be used as an

7

antioxidant precursor to glutathione (γ-glutamylcysteinylglycine; GSH) in the treatment of paracetamol overdose [35] (Fig. 1.4).
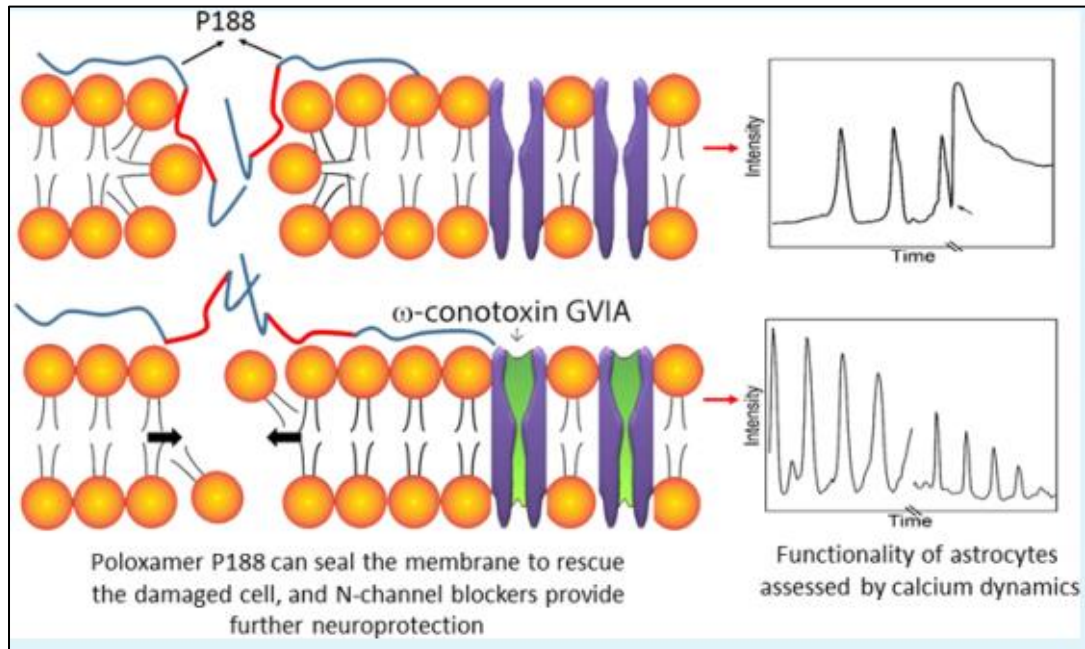
Figure 1. 3 - Schematics showing the integration of poloxamer 188 into the damaged astrocyte cell membrane to restore calcium spiking. Chen et al., [118].
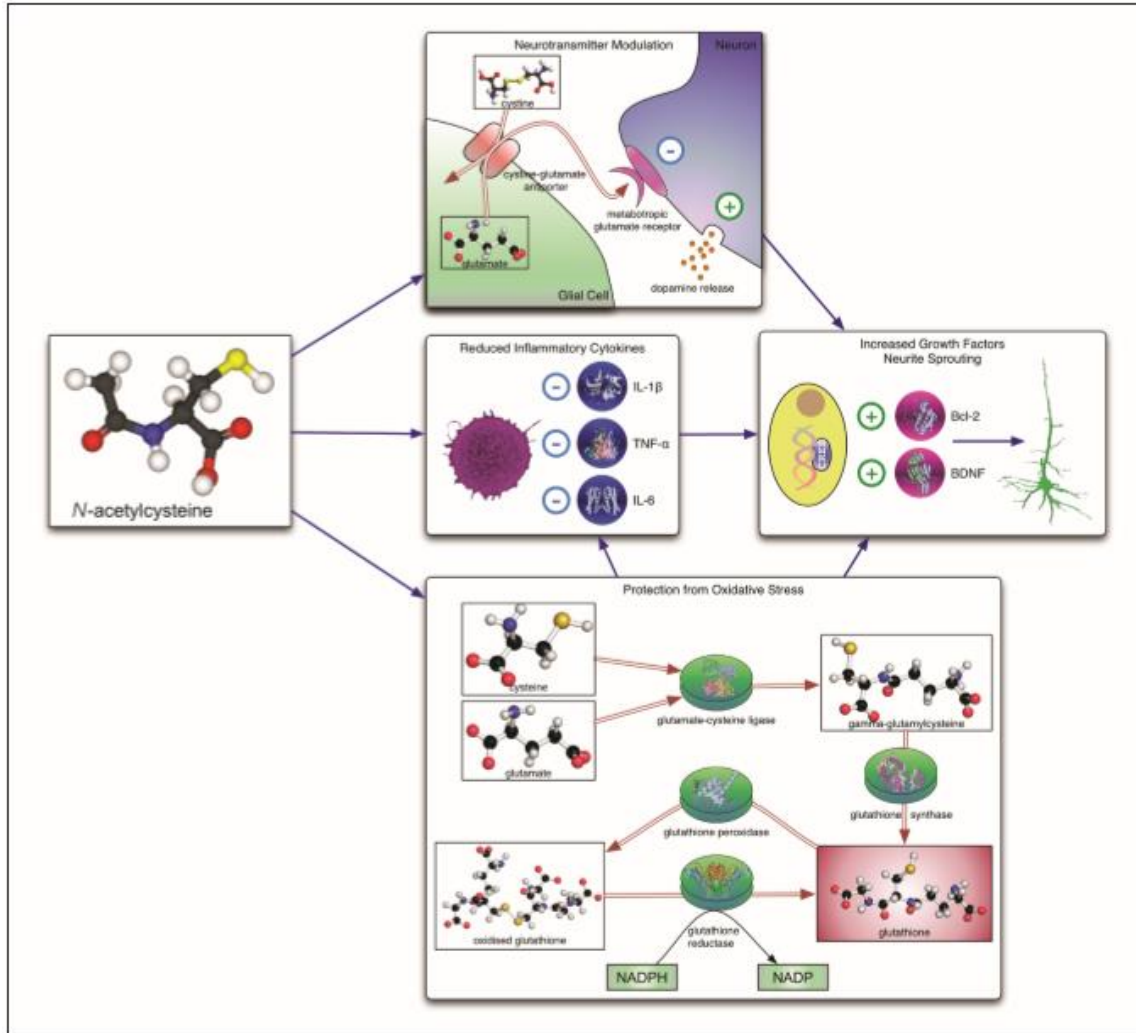
Figure 1. 4 - Schematics of mechanisms of action of N-acetylcysteine (NAC). Top to bottom: increased activity of cysteine–glutamate antiporter results in increased activation of metabotropic glutamate receptors on inhibitory neurons and facilitates vesicular dopamine release; NAC reduces inflammatory cytokines and acts as a substrate for glutathione synthesis. Dean et al., [34]

Differential display technologies are used to establish genes upregulated in diseased/injured brain endothelium [36]. These upregulated genes are great targets for therapy, but caution is needed because some of the genes are upregulated for the defensive mechanism. Also, some agents have different roles in various phases or stages of the disease, injury, or inflammation. They could be destructive at an earlier stage and protective at a later stage and vice versa. For example, VEGF, which increases brain endothelial permeability when given intravenously, is neuroprotective and reduces BBB leakage after ischemia when given intraventricularly [37]. The cytokine erythropoietin (a major regulator of erythropoiesis) is protective against brain injury *in vivo* and protects cultured neurons against toxicity [38];

9

moreover, it protects the brain endothelium against VEGF-induced permeability by reducing the level of endothelial nitric oxidase synthase (eNOS) and restoring junctional proteins [39]. There is a need to evaluate the performance of the current cell-based in vitro systems of the BBB and standardize the method of evaluating the mechanism responsible for BECs disruption. A thorough investigation of the mechanisms involved in the endothelial cell-cell interaction will help in the design of therapies targeted at specific features necessary for BBB function (Fig. 1.5). We also need a better understanding of cellular proteomics and metabolism to devise additional targeted therapies for the BBB. Improved techniques to image with high resolution and monitor the functions of the living brain will also accelerate the development of potential treatments.
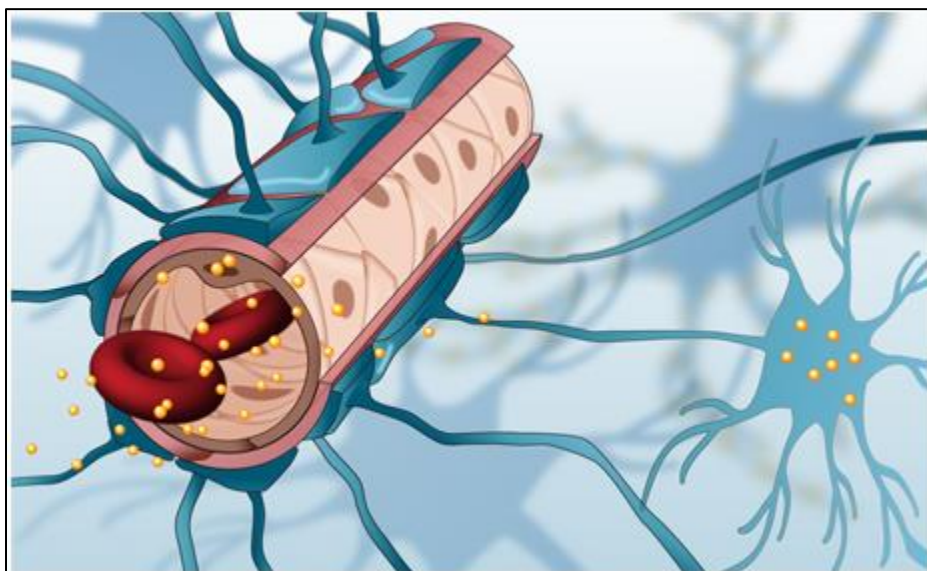
Figure 1. 5 - Schematics of nanoparticles penetrating the blood-brain barrier for targeted delivery. Researchers at DTU Nanotech.

1.5   <u>Overview of Research Project</u>

The goal of the research project is to establish in vitro models to characterize and elucidate the mechanisms mediating disruption of the brain endothelium in response to blast-induced traumatic brain injury (bTBI). Using the same models, the effects of chemical traumas induced by psychostimulants (cocaine and alcohol) are also determined. Furthermore, theragnostic approaches

are engineered to specifically target the injured cells and to deliver therapeutic agents to treat the disrupted endothelium or neurons that are affected by the dysfunctional endothelium.

1.5.1   Objectives:

To investigate the mechanisms responsible for the disruption of brain endothelial cells (BECs) in response to blast-induced traumatic brain injury (bTBI) using an engineered cell culture chamber and blast exposure chamber. Specifically, BEC tight junction protein (ZO-1) will be quantified before and after blasts. Also, the theranostic approaches will be developed, validated, and applied to target, diagnose, and treat the disrupted tight junctions. The anticipated findings will aid in understanding the molecular mechanisms responsible for the compromised brain endothelium.

1.5.2   Hypotheses:

bTBIs can be caused by an explosive blast or blunt force to the head, but the mechanisms responsible for such injury is not well elucidated. However, it is well documented that a blast can generate microbubbles and the subsequent collapse of the bubbles (i.e., microcavitation) disrupts the BECs. Here, the hypothesis is that the collapse of microbubbles and addiction to psycho-stimulant drugs (PSDs), e.g., cocaine modulates the mechanical structure and physiological functions of BEC and that surfactants such as poloxamers (P188) in combination with NAC can attenuate the BEC disruption induced by bTBI.

1.5.3   Specific Research Aims:

1. **To develop and validate a cell culture device to study the effect of microcavitation on BECs.** Using microfabricated cell culture chambers and a permeable thin biopolymeric membrane (Polyester) that is easy to control to investigate the effect of microcavitation on BECs, measure the permeability of the brain endothelium and elucidate the role of matrix metalloproteinases in the tight junction degradation

2. **To investigate the structural and physiological role of GLUT-1 glucose transporter on brain endothelium barrier integrity and impact of abnormal glycemia on neurons.** Elucidating the BECs integrity and function and quantify the effects of hyperglycemic conditions on primary neurons.

3. **To encapsulate P188 and the combination of P188 + NA in PLGA nanoparticles to investigate the potential therapeutic treatment. Decorate the nanoparticles with PSGL-1 to target and stimulate proliferation and repair of brain endothelial tight junctions.** This aim is designed to be accomplished by targeting proteins that are upregulated in BECs after microcavitation and then treat the injured BECs with non-biologics. Successful outcome from the studies in this aim is expected to establish urgently needed alternate treatments for TBI.

Chapter 2

Aim 1: To develop and validate a cell culture device to study the effect of microcavitation on BECs.

2.1   INTRODUCTION

Traumatic brain injury (TBI) is one of the major causes of emergency visits and hospitalization. In 2010, the Centers for Disease Control (CDC) reported about 2.5 million emergency department visits, hospitalizations, and deaths here in the United States alone [40]. TBIs are also caused by explosive blast or blunt force to the head especially among those who serve in the U.S. military [41-43]. The trauma can lead to endothelial cell detachment, tight junction disruption, and blood-brain barrier (BBB) permeability [44, 45]. One of the unique features of BBB is the regulation of transport through a monolayer of brain endothelial cells (BECs). BECs are tightly regulated in their structure and function by tight junctions that are composed of, among many molecules, zonula occludens (ZO-1) and the Occludins family [46, 47]. Only particles with a molecular mass of fewer than 500 Daltons can cross the BBB efficiently [48]. However, the structural integrity of the BBB can be mechanically and biochemically compromised [49-52]. Harmful substances can extravasate into the brain through the compromised brain endothelium which, in turn, may lead to secondary brain injury [53-55] (Fig. 2.1). Small lipophilic molecules such as oxygen, CO_2, and ethanol can freely diffuse across the lipid membranes of the endothelium. Small polar solutes needed for brain function are transported by several specific carriers (e.g., GLUT-1 for glucose, L-system carrier L1 for large neutral amino acids such as leucine) and specific carriers mediate the efflux from the CNS of potentially toxic metabolites (e.g. glutamate) [56]. Anatomical examination of the brain microvasculature shows that the endfeet of astrocytic glia form a network of fine lamellae on the outer surface of the endothelium [57] (Fig. 2.2). This close anatomical apposition led to the suggestion that astrocyte is a major source of inductive influences on the development of specialized BBB phenotype of the brain endothelium [56]. Early evidence in support of this hypothesis came from grafting experiments in which brain vessels growing into grafts of peripheral tissue became less tight to intravascular tracers, while the relatively leaky vessels of peripheral tissues became tighter on growing into grafts of brain tissue [58].
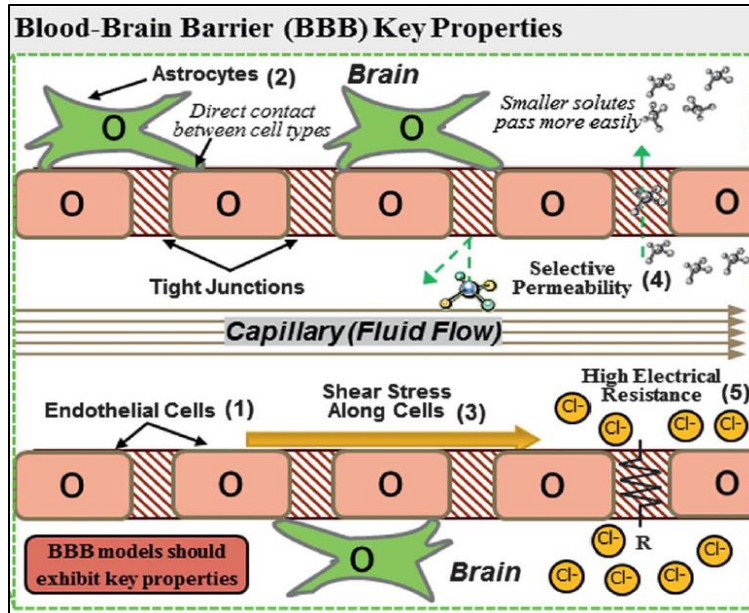
Figure 2. 1 - Schematics of an in vitro BBB models showing key properties likes endothelial cells with tight junction expression, co-culture with astrocytes, presence of shear stress, selective permeability to compounds, and high electrical resistance

Several sophisticated TBI models of the explosive blast or blunt force have been studied. However, the potential mechanisms connecting shock wave exposure to the head to TBI are still not well understood at all [59]. As stated in chapter 1, one of the mechanical trauma that has been investigated in our laboratory is the formation of micron-sized bubbles in response to a shock wave and subsequent collapse of such microbubbles, referred to as microcavitation [60]. The collapse of highly pressured microbubbles is thought to produce shear stress that can disrupt the brain endothelium [61, 62]. Our previously published work demonstrated that microcavitation detaches cultured cells and creates an area that is devoid of any cells. We coined the term "2D crater" to describe this microcavitation-induced effect. While we documented the effect of micro cavitation using astrocytes [60, 63], it is interesting to investigate whether the microcavitation mechanism is responsible for the disruption of the brain endothelium. Since a monolayer of mouse brain endothelial cells has been demonstrated to resemble the BBB phenotype found *in vivo*, express excellent characteristics of the BBB, and form the functional barriers [64], it offers a model system to elucidate the potential damage mechanisms that are associated with microcavitation. Three dimensional (3D) models are expected to provide a better understanding of brain diseases and pathologies. However, the formation of shock wave-induced microbubbles in 3D models is neither predictable nor controllable [187]. It will be a daunting task to predict the location of

microcavitation and then focus on determining the cellular responses. Attempt to monitor such responses in real time would be futile if one cannot reliably predict the microcavitation event. In contrast, the 2D culture system we developed allowed us to spatially control the microcavitation (see Methods below). Moreover, although confocal microscope should be able to generate reconstructed 3D images, the subcellular responses recorded by 2D images provide a glimpse of the dynamic (e.g., calcium spiking) involved in microcavitation.
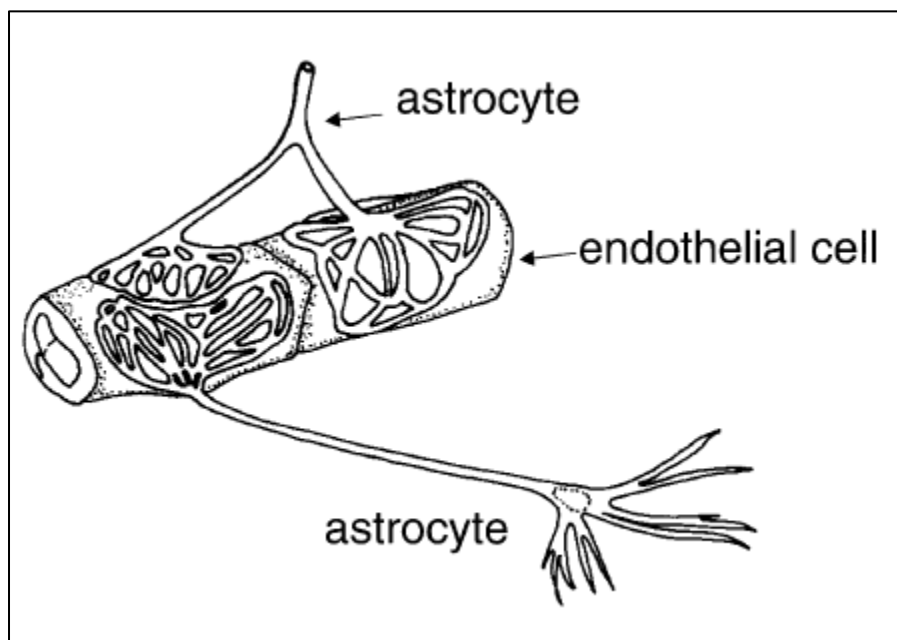
Figure 2. 2 - Schematic of astrocyte feet in contact with the brain capillary surface, allowing for two-way induction and communication between the astrocytes and endothelium, Abbott et al., [56].

Although there is an increasingly better understanding of brain trauma, it remains elusive to determine whether reparative treatments are plausible. A recent study suggests that approximately 320,000 soldiers may have experienced mild TBI in the Iraq and Afghanistan wars and that such injuries most often lead to cognitive degeneration and post-traumatic stress disorder (PTSD) [65]. There are only a limited number of treatments currently available, and in most cases, only the symptoms are identified and treated. For example, selective serotonin reuptake inhibitors have been approved by the FDA. Some non-pharmacological treatments, such as cognitive-behavioral therapy may also be effective [66]. Use of a family of copolymers referred to as poloxamers offer an intriguing potential to mitigate the blast-induced cell damage. Because many studies have shown that the poloxamers are capable of sealing the compromised cell membrane, the FDA-

approved poloxamers P188 was demonstrated to seal the membrane in BBB [67] and down-regulate the secretion of matrix metalloproteinases [68]. However, the role of P188 in the cytosol remains to be further studied. It is suspected to be involved in the TNF-α pathway [69]. In this study, we cultured a monolayer of brain endothelial cells on a well-characterized synthetic membrane and quantitatively determined changes in the permeability and disorganized tight junctions. Our results show that microcavitation functionally and mechanically disrupts the BECs and that treatment of brain endothelial cells with P188 mitigates the BECs disruption by alleviating the loss of tight junctions and suppressing the excess production of MMPs.

2.2 MATERIALS AND METHODS

2.2.1 Design, Fabrication, and Setups of the Culture Model.

Three laser-cut pieces of PMMA were utilized (base layer: 30mm x 30mm, middle layer: 30mm x 30mm, with a rhombus shape cut-out of the length of 14mm on each side. upper layer: 30 mm x 30mm, with a circular shape cut out of diameter 10mm). A PDMS polymer was laser cut in the same dimensions for both the middle and upper layers. The device was set up by sticking the base and middle chamber together to create a chamber, and PDMS was attached to the top of the middle. PDMS was also attached to the bottom of the upper layer to provide adhesion and allow for easy detachment. PDMS was fabricated as described by Abhyankar et al., [70]. Briefly, PDMS prepolymers (10:1 base to catalyst ratio,) was spin-coated to obtain a uniform thickness of 0.30mm (Fig. 2.3A). Holes for magnetic sealing were cut with a diameter of 1.59mm. An insert with a laser-cut PETE culture membrane (1.0 μm pore diameter, 2 X 10^7 pores / cm^2 Sterlitech) (Fig. 2.3A and C) was sandwiched and laminated between two laser cut sticky sheets containing an open central region(10mm diameter) and then, was sandwiched in between the middle layer of the chamber and the upper layer and sealed with magnets of different poles (kjmagnetics) to have airtight compartments. This sandwiching of the insert gives the chamber two compartments. After assembling, membranes and chambers were sterilized with 70% alcohol for 5 minutes and washed with PBS (10mM sodium phosphate, 150mM sodium chloride, pH 7.4).

2.2.2   In vitro Brain Endothelium Model

Mouse brain endothelial cells were cultured on a synthetic polyethylene terephthalate (PETE) membrane (Sterlitech, PET1047100) that contains 1 μm diameter pores at the density of 2×10^7 pores /cm^2. This well-defined membrane allowed us to establish a monolayer of endothelial cells and determine the endothelium permeability. Balb/c mouse primary brain microvascular endothelial cells (MPBMECs; Cell Biologics Inc., C576023) were grown in endothelial basal medium-2 (EBM-2) with EGM-2 kit (Lonza, CC3156, CC4176 respectively) in a flask coated with a gelatin-based coating solution. Cells were seeded at the density of 6.60×10^4 cells/ cm on the PETE membrane coated with fibronectin (l μl/mL). To confirm the viability of MPBMECs, an in vitro angiogenesis was performed. Briefly, reduced growth factor Matrigel (200 ul; Corning, 356230) was pipetted onto a 22x22 mm coverslip in a petri dish and incubated at 37 °C and 5% CO_2 for 30 min to solidify Matrigel. Once Matrigel was set, approximately 5×10^4 cells MPBMECs were seeded on the gel, and tube formation was observed after 6 hrs. To visualize cells, green cell tracker (FITC) was added to the cells before seeding. Images were recorded using a 20x microscope objective.

2.2.3   Microbubble Exposure Chamber

A detailed description of the microbubble chamber used in this experiment has been provided elsewhere [60, 63]. This chamber is designed to fit the microscope stage for real-time imaging. Briefly, two platinum electrodes were symmetrically embedded in the middle of the chamber (~ 10 mm high; Fig. 2.3D). Shock waves were generated by applying an electrical pulse across the electrodes that were separated by 700 um. Electrical breakdown of water creates shock waves, followed by the generation of microbubbles. Potential artifacts such as temperature rise, excessive-high electric field, and the impact of shock waves were all carefully addressed in the previously published papers. For example, the temperature rise of < 0.5 $^{\circ}$C was measured [63], and the principle of symmetry was applied to study the effect of the shock wave by plating cells at the bottom of the chamber (Fig. 2.3D). Should the shock waves (0.3 us travel time across the depth of the chamber) cause any measurable impact, these effects should be observed both at the top and bottom of the chamber. The cells plated at the bottom of the chamber were observed viable and functional [63] and expressed the baseline fluorescent markers, for example, of apoptosis [63]. In

contrast, the microbubbles rose only to the top of the chamber and collapsed onto the plated cells. The density of microbubbles, their speed and size distribution following the propagation of shock waves were recorded, analyzed, and reported in our previous study [63]. Determination of the cellular and molecular signatures that are associated with cell damage is the aim of the current study and described below in the Results section.

2.2.4   Immunostaining for ZO-1, Actin, and MMP-2 & 9

Tight junctions in the brain endothelial cells were visualized using zonula occludens 1 (ZO-1) monoclonal antibody conjugated with Alexa Fluor 488 (Thermofisher Scientific, MA339100A488). Briefly, the BECs were fixed with 4% paraformaldehyde in PBS for 10 minutes at room temperature and blocked with 3% of BSA for 1 hour. Cells were incubated with fluorescently conjugated ZO-1 monoclonal antibody for 1 hour and kept in the dark. Nuclei were stained with DAPI at a dilution of (1:1000). For MMP-2 & 9 analyses, cells were fixed with 4% paraformaldehyde in PBS, permeabilized with 0.1% Triton X-100 for 3 minutes and blocked with 3% of BSA for 1 hour. Cells were incubated with the MMP-2 & 9 primary antibodies (1:500, 4.3 µg/ml, Santa Cruz., SC13595, and SC393859 respectively), and subsequently incubated with Alexa Fluor 488-conjugated goat anti-rabbit IgG (1:1000, 2 µg/ml, Santa Cruz., SC516167).

2.2.5   RNA Isolation and Gene Expression Measurements

Total RNA was isolated according to protocols supplied by the manufacturer (Quick-RNA Microprep Kit, Zymogen Research Corp, R1050). Briefly, cells were lysed in an RNA lysis buffer washed with 95% ethanol and RNA prep buffer, and then sequentially washed with RNA wash buffer, and RNA was eluted with 15 ul of DNase/RNase-Free water. The sample was treated with RQ1 RNase-Free DNase from (PROMEGA Corp, M6101) to remove any remaining DNA. RNA yield was quantified using nanodrop by measuring the optical density of the sample at 260–280 nm. RT-PCR was carried out using the manufacturer's protocols. cDNA was synthesized using AzuraQuant cDNA Synthesis kit (Azura Genomics, AZ1996). The mastermix was prepared using AzuraQuant Green Fast qPCR Mix Hirox Kit (Azura Genomics, AZ2001). Two microliters of cDNA were used in each subsequent PCR reaction. Specific primers for BBB tight junction protein; zonula occludens 1 (ZO-1), and a housekeeping gene, GAPDH (RealTimPprimers.com),

were designed and synthesized according to published sequences (RealTimePrimers.com). PCR amplifications were performed in a final volume of 20 mL of the mastermix using AzuraQuant Green Fast qPCR Mix Hirox as instructed by the manufacturer. Using applied biosystems 7300 Fast Real-Time PCR system (Thermo Fisher), amplifications were done for 45 cycles using a denaturation step at $95^{\circ}C$ for 5 s, an annealing step at $60\ ^{\circ}C$ for 25 s, and polymerization step at $72\ ^{\circ}C$ for 45 s.

2.2.6   In Vitro Diffusion Model and Permeability Experiment

A custom-designed diffusion chamber was constructed (Fig.2.3E). Adhesive glue was applied to the entire boundary of the chamber to prevent leakage. And a PDMS with 10 mm aperture was aligned with the insert and glued in place over the insert. After sealing the chamber properly, the upper chamber was filled with PBS containing FITC dextran molecules. The apparatus was discarded if leakage into the lower chamber was detected. The lower chamber of a 5 ml volume was filled with PBS without phenol red. The experiment was conducted in the dark and at room temperature. FITC dextran of molecular weight 3 and 10 kDa were used for the experiment. 25 µl were collected from the lower chamber at one-hour intervals for 6 hours and stored at -80 °C. Fluorescence intensities were measured using a fluorescence plate reader (Synergy HT). Fluorescent intensity calibration standard was obtained by serial dilution of fluorescent dextrans. Concentrations in the collected samples were determined from the calibration curve. The Permeability coefficient was then calculated by modifying the equation from Li et al., [71]; $P = \frac{[(C2a - C1a) *Va)]}{[A*\Delta t* Co]}$, where P is the permeability coefficient, C_{2a} & C_{1a} are the concentration in the abluminal chamber at different time intervals, V_a is the volume of the abluminal chamber, A is the surface area of the membrane, Δt is the duration of steady-state flux, C_o is the concentration in the luminal chamber. The expression $(C_{2a} - C_{1a})/ \Delta t$ is considered as the slope of the diffusion curve over time.

2.2.7   Conjugation of P188 with TAMRA

The procedure to fluorescently conjugate P188 was carried out as described elsewhere with slight modification [72]. Briefly, the hydroxyl terminal groups of P188 were converted to amino groups by activating dry P188 (5 g, 50 mM) with carbonyl diimidazole (CDI) (257 mg, 1.6 mM) in

anhydrous dichloromethane (DCM) (50 ml) at 37 ºC for 4 h. After cooling to room temperature, a mixture of ethylenediamine (398 µl, 6 mM) and N, N-diisopropylethylamine (DIPEA) (277 µl, 1.6 mM) was added to the solution and stirred for 48 h which resulted in 1-amino-2- 10 Ethan carbamate functionalized P188 (P188-NH2). The resulting mixture was then dialyzed using a 2 kDa-cutoff membrane against 15% ethanol for 4 days changing the buffer 8 times and freeze-dried to yield P188-NH$_2$.

Synthesized P188-NH2 (200 mg) was dissolved in acetonitrile (2 mL) and then 2 mL of 0.1 M sodium tetraborate buffer (pH 8.5) was added to the solution and stirred for 1h. A solution of TAMRA-SE (19 mg, 31.8 µmol) in DMSO (1 ml) was added to the above mixture and stirred at for 18 h at room temperature. The resulting mixture (TAMRA – P188) was diluted with 20% ethanol and dialyzed with 2 kDa-cutoff membrane against 20% ethanol for 5 days at room temperature, changing the buffer 15 times and then ultracentrifuged before freeze-drying.

2.2.8   Statistical analysis

All data analysis was executed using one-way and two-way ANOVA (R-Studio Software) to analyze differences between group(s) with one or more independent variables. $p < 0.05$ was considered as significant difference. *Post hoc* analysis was done using Tukey's honest significant difference (HSD). All data were reported as mean ± standard deviation.

2.3   RESULTS

2.3.1   Cell Culture Chamber Design, and Non-transformed phenotype of mouse primary brain microvascular endothelial cells (MPBMECs).

The culture-insert enabled direct cell seeding from the top (Fig. 2.3A). Before culture, the membrane in the insert was properly coated with fibronectin. To establish that our model and PETE supports cell culture, EC was preincubated with cell tracker (green) for 30 minutes before seeding on the membrane (Fig. 2.3C). Following cell culture, culture insert (Fig. 2.3C) was transferred to an induce blast exposure chamber (fig. 2.3D) to carry out microcavitation, followed

by permeability experiments (Fig. 2.3E) which will be explained in detail later. The portability of the inserts and devices allows for easy maneuvering.
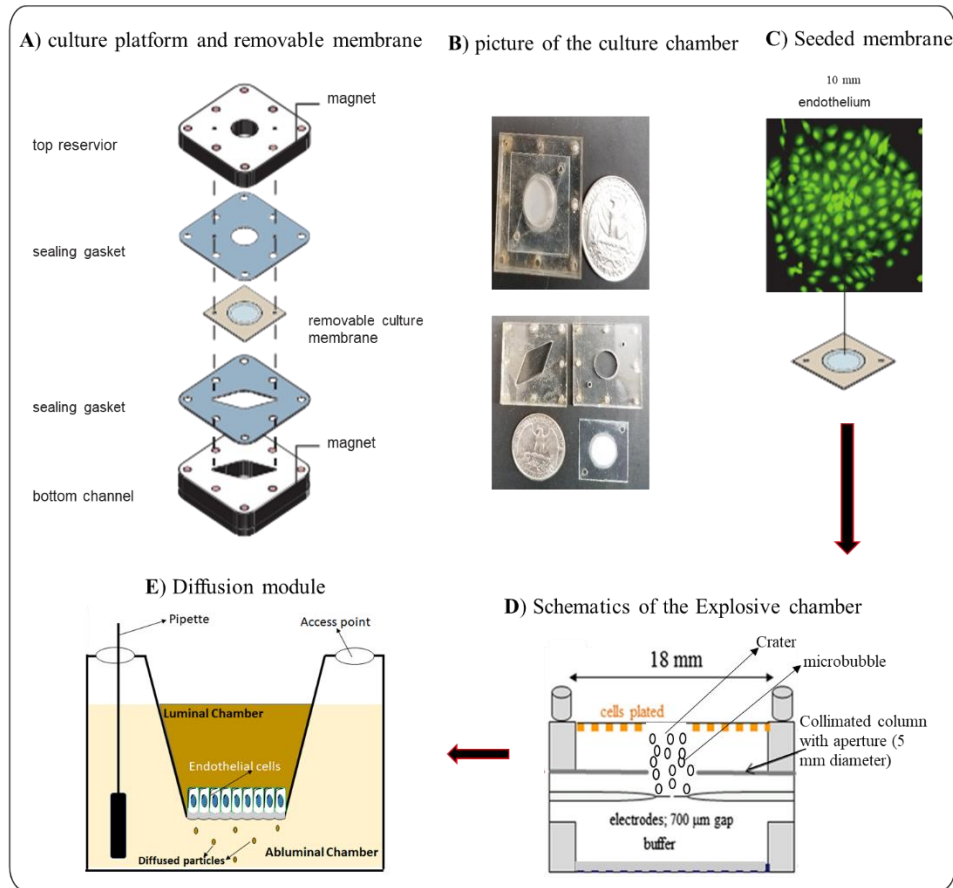
Figure 2. 3 - Schematics of the culture chamber, culture insert, proof of cell adhesion to PETE membrane, blast exposure chamber, and diffusion chamber. (A) Culture chamber composed of PMMA housing with magnet holes, PDMS sheets, and a removable cell culture insert. (B) picture of the uncoupled two-chamber system. The chamber can also support two cell cultures. (C) Culture insert showing cell culture. Green FITC cell tracker is showing that PETE membrane supports endothelial cell culture with strong adhesion. Endothelial cells were seeded on a fibronectin-coated membrane. (D) Diagrammatic representation of the design and structure of the blast chamber, depicting the events that take place after transferring the cell culture insert to the blast chamber. Bubbles are formed, and the collapse of the bubbles causes cells and BECs destruction, and the formation of "crater". (E) Schematic description of our diffusion model, with BECs monolayer on the luminal side of the membrane. Permeability was measured by introducing FITC dextran dye of different molecular weights into the luminal chamber and measuring the time-dependent concentration in the abluminal chamber.

Endothelial cell-seeded reached confluence at day 4. The MPBMECs used in this study showed a morphology like primary cultures of brain endothelial cells, with monolayers of tightly packed elongated cells that exhibited cell-cell contact at the confluence (Fig. 2.4A). At confluence,

MPBMECs exhibited spindle-shaped morphology previously documented in brain endothelial cells derived from human [73] (Fig. 2.4B). The MPBMECs cell population displays the presence of tight junction protein ZO-1at day 4 of culture (Fig. 2.4C). The MPBMECs maintained a non-transformed phenotype over more than 6 population passages, without any sign of senescence, as supported by the following observations: 1) immunofluorescence images from passages 5 and 6 (Appendix 1. A and B); and 2) when MPBMECs were seeded on reconstituted extracellular matrix (Matrigel), they rapidly formed a branched capillary-like cords network, a characteristic which is typical of primary endothelial cells, suggesting a normal capacity for angiogenesis (Fig. 2.4D). This was also observed at different passages (Appendix 1. C and D). Endothelial cells also displayed well-aligned skeletal F-actin fibers at day 4 of culture (Fig. 2.4E). For all experiments, endothelial cells cultured to day 4 were used.
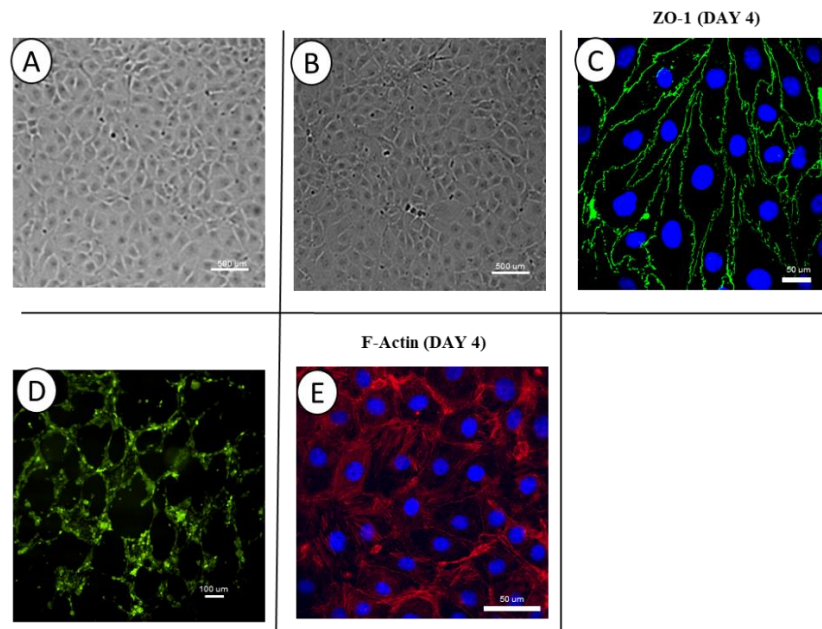
Figure 2. 4 - Morphological Characterization of mouse primary brain microvascular endothelial cells (MPBMECs). (A) Phase-contrast microscopic view of the MPBMECs showing tightly packed contact morphology (B) Human umbilical vascular endothelial cells (HUVECs) with similar morphology. (C) Immunofluorescence staining is demonstrating the expression of the endothelial cell tight junction-associated marker, ZO-1 (green) after 4 days of culture. (D) A branched network of capillary-like cords formed by MPBMECs in Matrigel extracellular matrix after 6 hours in EGM-2 medium (20X). (E) Immunofluorescent staining of mouse endothelial cell skeletal fibers, F-actin (red). Nuclei counterstained with DAPI.

2.3.2 Microcavitation, FITC molecule permeability, and TAMRA – P188 conjugation.

The experimental model employed in understanding the effects of microbubbles and for better interpretation of our results is shown in Figure 2.5A. It shows our area of interest; the "crater" and the periphery (blast radius- R_B) of the crater. We measured the average area of the crater created from the blast and estimate the area over which the bubbles act. From our model, cells within the crater are rendered destroyed. Cells within the R_B of the bubbles are affected by bubbles (e.g., either permeabilized, destroyed, or their tight junctions are disrupted), and those cells that are outside the blast radius are not affected. The level of bioeffects caused by microcavitation on MPBMECs was observed by fluorescence images (Fig. 2.5B - E).
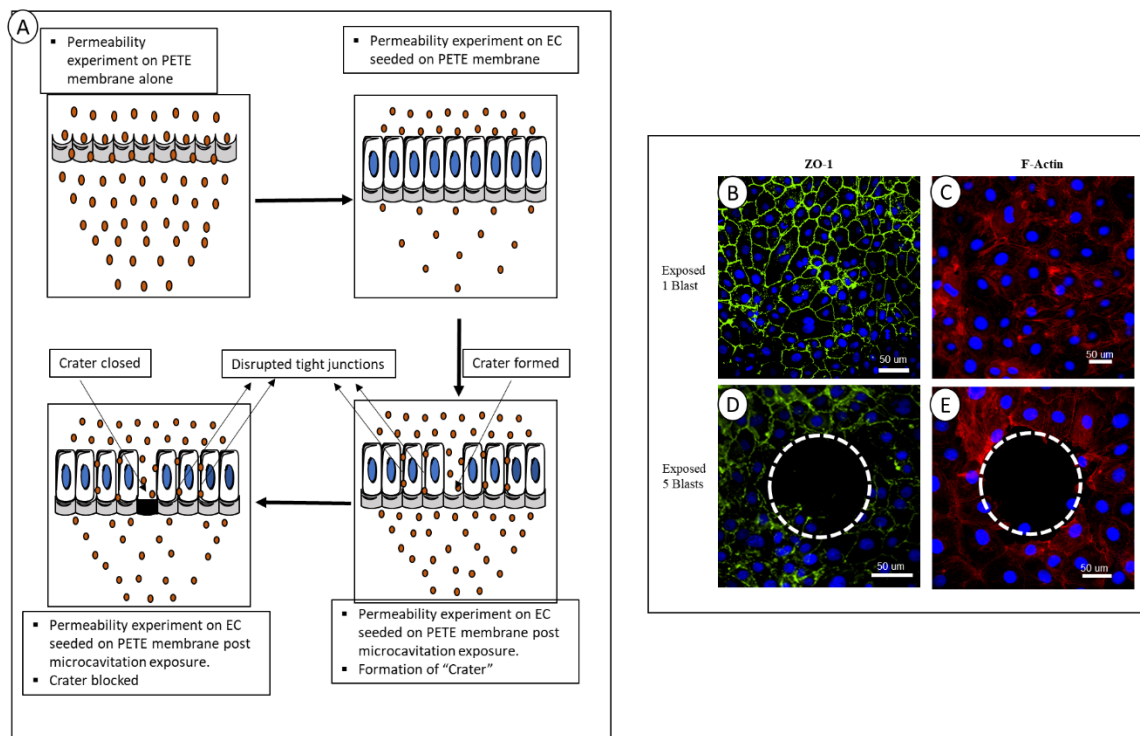
Figure 2. 5 - Schematics of permeability experiment and confirmation of microcavitation(MC) disruption of Blood-brain endothelium. (A) Summarized procedures for the evaluation of dextran molecule permeability across our in vitro BBB model. (B & C) Immunofluorescence Staining of EC for ZO-1 (green), Actin (red) post MC exposure to 1 blast. (D & E) exposure to 5 blasts. *There is no obvious destruction of tight junctions nor cells after 1 blast exposure. However, there is TJs/cell destruction and formation of the crater after 5 blasts exposure. The nuclei (blue) stained with DAPI.

Monolayers of MPBMECs, grown to confluence on porous membranes, were tested for their permeability to hydrophilic molecules (control group). The experimental groups were subjected to microcavitation. Exposure to one blast alone did not have any major impact on endothelial cell monolayers (Fig. 2.5B and C). However, exposure to 5 repetitive blasts caused major damage. It should be noted that the repetitive blast-induced TBI is presumed to be responsible for clinical manifestations [63]. The damage from 5 blasts (Fig. 2.5D and E) was far greater than the damage from 1 blast. To calculate the permeability of R_B, concerning 5 repetitive blasts exposure, the following steps were followed (Fig. 2.5A) STEP-1; diffusion was carried out on the membrane without cells. STEP-2; on the membrane with EC monolayer. STEP-3; on EC monolayer post-microcavitation exposure. STEP-4; finally, to calculate the permeability of R_B the crater was blocked before carrying out the permeability experiment.

Figure 2.6 shows the measured permeability coefficient (P) of our *in vitro* brain endothelial model of two different molecular weight fluorescent solutes: 3 and 10 kDa. The values of P^{3K} and P^{10K} for various experimental groups are recorded in Table 1 below. P^{3K} and P^{10K} for EC monolayer were significantly decreased by 85% and 84% respectively from that of the PETE membrane alone, as expected. On the other hand, microcavitation by 1 blast exposure did not cause any significant increase the permeability coefficients. However, 5 blasts exposure drastically increased the P^{3K} and P^{10K} compared to using monolayer alone (for all experimental groups, n = 6, P < 0.05). To validate that disruption occurred around the crater, the crater was blocked, allowing permeability to be observed only around the crater (results presented in Table 2). Permeability coefficients were also measured in cells treated with P188 and with the crater blocked (Table 2).
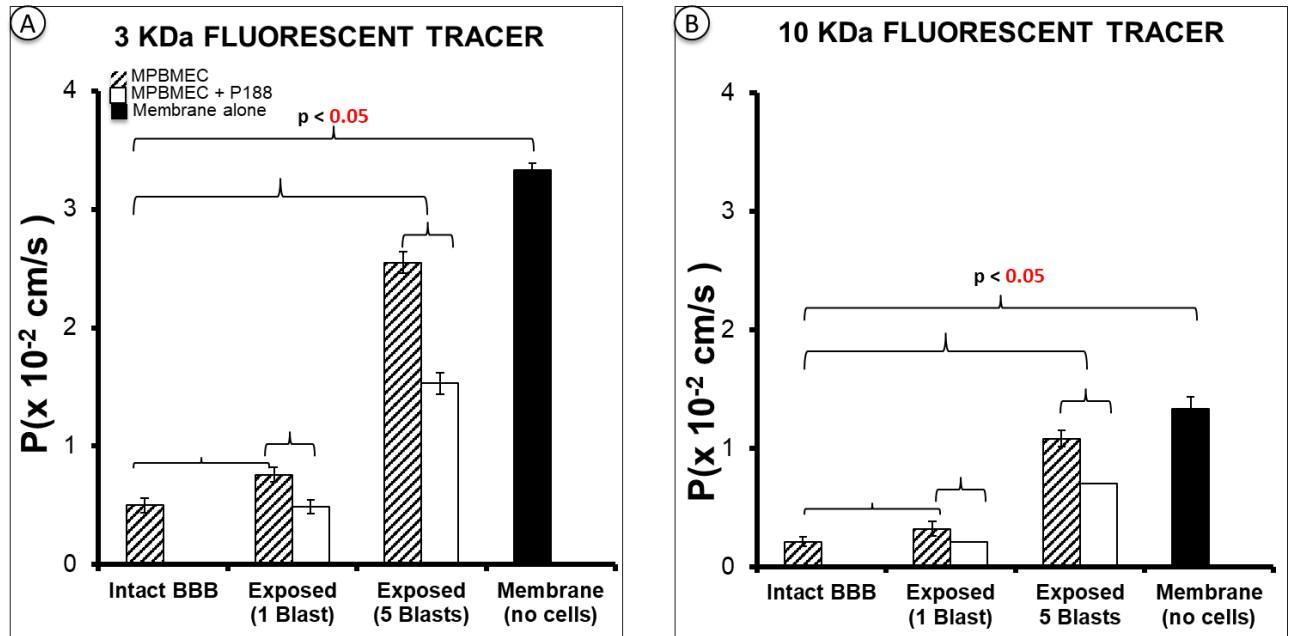
Figure 2. 6 - Graphs showing the permeability coefficient (P). (A) The permeability coefficient of MPBMECs monolayer to 3 kDa after exposure to blasts and after treatment with P188. (B) Permeability coefficient to 10 kDa. * Increase in permeability is correlated to the repetition of exposure to blasts. Also, 3 kDa molecules have a higher permeability as expected, n = 6

Table 2 - Permeability coefficient (P) post MC and after P188 treatment

	P^{3K} (cm/s)	P^{10K} (cm/s)
Membrane alone	$3.33 \pm 0.02 \times 10^{-2}$	$1.33 \pm 0.02 \times 10^{-2}$
MPBMECs monolayer	$0.50 \pm 0.06 \times 10^{-2}$	$0.21 \pm 0.04 \times 10^{-2}$
MPBMECs + MC (1 Blast)	$0.76 \pm 0.09 \times 10^{-2}$	$0.32 \pm 0.04 \times 10^{-2}$
MPBMECs + MC (5 Blasts)	$2.55 \pm 0.09 \times 10^{-2}$	$1.08 \pm 0.07 \times 10^{-2}$
CRATER BLOCKED		
	P^{3K} (cm/s)	P^{10K} (cm/s)
MPBMECs + MC (5 Blasts)	$1.02 \pm 0.12 \times 10^{-2}$	$0.23 \pm 0.06 \times 10^{-2}$
MPBMECs + MC (5 Blasts) + P188	$0.57 \pm 0.10 \times 10^{-2}$	$0.15 \pm 0.07 \times 10^{-2}$

We suspected that P188 not only sealed the compromised membrane but also entered the cytosol to interact with the molecular mechanisms that might further exasperate the function of tight junction. In order to investigate potential interactions, we conjugated P188 fluorescently using the TAMRA dye (see above) and incubate with cells exposed to different experimental conditions. Fluorescence images revealed the successful conjugation of TAMRA to P188 and the internalization of TAMRA-P188 by both control BECs and those exposed to microcavitation (Fig. 2.7A and B). The TAMRA dye alone also demonstrated its capability of diffusing through the cell membranes in control cells and even into the nucleus (Fig. 2.7C and D). It is not too surprising that the dye should diffuse across the membrane into the cytosol as well as into the nucleus since its molecular weight is only 527.53 Da. The TAMRA-P188 complex was also found to diffuse into the cytosol. However, in control cells, the complex was excluded from entering the nucleus. Surprising, some cells when exposed to microcavitation showed the complex penetrated into the nucleus, suggesting the mechanical trauma from microcavitation may have reorganized and changed the nuclear structure. This shows that TAMRA is not subjected to the problems associated with immunoconjugates such as decreased immunoreactivity and poor solubility. The in vitro studies of these TAMRA-P188 conjugates show that they specifically bind to organelles inside the cytosol and the internalization is documented by the fluorescent microscopy experiments. Our results suggest additional studies of the TAMRA-P188 complex that might play a role in the targeted therapeutics.
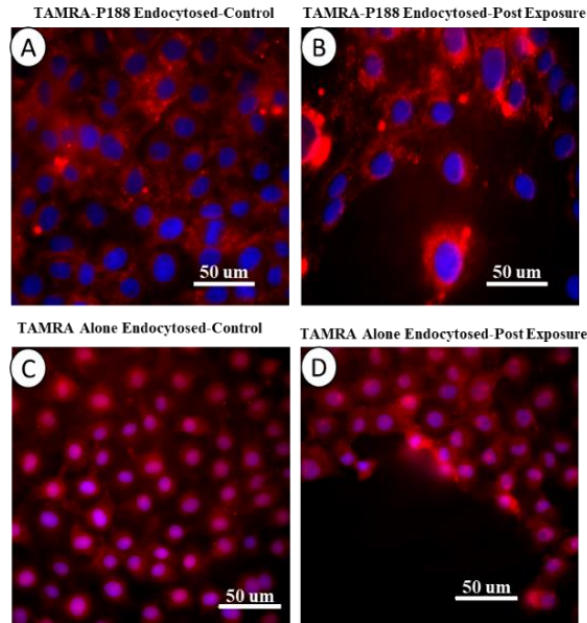
Figure 2. 7 - Validation of internalization of P188 by Primary brain endothelial cells and MMP-2&9 Gene expression. (A) Immunofluorescence images are showing endocytosis of conjugated TAMRA-P188 in control cells. (B) After Microcavitation. (C) Image of internalized TAMRA in control cells exposed to microcavitation (D). Nuclei counterstained with DAPI. 60X. Notice the colocalization in the groups treated with TAMRA alone (color change to purple in the nucleus depicts that the dye diffused all through the cells).

2.3.3 P188 Down-Regulates the Expression of MMP-2 & 9, Alleviate ZO-1 Loss and attenuates BBB Permeability.

In order to probe the potential interaction between P188 and MMP-2 & 9, we first pretreated the cells with P188 before activating them with TNF-α and measured the expressions of MMP-2 & 9 (Fig. 2.8A and E). The MMP expressions were found to be suppressed by such treatment. In contrast, in the cells activated by TNF-α without P188 treatment, we observed high expressions of MMP-2 & 9 (Fig. 2.8 B and F) respectively. Additionally, post-treatment with P188 after activating the cells with TNF-α also significantly suppressed the MMP-2 & 9 expressions (Fig. 2.8 C and G), respectively. The inactivated control cells (i.e., no TNF-α treatment) showed essentially no MMP expressions (Fig. 2.8 D and H). Pretreatment of cells with P188 before microcavitation showed a noticeable suppression of the MMP-2 & 9 (Fig. 2.9A and E), respectively. On the other hand, microcavitation alone caused a high expression of MMP-2 & 9 (Fig. 2.9B and F),

respectively. Post-treatment with P188 also suppressed the expression of MMP-2 & 9 (Fig. 2.9C and G), respectively. Experimental groups were compared to the control group (Fig. 2.9D and H).
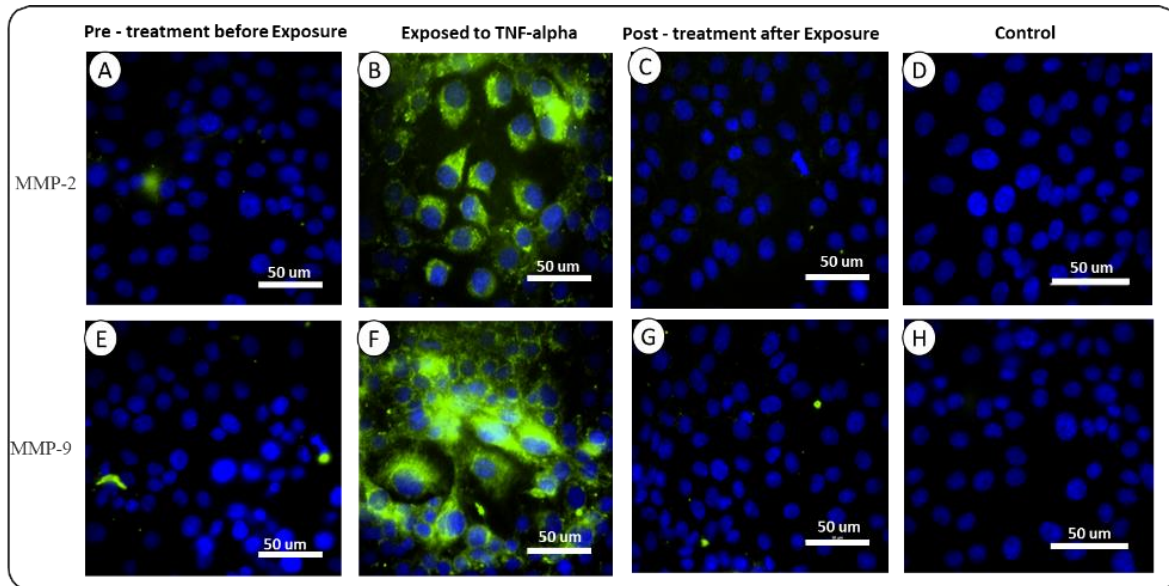
Figure 2. 8 - Activation of MMP-2 & 9 by biochemical disruption of TJs: Immunofluorescent staining of MMP-2 & 9 in TNF-alpha activated MPBMECs. ECs pretreated with P188 for 3 hours before incubating with TNF-alpha for 1 hour and then stained for MMP-2 & 9 (A & E) r espectively. ECs incubated with TNF-alpha for 1 hour and then stained for MMP-2 & 9 (B & F) respectively. EC incubated with TNF-alpha for 1 hour, treated with P188 for three hours, and then stained for MMP-2 & 9 (C & G) respectively. Results from all groups were compared with control (D & H) respectively.
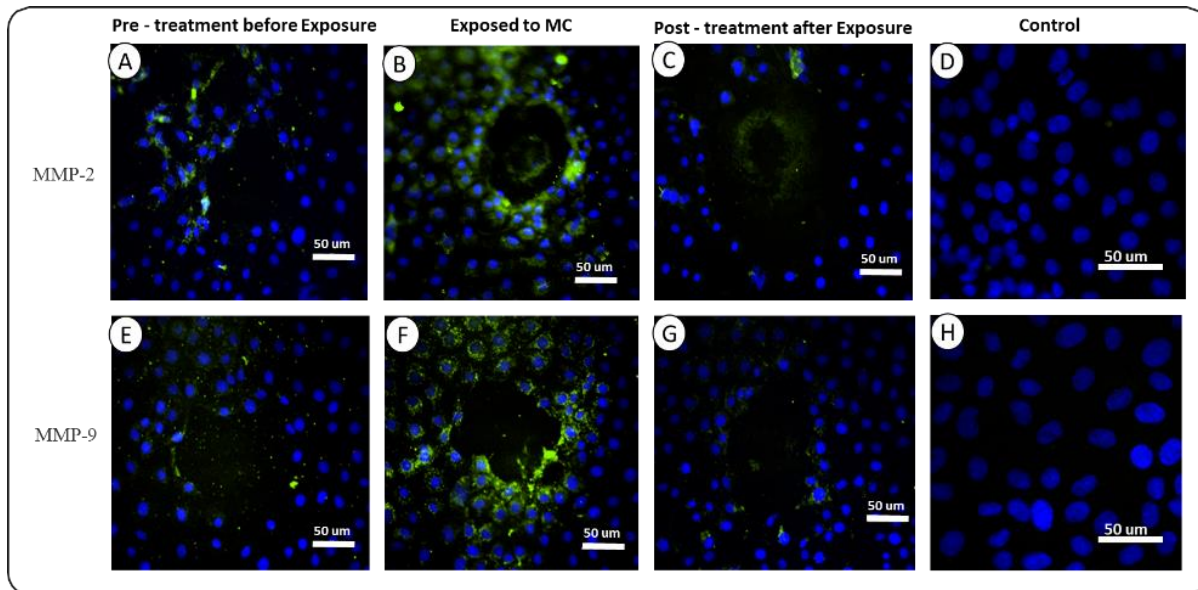
Figure 2. 9 - Activation of MMP-2 & 9 in traumatic brain injury: Immunofluorescent staining of MMP-2 & 9 in mechanical disruption of MPBMECs TJs. ECs pretreated with P188 for 3 hours before subjecting to induced blast and then stained for MMP-2 & 9 (A & E) respectively. ECs exposed to last and then stained for MMP-2 & 9 (B & F) respectively. ECs exposed to the blast, treated with P188 for three hours, and then stained for MMP-2 & 9 (C & G) respectively. Results from all groups were compared with control (D & H), respectively.

The expression of ZO-1 network in the microcavitation-exposed group was shown disorganized (see Fig. 2.5B and D). To correlate the protein expression with activation of genes, PCR experiments were carried out to quantify the gene expression. About a 6-fold decrease in the ZO-1 gene expression was measured (Fig. 2.10A) in response to exposure to microcavitation ($P < 0.05$). PCR measurements showed significant increases in the MMP-2 and 9 gene expressions induced by microcavitation. Either before or after treatment of cells with P188 was effective in restoring the MMP gene expressions to the control level (Fig. 2.10B and C). Consequently, upregulating ZO-1 protein expression which led to tight junction restoration. Excess production of MMP-2 and 9 is none to degrade tight junction proteins (ZO-1) and increase Brain endothelial cell permeability [46, 76]. Table 3 shows forward and reverse primers used in this study. This finding agrees with a recent report on primary cultures of human brain endothelial cells [75], where ZO-1 gene expression significantly decreased due to tight junction disruption.

Table 3 - Primers used for RT - PCR

GENE	FORWARD PRIMER (5'-3')	REVERSE PRIMER (5'-3')
ZO - 1	CCACCTCTGTCCAGCTCTTC	CACCGGAGTGATGGTTTTCT
GAPGH	CTGGAGAAACCTGCCAAGTA	TGTTGCTGTAGCCGTATTCA
MMP-2	CACCTGGTTTCACCCTTTCT	GAGGAGGGGAACCATCACTA
MMP-9	CTCACTCACTGTGGTTGCTG	TGGTTATCCTTCCTGGATCA
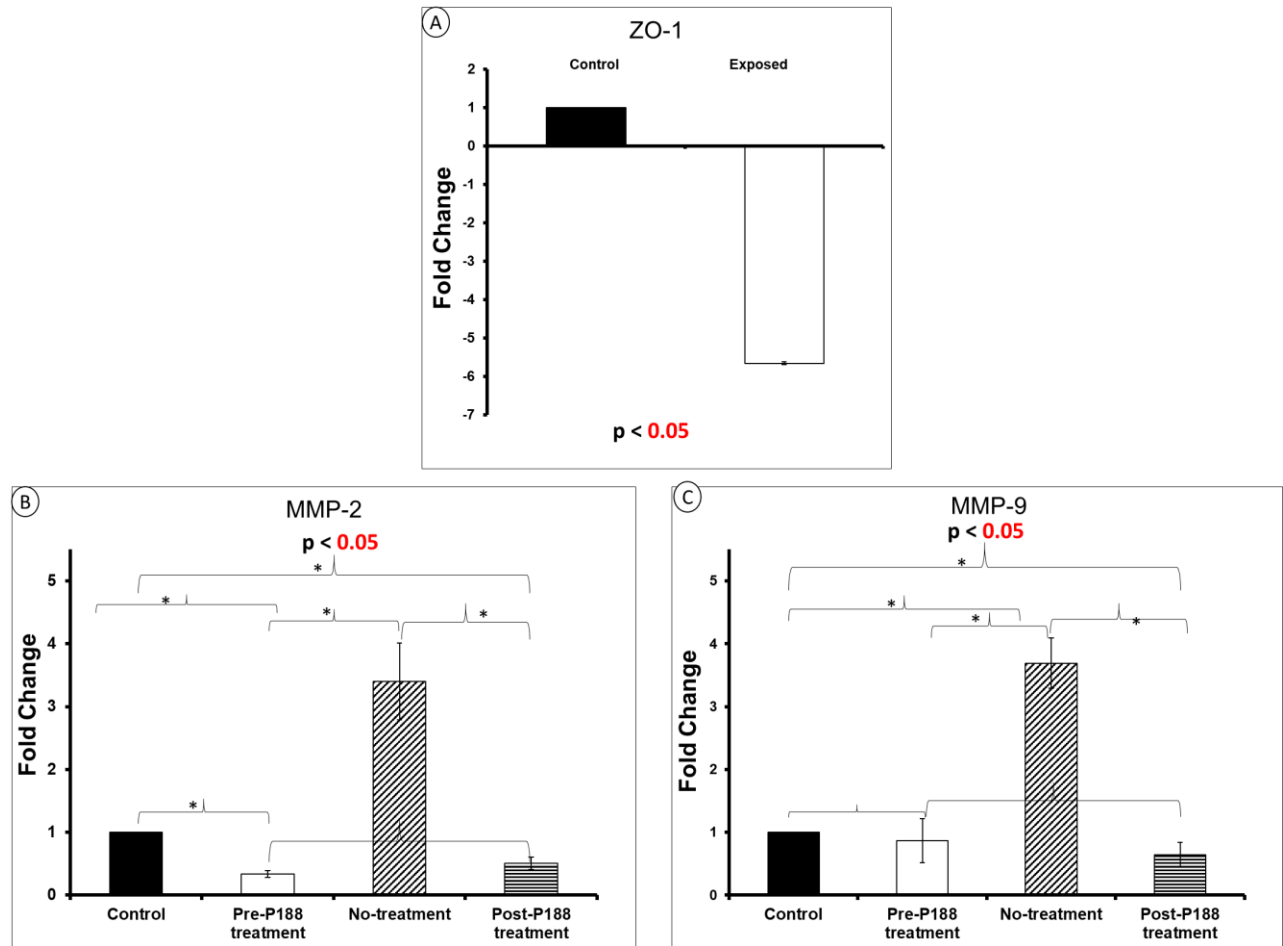
Figure 2. 10 - Fold change after exposure to microcavitation. (A) The decrease in expression levels of ZO-1 was calculated from triplicate reactions. (B & C) Signifies the efficacy of P188 in suppressing the expression of MMP-2 & 9 in both pre-treated and post-treated groups. Fold change were calculated from triplicate reactions as well, n = 6.

To test if there is a therapeutic window that P188 should be administered in order to render successful repair of the disrupted brain endothelium, cells were treated at different time points after blast exposure. Treatment to cells exposed to microcavitation was delayed for about 10 to 60 minutes (Fig. 2.11A and B) before treating with P188. Interestingly, the treatment with P188 significantly alleviated ZO-1 protein loss between 1 to 3 h after treatment (Fig. 2.11C-F). We also waited for about 3 to 6 hours before administering P188 to the exposed cells, and we observed a higher rate of tight junction degradation (Fig. 2.12A and B). Consequently, when we treated the cells with P188, we did not observe total tight junction restoration (Fig. 2.12C - F). What these indicate is that there is a therapeutic window that P188 should be administered to obtain total or complete tight junction restoration. Additionally, the longer the treatment, the higher the expression of a well-arranged network of tight junction [68]. It is interesting to observe that, without treatment of P188, the 2D crater that was created by microcavitation seemed to expand (Fig, 2.12B) in comparison to when the sample was treated with P188 (0.5 mM) for 3 hrs (Fig. 2.12F). Taken collectively, the P188 treatment appears to restore the biotransport properties and tight junction expression.
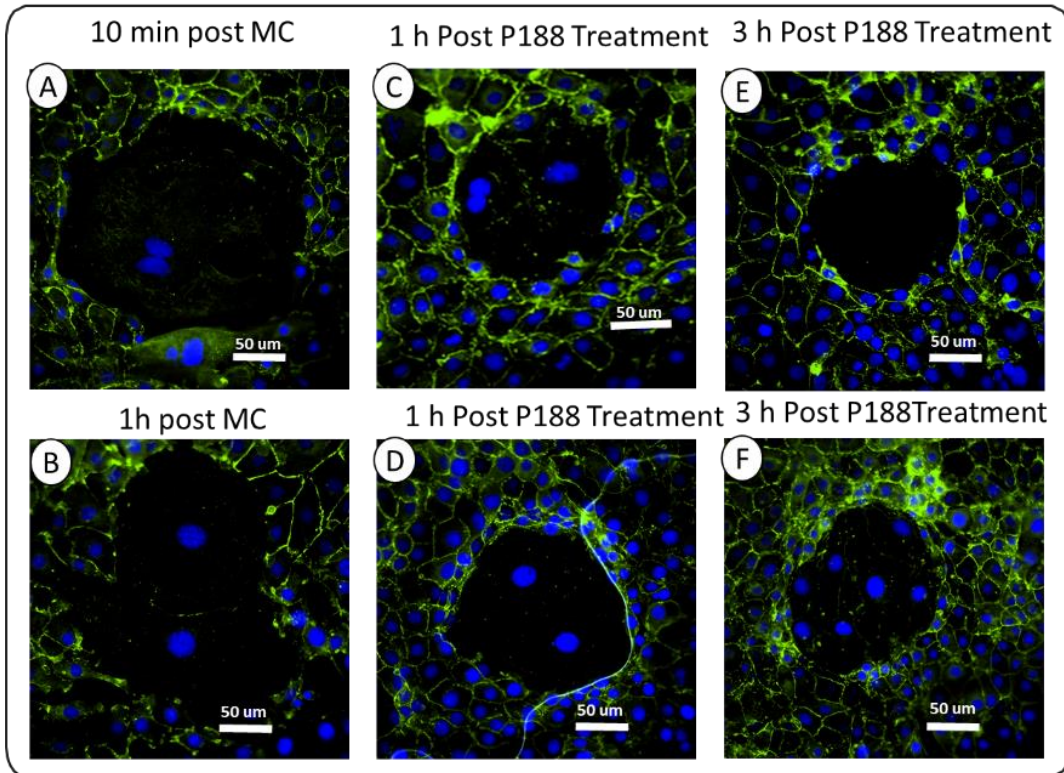
Figure 2. 11 - Effects of P188 on TJ localization in MPBMECs post-exposure to microcavitation. Confluent MPBMECs monolayers were exposed to microcavitation(MC) and then incubated with normal media for 10 min and 1 h, before treating with P188 for 1h and 3 h. Distribution/expression of TJ proteins was examined by immunofluorescence staining. Panels (A & B) represent the control, (C & D) represent the 1 h treatment group, and (E & F) represent the 3h treatment group. Immunofluorescent images showed reconstitution of tight junctions after treatment with P188.
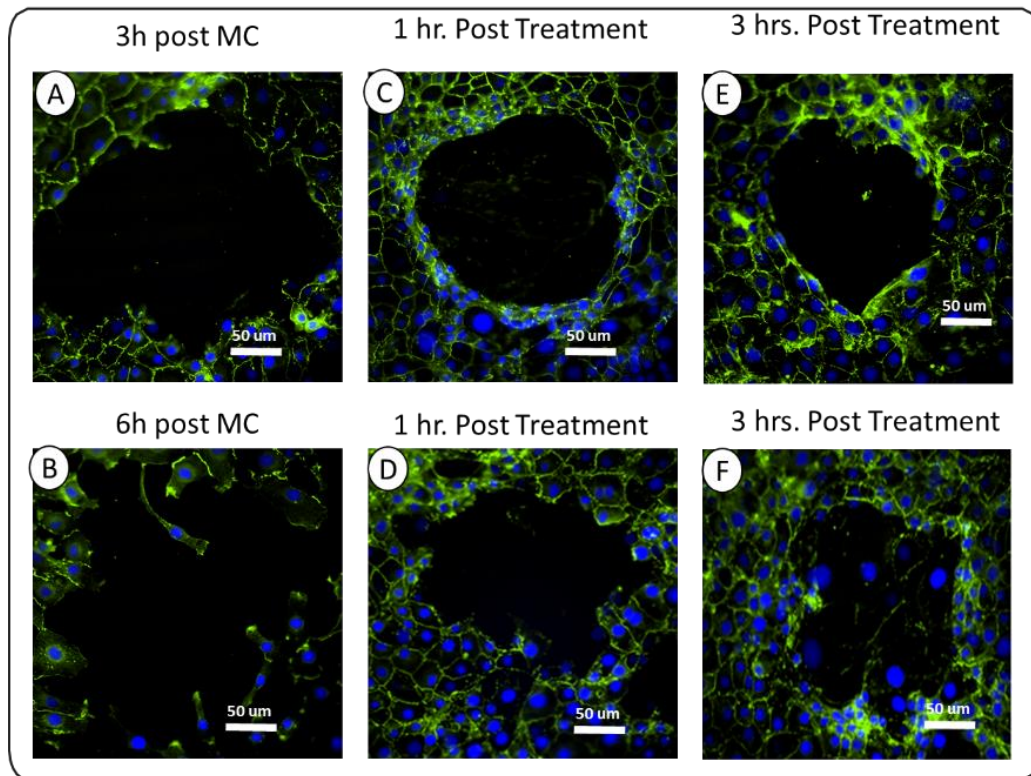
Figure 2. 12 - Based on the results for 10 min and 1h, we proceeded to examine the TJ localization for 3 and 6 h, before subsequent treating with P188 for 1 and 3 h. Panels (A & B) represent the control (3 and 6 h respectively), (C & D) represent the 1h treatment group, and (E & F) represent the 3h treatment group. Longer waiting period lead to a higher rate of tight junction degradation. Total restoration of tight junctions was not observed in groups delayed for over three hours.

2.4   DISCUSSION

Traumatic brain injury causes activation of inflammatory responses and release of free radicals, which leads to necrosis and eventual apoptosis [63]. There are several models of BBB disruption, but none focuses on the mechanism of the brain endothelium disruption and identification of enzymes that are involved in the disorganization of tight junction. In response to microcavitation our model allowed us to explore the mechanism responsible for blood-brain endothelium disruption and the key enzymes involved as well as the efficacy of P188 in attenuating traumatic brain injury. P188, which is a triblock copolymer approved by FDA to be used as a free drug for blood thinning, has been reported seal the compromised cell membrane. In recent years, it has been shown that P188 can be internalized by the cells and thus affect intracellular activities, such as blocking the cascade reaction due to inflammatory factors, excess activation of cytokines, and

33

as well as the release of free radicals. In this study, we found that treatment with P188 to disrupted endothelial cells for 1 – 3 hr promoted the functional recovery of tight junction by down-regulating MMP-2 & 9 and up-regulating ZO-1. The future experiments may be designed to investigate the correlation between the MMP-2 & 9 and adhesion molecule, specifically CD49d post microcavitation to determine the cell-substrate adhesion.

Maintenance of the BECs relies on the interaction of endothelial cells and basement membrane. Together, they play an important role in the bio-transport of molecules from the blood to the brain and vice versa. TBI is typically accompanied by an increased permeability through the BBB that causes extravasation and intravasation of molecules larger than 500 Dalton. Studies have shown that an increased level of MMP-2 & 9 plays a key role in BBB destruction by induction of inflammatory cascade reaction [76]. These two are the two most studied proteolytic enzymes, and their increased activity is associated with the BBB permeability [46] facilitating degradation of tight junction proteins. The inhibition of MMP-2 & 9 promotes recovery of the BBB [77]. Therefore, targeting MMP-2 & 9 may be one of the strategies for the treatment of TBI. Our results show that an excessive expression of MMP-2 & 9 induced by TNF-α (chemical) and microcavitation (mechanical) can be reversed by P188 treatment.

The blood-brain endothelium and tight junctions are very important components of the BBB. The permeability of the BBB, for example, is associated with the tight junction's integrity [78]. ZO-1 plays a fundamental role in maintaining the BBB integrity by forming a selectively permeable barrier. The BBB can be compromised by either biochemically or mechanically, which increases permeability. First, we tested the theory that P188 and the TAMRA-P188 complex can be internalized. Images showed that the TAMRA–P188 complex was found in the the cytosol but did not penetrate into the nucleus (see Fig. 2.7A). Further evidence showed that TAMRA diffused through the entire cell cytoplasm and the nucleus. It is evidence that P188 can be internalized and is therefore capable of interacting with cellular organelles.

Our results demonstrate that bTBI suppressed the expression of ZO-1, and that P188 treatment mitigates the loss of this tight junction protein. Assessing the permeability of BECs, we observed a significant reduction in the permeability coefficient in the P188-treated group, indicating a degree of restoration of the BBB characteristics and functionality. The restorative effects of P188 is attributed to the suppression of the MMP-2 & 9. Importantly, the treatment with P188 reduced the diffusion of molecules post-microcavitation, demonstrating the efficacy of P188

34

in attenuating bTBI. Also, the P188 treatment significantly decreased the expression of MMP-2 & 9 both in pre-and post-treatment (see Fig. 2.10B and C) and alleviates ZO-1 loss post-microcavitation. Taken collectively, these findings provide evidence to validating that P188 can restore the BBB integrity.
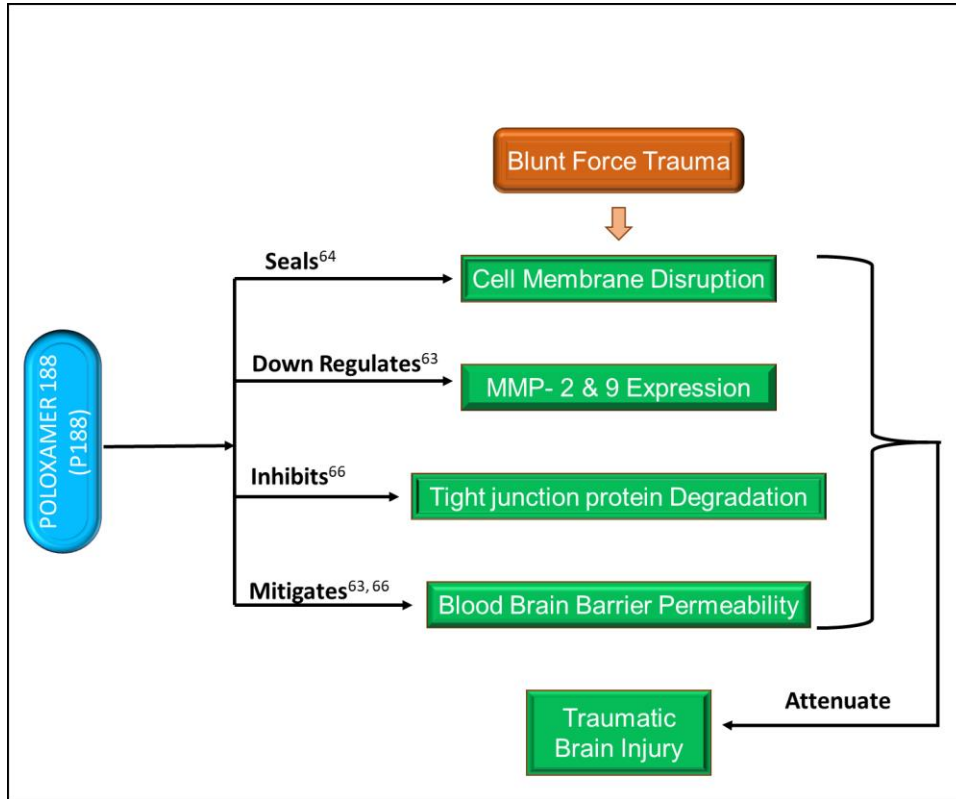
Figure 2. 13 - Schematics showing the possible mechanisms underlying the P188's BBB protection against traumatic brain injury. Blunt force trauma causes the up-regulation of MMP- 2 & 9 in the brain, which degrades the tight junction protein ZO-1, leading to an increased BBB permeability and brain damage. The BBB protection by P188 against traumatic brain injury is possibly through the down-regulation of MMP-2 & 9, which inhibits the degradation of tight junction protein ZO-1, thereby enhancing tight junction and attenuating traumatic brain injury.

2.5   CONCLUSION

In conclusion, we established and characterized an *in vitro* model of MPBMEC culture on the PETE membrane. Biotransport properties have been quantitatively determined and changes in the permeability coefficients due to chemical (e.g., TNF-a) or mechanical (microcavitation) have been

experimentally measured. The FDA-approved poloxamer P188 was shown to restore the permeability, which suggests the brain endothelium had been compromised but repaired by the P188 treatment. Such reparative effects of P188 are likely mediated by a suppression of MMP-2 & 9 and also by reestablishing the integrity of tight junction. These molecular events are postulated to attenuate the extent of damage caused by TBI (Fig. 2.13). Finally, the model designed, developed, and tested in this study is simple to engineer, effective, reproducible, and convenient to be used as a platform for therapeutic studies.

Chapter 3

AIM 2: <u>To investigate the structural and physiological role of GLUT-1 glucose transporter on brain endothelium barrier integrity and the impact of abnormal glycemia on neurons.</u>

3.1 <u>INTRODUCTION</u>

The blood-brain barrier (BBB) is a dynamic system that regulates the central nervous system (CNS) microenvironment [79] with a high degree of selectivity. The key players of the BBB are the tight junction proteins such as zonula occluding (ZO-1). The primary function of the brain endothelial cells (BECs) is to maintain the homeostasis of the brain. The colocalization of ZO-1 and glucose transporters (e.g., GLUT1), and enzymatic activities of BECs that metabolize harmful substances at the vascular face of the BBB [81] protects the CNS from external toxins within the circulation [80]. Nevertheless, this tight barrier can be breached either mechanically or biochemically. Recent evidence points to microcavitation and the overuse of psychostimulant drugs (PSDs) (e.g., cocaine and alcohol) to disrupt the function of BECs. The overall permeability of the blood-brain barrier is regulated by endothelial cells and their junctional complexes, which consist of adherens and tight junctions, and glucose transporters. The end-feet of astrocytes are in contact with the capillary wall and in communication with the neurons (Fig. 3.1). [72]. Microglia are also present for sensing neuronal injury and for detecting and fighting infection. Together, this unit regulates blood-brain barrier permeability and protects the integrity and function of the brain and central nervous system.
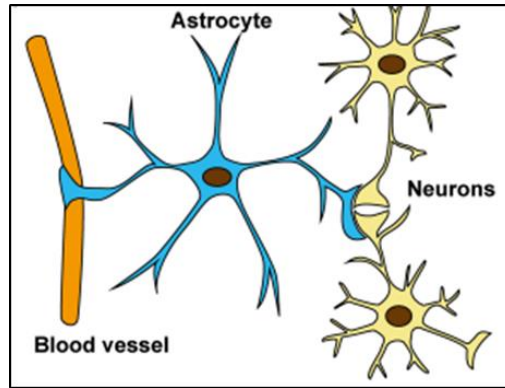
Figure 3. 1 Schematics of Astrocytes close morphological and functional associations with microvasculature and neurons. Showing location of astrocytes around blood vessels and neurons in the central nervous system.

The model we developed in Chapter 2 has potential to be applied in different brain diseased pathologies and from the evidence gathered from its applications, we suspected microcavitation, and PSDs disruption might be causing glucose transporters (e.g., GLUT1) depletion leading to unregulated flow of glucose into the brain; hence, exposing neurons to hyperglycemia. Hyperglycemia has been reported to increase reactive oxygen species (ROS), followed by alteration in the neuronal morphology, axonal degeneration in nerve fibers [73]. To test the theory of GLUT1 damage by microcavitation and PSDs and eventual exposure of neurons to hyperglycemia, we measured the permeability of BECs to Fluorescent 2-[N-(7-nitrobenz-2-oxa-1,3-diazol-4-yl) amino]-2-deoxy-D-glucose (2-NBDG) after exposure to two extreme concentrations of cocaine combined with 0.1% alcohol. The concentrations were chosen from our concentration-dependent study. Microcavitation, 20 uM cocaine + 0.1% alcohol, and 1 uM cocaine + 0.1% alcohol-induced changes in the permeability to the glucose analog were determined. The BECs barrier breakdown by microcavitation and the combination of cocaine and alcohol correlates with tight junction complex distortion. We demonstrate that the combination of poloxamer 188 (P188) and N-acetylcysteine (NAC) can repair the disrupted junctional complexes, decrease the paracellular permeability, and enhance neuron regeneration after exposure to a hyperglycemic condition. To reiterate the potential therapeutic treatments, poloxamer 188 is a triblock copolymer that was approved by the FDA for diverse biomedical applications [33], and N-Acetyl-L-cysteine (NAC) was also approved by the FDA to be used for the treatment of acetaminophen (paracetamol; N-acetyl-p-aminophenol) poisoning [107]. The mode of action of NAC in acetaminophen

overdose relies on the protection against oxidation and incorporation into the highly abundant intracellular antioxidant, glutathione (GSH).

Glucose is the major source of energy for most mammalian cells, particularly in the brain. The brain depends heavily on glycolysis, but the primary source of glucose comes from the blood and is dependent on transport through the BBB. Facilitative glucose transporter proteins mediate the passage of glucose into the brain. There are seven known isoforms of glucose transporters designated GLUT 1-7 [82]. GLUT1 and GLUT3 are the main isoforms found within the CNS that bring glucose into the cell through sodium independent transport mechanisms. A summary of the various GLUTs and their distribution within the CNS is shown in Figure 3.2. There are two forms of GLUT1 within the CNS, which differ only by the extent of glycosylation [83]. A glycosylated, 55 kDa GLUT1 is found primarily in the endothelial cells of the BBB while the non-vascular, non-glycosylated 45 kDa form is mainly found in neural cells as well as the basolateral plasma of epithelial cells isolated from the choroid plexus [82]. GLUT1 has also been detected in small cells with darkly stained nuclei characteristic of glial cells [84]. Immunohistochemistry staining and electron microscopy have shown positive detection of GLUT1 in astrocytes that are in direct contact with the cerebral microvessels of rat brain slices and dense distribution of GLUT1 within the astrocyte foot processes surrounding the microvessels of the gray matter and synaptic connections respectively [85]. GLUT1 is the primary glucose transporter in the BBB.
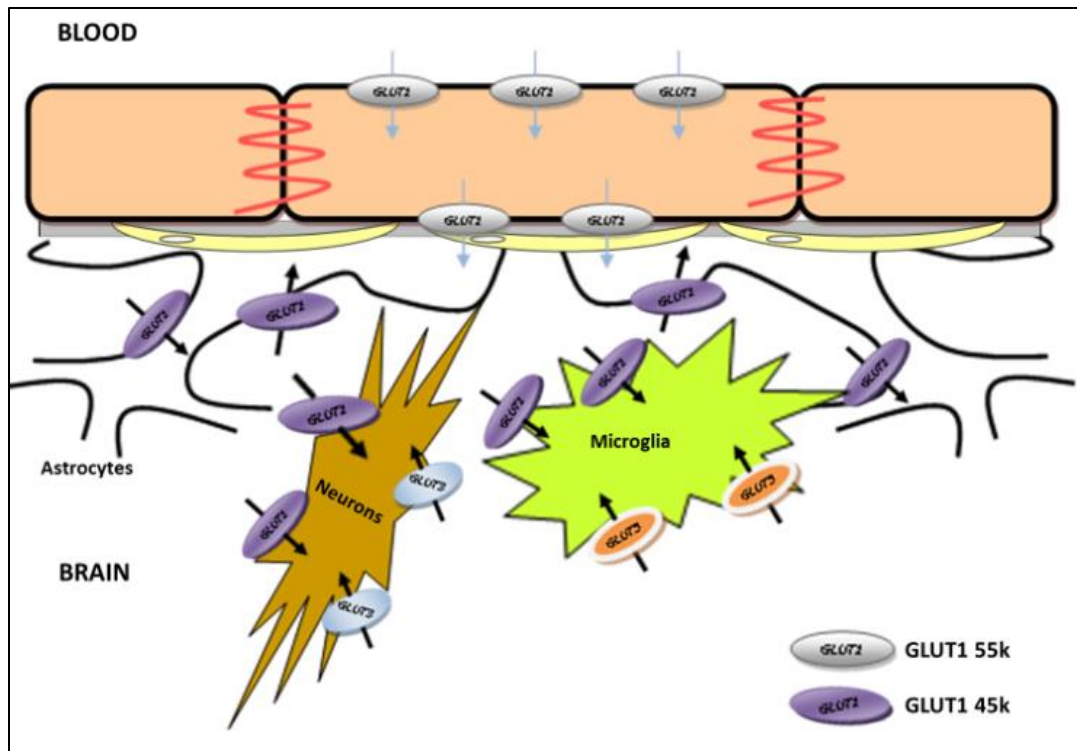
Figure 3. 2 - Schematics of Cellular localization of different isoforms of glucose transporter in the CNS.

GLUT1 is also highly expressed in the blood-retinal barrier, the placental barrier, and the blood-CSF barrier (BCSFB) [86-88] which highlights its importance in the regulation of glucose levels in these tissues. The rate-limiting step for glucose utilization in the brain is the transport of glucose through GLUT1 in the BBB and is highly responsive to metabolic changes within the brain. For instance, depending on the ambient concentration of hexose, GLUT1 expression in the BBB at both the mRNA and protein level can increase or decrease. A high concentration of hexose decreases the expression of GLUT1, while low hexose concentration causes an up-regulation of both GLUT1 mRNA and protein levels [89]. Both mRNA and protein levels of GLUT1 significantly increase following brain injury, such as a stroke and brain tumors [82, 84, 90]. Sodium-glucose cotransporter (SGLT) is also expressed by endothelial cells forming the BBB [91]. Compared to GLUT1, glucose transport through SGLT is sodium-dependent. A functional role for SGLT in glucose homeostasis in the brain is not well established. However, it has been speculated that SGLT helps maintain intracellular glucose levels in the brain under stressful conditions such as hypoglycemia [91].

Glucose transporters (GLUTs), specifically GLUT1, is colocalized with ZO-1 at the blood-brain barrier [92] to maintain a continuous high glucose and energy demands of the brain (Fig. 3.3). GLUT1 is prominent in the brain, and its expressions play a role in the distribution of hypoglycemia and hyperglycemia associated with diabetes and oxygen/glucose deprivation related to cerebral ischemia. A reduction in GLUTs at the blood-brain barrier occurs before the onset of the main pathophysiological changes. Mutations or alteration in GLUT1 by some recreational drug compounds alters the functionality of GLUT1 at the blood-brain barrier. Furthermore, glucose transporter isoform (GLUT1), as a BBB metabolic indicator [93], is downregulated in diseased endothelium while cerebral vascular adhesion molecules, such as vascular cell adhesion molecule (VCAM-1), are upregulated [94-96].
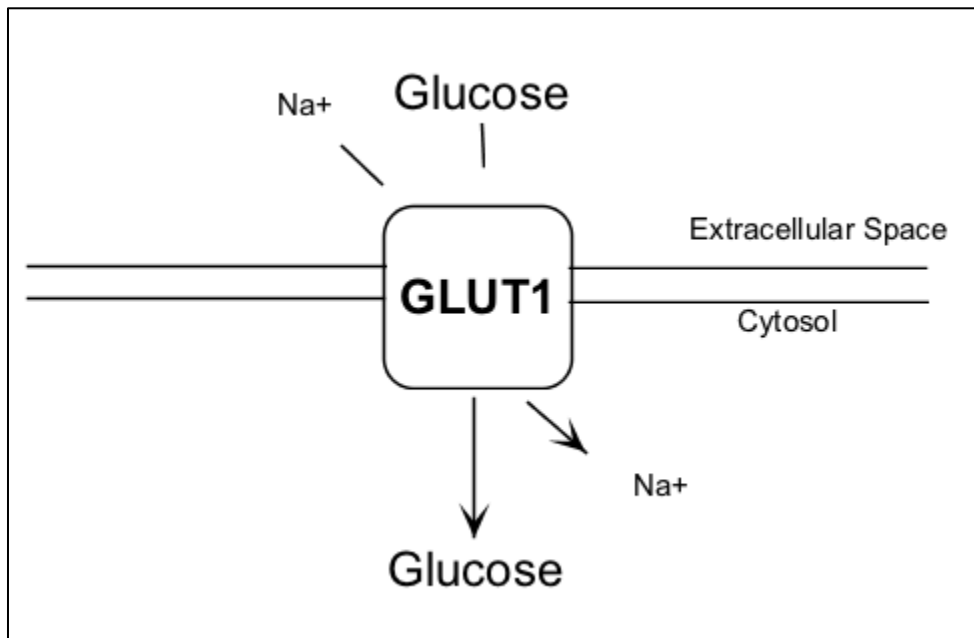
Figure 3. 3 - Schematics of GLUT 1 transporter

Cocaine-induced BECs dysfunction is characterized partially by the alterations in tight junction protein complexes [97]. Cocaine treatment also increases gene expression of some factors, including MMP-1, that contribute to basement membrane actin rearrangement resulting in stress fiber formation around cerebral vessels [98]. Continuous conformational changes in tight junction proteins and reorganization of basement membrane fibers weaken the BBB. alcohol abuse is associated with BBB impairment. Immunostaining shows diminished ZO-1 expression [99, 100].

Studies have shown that long-term alcohol abuse leads to functional and morphological changes in the CNS, regardless of nutritional status [74], and therefore, can enhance the oxidative injury of BECs. The combined frequent use of cocaine and alcohol can cause detrimental effects to the BBB and brain cells, including hyperglycemia [79]. Hyperglycemia is a trigger of diabetic complications [102], which eventually leads to diabetic neuropathy [101]. Exposure of neurons to high glucose concentrations is considered a determinant of diabetic neuropathy [103]. Neuronal cellular damage caused by hyperglycemia is known as glucose neurotoxicity [104]. Long-term high levels of serum glucose in diabetes have been proved to promote the generation of intracellular reactive oxygen species (ROS), neuronal injury, and even neuronal cell apoptosis [105, 106]. However, the molecular basis of how hyperglycemia alters neuronal functions is yet to be elucidated.

In summary, a proper understanding of the alterations of the structure and function of neurons in hyperglycemia-treated cultures appears to be of great importance for translational research. In this study, endothelial cell ZO-1, GLUT1, neuron microtubules expression and arrangement, upregulations in ROS, cell viability/apoptosis were investigated.

3.2   MATERIALS AND METHOD

3.2.1   Cell Culture

MPBMECs (passages between 3 to 6) were seeded on fibronectin-coated glass slides at a cell density of 4×10^4 cells/cm^2 in EBM-2 basal medium (Lonza) supplemented growth factors, antibiotic, and maintained at 37°C with 5% CO_2 environment. The medium was changed every three days until the cells reached confluence. MPBMECs monolayer integrity at confluence was confirmed by the expression of endothelial cell tight junction markers.

3.2.2   Evaluation of Brain Endothelial Cells Integrity

Effects of alcohol and cocaine on BBB integrity were assessed by measuring paracellular permeability (luminal to abluminal) to glucose analog. MPBMECs monolayers seeded on customized inserts were exposed to a selected concentration of cocaine (1 uM and 20 uM) in combination with alcohol (0.1%) for 1 hr. at 37°C in a humidified incubator before the addition of

a mixture of glucose analog in PBS to the luminal compartment. Abluminal samples (20 μL) were collected over 3 hr and replaced with an equal volume of fresh media. The diffusion coefficient was determined by fluorescent measurements at 475 nm and 535 nm excitation and emission wavelengths, respectively. Culture inserts with and without cells were used as controls.

3.2.3 Characterization of GLUT1 and ZO-1

For GLUT1 and ZO-1 expressions, MPBMECs were cultured on glass coverslips until 80-100% confluent and then treated with cocaine (1, 2.5, 5, 10, 20 μM), (20 μM cocaine + (0.1%) alcohol), and (1 μM cocaine + (0.1%) alcohol) for 24 hours. Fixed in 4% paraformaldehyde, permeabilized in (0.3% Triton X-100 for 3 minutes, blocked with 3% bovine serum albumin at room temperature for 1 hr and incubated with Alexa Fluor 555 and 488 conjugated GLUT-1 and ZO-1 antibody respectively. After that, cells were rinsed and counterstained with DAPI. Rinsed, mounted, imaged, and analyzed. For neurons and astrocytes, cells were cultured until day 7 and then doubled stained following the protocol above using anti-beta Tubulin Class III Alexa Fluor 488 and GFAP Alexa Fluor 570. Nuclei were stained with DAPI.

3.2.4 In vitro Glucose uptake

This method is well described by Itoh et, al [108] by using Fluorescent 2-[N-(7-nitrobenz-2-oxa-1,3-diazol-4-yl) amino]-2-deoxy-D-glucose (2-NBDG), a glucose analog to measure the glucose uptake. Briefly, cells were preincubated for 15 minutes with HBSS containing 2 mM glucose in air/5% CO_2, the preincubation medium was replaced by HBSS with 2 mM glucose containing 2-NBDG (50 μM), and incubation was continued for either 0, 5, 15, 25, 35, 45, and 60 minutes. At the end of the incubation, the reaction mixture was replaced by fresh HBSS with 2 mM glucose, and incubation was continued for 5 minutes to allow efflux of residual nonphosphorylated 2NBDG from the cells. The cell layers were washed three times with HBSS containing 2 mM glucose. Fluorescence imaging was performed at excitation and emission wavelengths of 475 nm and 535 nm, respectively. Fluorescence intensity of standardized concentrations of 2NBDG, each of which filled a culture dish without cells, was measured for calibration. Glucose uptake in cultured endothelial cells in each dish was calculated by averaging fluorescence intensity. To test the effect of repetitive use of cocaine and alcohol, cells were treated with (20 μM cocaine), (1 μM cocaine),

(20 μM cocaine + (0.1%) alcohol), (1 μM cocaine + (0.1%) alcohol) daily for three days and then glucose uptake and fluorescent intensity was measured.

3.2.5   Measurement of Mitochondrial Reactive oxygen species (ROS) in BECs

In this study, ROS was measured using a MitoSOX™ Red mitochondrial superoxide indicator, according to the manufacturer's instructions. Briefly, BECs were cultured on glass cover slides. After treatments with cocaine, alcohol, and in combination, the cells were incubated with 1 μM MitoSOX™ reagent working solution for 30 min under room temperature in the dark. After washing three times with PBS, the fluorescence was imaged with a fluorescent microscope.

3.2.6   Endothelial Cell Viability

Endothelial cell exposed to cocaine (20 uM) + alcohol (0.1%) and cocaine (1 uM) + alcohol (0.1%) were analyzed for viability using LIVE/DEAD Cell Imaging Kit (Life Technologies) according to the manufacturer's instructions. Brief, endothelial cells were first exposed to cocaine (20 uM) + alcohol (0.1%) and cocaine (1 uM) + alcohol (0.1%) with or without P188, NAC, and P188 + NAC; the Live Green and Dead Red reagents were then mixed to prepare 2X stock and added to the cells at room temperature for 15 min. The cells were subjected to fluorescence imaging. Cells with green fluorescence signal represent live cells, while cells with red fluorescence signal represent dead cells.

3.2.7   Cortical neuron isolation and culture

Cortical neurons were prepared from E18 embryos of a mouse. The cortex was dissected and dissociated using trypsin and plated on glass cover slide in Petri dishes precoated with poly-L-lysine (PLL) overnight in 4°C. Cells seeded at the cell density of $5x10^5$ or 2.5×10^5/glass slide in a volume of 100 ul were maintained in Neurobasal culture media supplemented with 1X B27, penicillin, and L-glutamine. Cells were cultured for five days before being used in experiments. These experimental protocols of isolating mouse cortical neurons were provided by Dr. Young-Tae Kim in the Department of Bioengineering at the University of Texas at Arlington and his laboratory personnel.

3.2.8 Characterization and induction of hyperglycemia

Culture media was changed to treatment media (with higher concentrations of glucose). The purity of neuronal cells was detected by double fluorescent labeling of beta III Tubulin and GFAP. Counter stained with DAPI. Neurons were cultured in culture media for an additional 1 day at different experimental conditions before observation. Neurobasal medium has 25 mM glucose concentration, which is optimal for DRG neurons survival and growth, so we consider this glucose concentration as normal. Mannitol glucose at different concentrations was added to the Neurobasal medium to create Hyperglycemic conditions. The cells exposed to either hypo or hyperglycemic conditions were then incubated for an additional 1 day with P188, NAC, or P188 +NAC added to the culture media. In the end, cells were double fluorescent-labeled for beta III Tubulin and GFAP. Counter stained with DAPI.

3.2.9 Neurospheroid measurements after exposure to hyperglycemic conditions

The diameter of neurospheroids were manually determined from optical microscope images using a commercial Nikon software (NIKON-ND2). The spheroid measurement was replicated three times and then averaged.

3.2.10 Validation of apoptotic neural cell death

Nuclear morphological change of cortical neurons exposed hyperglycemia for 24 h was observed by using DAPI staining, which is a fluorescent stain for labeling DNA. Briefly, cortical neurons were fixed with 4% paraformaldehyde for 15 min and stained with DAPI for 10 min at room temperature in the dark, then washed twice with PBS and assessed under a fluorescent microscope.

3.2.11 Evaluation of neuron cell viability

Neuron cells exposed to different concentrations of glucose and then treated with P188, NAC, or both were analyzed for its cell viability using LIVE/DEAD Cell Imaging. Briefly, neuron cells were first exposed to normal or hyperglycemic media with or without P188, NAC, and P188 + NAC; the Live Green and Dead Red reagents were then mixed to prepare 2X stock and added to the cells at room temperature for 15 min. The cells were fixed with paraformaldehyde and then subjected to fluorescence imaging. Cells with green fluorescence signal represent live cells, while cells with red fluorescence signal represent dead cells.

3.2.12 Measurement of Mitochondrial Reactive oxygen species (ROS) in neurons

In this study, ROS was measured using a MitoSOX™ Red mitochondrial superoxide indicator, according to the manufacturer's instructions. Briefly, cortical neurons were cultured on glass cover slides. After treatments with different glucose concentrations, the cells were incubated with 1 µM MitoSOX™ reagent working solution for 30 min under room temperature in the dark. After washing three times with PBS, the fluorescence was imaged with a fluorescent microscope.

3.2.13 Statistical analysis

All data analysis was executed using one-way and two-way ANOVA (R-Studio Software) to analyze differences between group(s) with one or more independent variables. $p < 0.05$ was considered a significant difference. *Post hoc* analysis was done using Tukey's honest significant difference (HSD). All data were reported as mean $\pm$ standard deviation.

3.3   RESULTS

3.3.1   Effects of microcavitation, cocaine, and alcohol, on BBB integrity

To determine the effect of microcavitation and PSDs on GLUT1 with respect to BECs integrity, we measure the permeability of brain endothelial cells to 2-NBDG a fluorescent glucose analog after exposure to microcavitation and cocaine + alcohol. Permeability was measured over 120 min time window following the addition of 2-NBDG. As shown in Figure 3.4, the permeability coefficient following exposure significantly increased to $8.86 \pm 0.90 \times 10^{-3}$ cm/s, compared to the control value, $1.27 \pm 0.85 \times 10^{-3}$ cm/s. The exposure of cells to (20 uM cocaine + 0.1% alcohol) and (1 uM cocaine + 0.1% alcohol) also increased the permeability significantly, $4.43 \pm 0.77 \times 10^{-3}$ cm/s and $3.17 \pm 0.82 \times 10^{-3}$ cm/s respectively. This is about 2 to 3-fold higher than the control. These results strongly suggest that exposure to microcavitation and cocaine + alcohol can affect the integrity of the BBB, leading to the excess flow of glucose to the brain (hyperglycemia). Interestingly, when cells were exposed to either repetitive 5 blasts, 20 uM cocaine + 0.1% alcohol, or 1 uM cocaine + 0.1% alcohol and were treated with P188 + NAC, there were significant decreases in the permeability of fluorescent glucose analog (Fig. 3.4). Permeability following a combined treatment of P188 + NAC to cells exposed to microcavitation (5 blasts) decreased by

about 20%. The permeability of cells treated with P188 + NAC after (20 uM cocaine + 0.1% alcohol) and (1 uM cocaine + 0.1% alcohol) exposure both decreased by 43% and 40%, respectively.
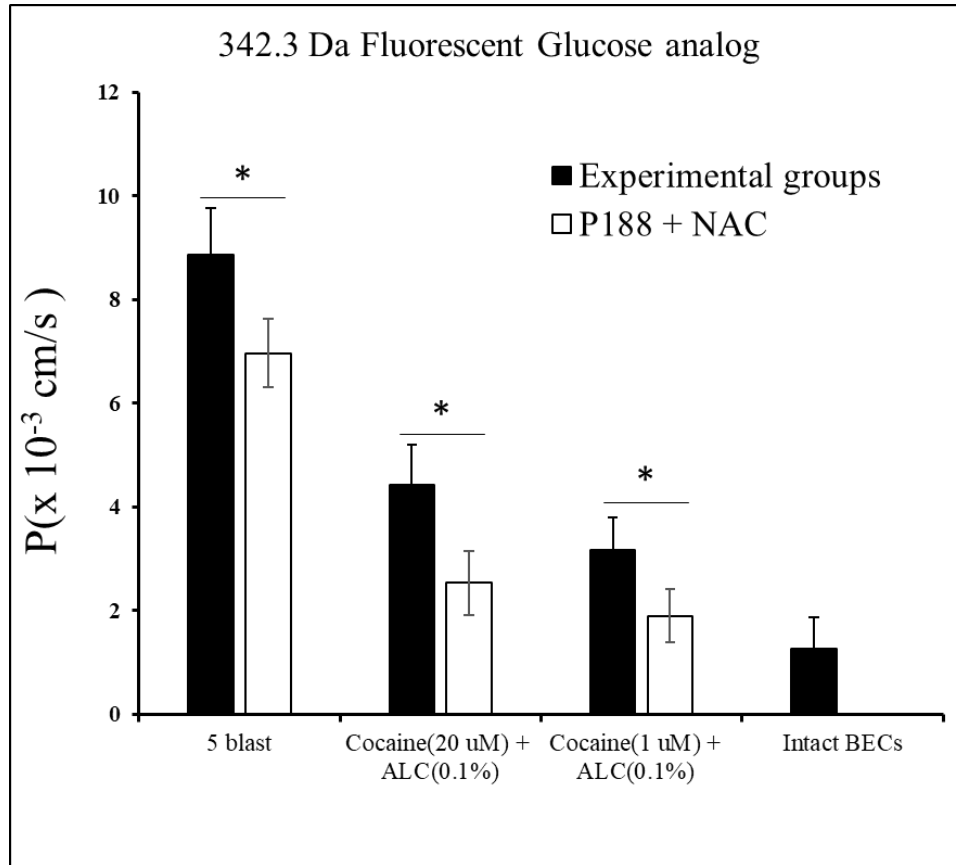
Figure 3. 4 - Permeability coefficients measured using 342.3 Da Fluorescent Glucose analog after exposure to microcavitation, cocaine + alcohol (ALC), and attempted reversal of the disrupted BECs tight junctions using P188, NAC, and P188 + NAC, n = 4.

3.3.2   Effects of cocaine and alcohol on GLUT1 expression

To investigate the effect of cocaine and alcohol on GLUT1, we exposed the cells to different concentrations of cocaine ranging from 1 to 20 uM for dose-dependent studies (Appendix 2) before picking two different concentrations to combine with 0.1% alcohol. Immunocytochemistry shows fluorescent expression of GLUT1 (Fig. 3.5A), ZO-1 (Fig. 3.5B), and colocalization of ZO-1 and GLUT1 (Fig. 3.5C). For the dose-dependent studies, fluorescent images indicate a substantial decrease in GLUT1 expression in BECs as cocaine concentration increases from 1 to 20 μM

47

(Appendix 2) between 5 to 60 minutes compared to control cells (Fig. 3.5A-C). Colocalization of GLUT1 protein with ZO-1 indicates an intracellular localization of GLUT1 protein in BECs. Following the cocaine treatment results (Appendix 2), we combined 20 μM cocaine with 0.1% alcohol (cocaine, 20 μM + 0.1% alcohol) (Fig. 3.6) and 1 μM cocaine with 0.1% alcohol (cocaine, 1 μM + 0.1% alcohol) (Fig. 3.7) and fluorescent images showed significant reduction in GLUT1 expressions followed by ZO-1 compared to control cells (Fig. 3.5A-C).
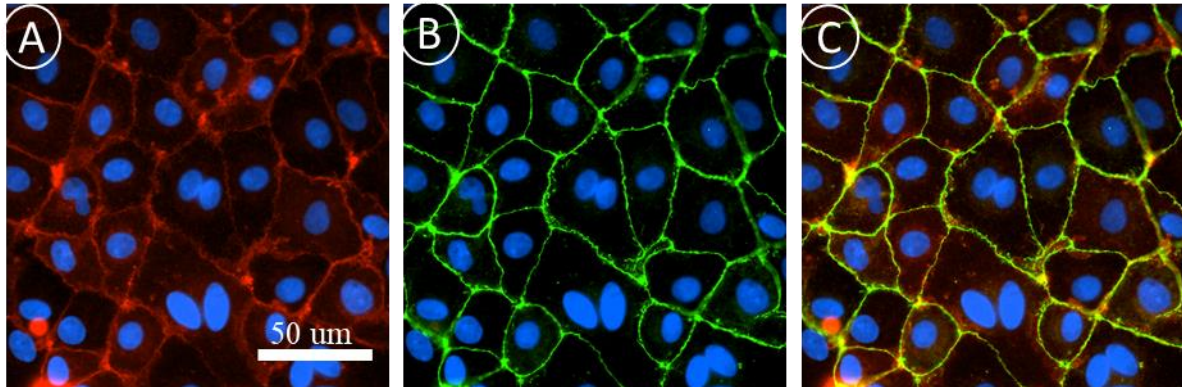
Figure 3. 5 - Characterization of Brain cells: Colocalization of GLUT-1 & ZO-1. Fluorescent staining of (A) GLUT-1, (B) ZO-1, and (C) merged image of brain endothelial cells. Counter stained with DAPI.
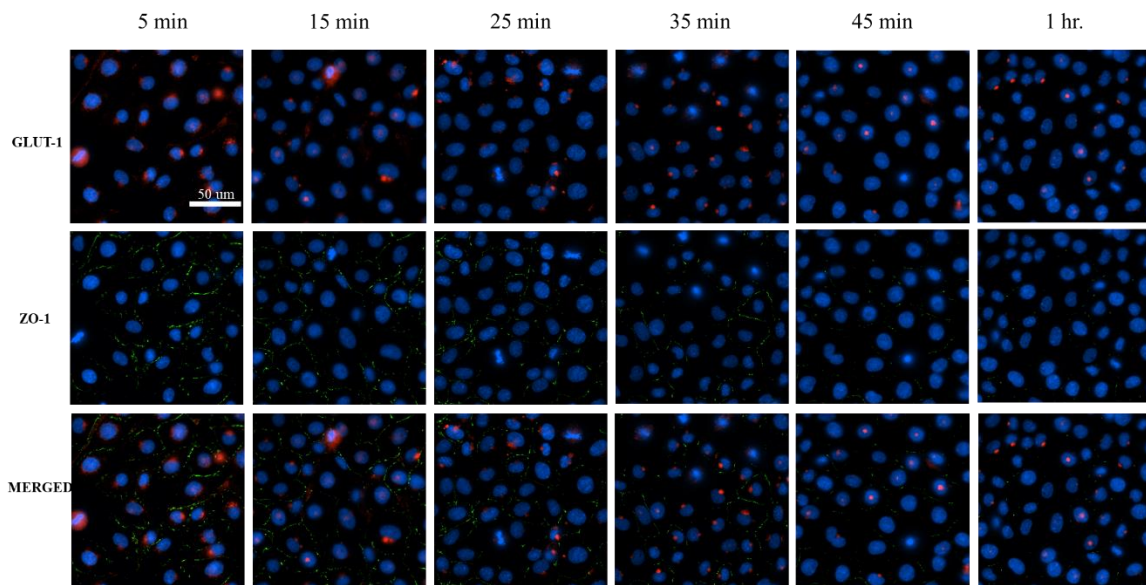
Figure 3. 6 - Combinatory effects of cocaine (20 uM) and alcohol (0.1%) on ZO-1 expression in mouse primary brain microvascular endothelial cells (MPBMECs): Disruption of GLUT-1 affects

the integrity of brain endothelium (BE). Immunofluorescent expression of GLUT-1(red), ZO-1 (green) and merged image in MPBMECs. DAPI (blue-nuclei).
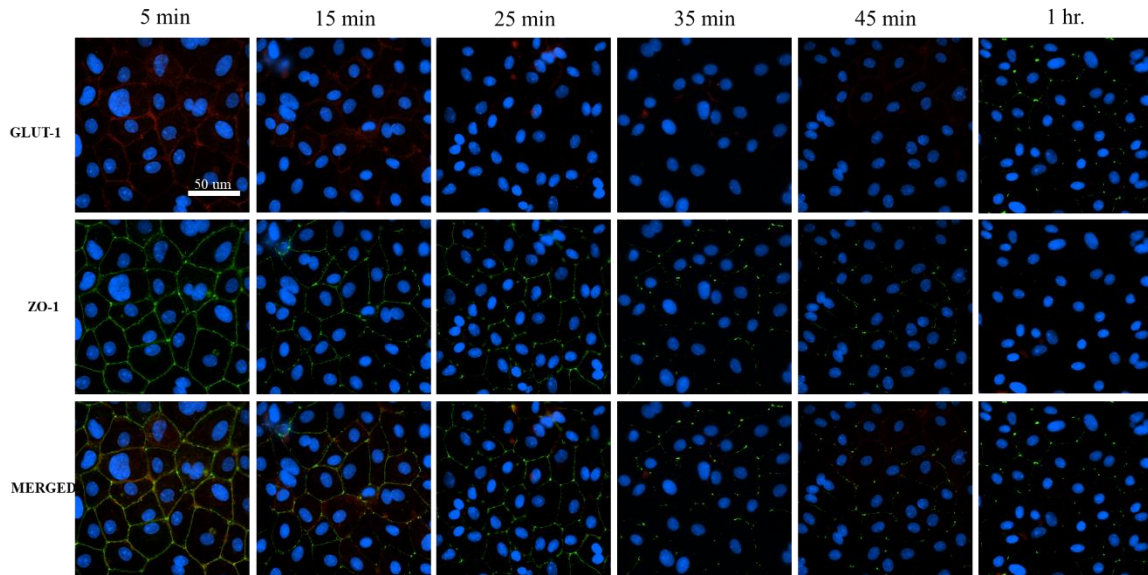
Figure 3. 7 - Combinatory effects of Cocaine (1 uM) and alcohol (0.1%) on ZO-1 expression in mouse primary brain microvascular endothelial cells (MPBMECs): Disruption of GLUT-1 affects the integrity of brain endothelium (BE). Immunofluorescent expression of GLUT-1(red), ZO-1 (green) and merged image in MPBMECs. DAPI (blue – nuclei).

3.3.3   Effects of cocaine and alcohol glucose Uptake by Endothelial cells

To investigate the effects of cocaine and alcohol on brain endothelial cells (BECs) glucose uptake, we first investigated a time-dependent uptake. Cells were incubated with glucose analog to study glucose uptake, and images of phosphorylated 2-NBDG in BECs are shown in Fig.3.8. After incubation with 50 μM 2-NBDG for either (A) 0, (B) 30, (C) 60, and (D) 90 min, the cells were washed three times to remove non-phosphorylated 2-NBDG, and fluorescence intensity derived from phosphorylated 2-NBDG in BECs increased with increasing incubation time (Fig. 3.8). The experiment was replicated in triplicate, and the average fluorescence intensity for each incubation time was measured. (graph in Fig. 3.8E.) Fluorescence intensity increased proportionately to incubation time. BECs exposed to cocaine, alcohol, and cocaine + alcohol were subjected to the same glucose uptake protocol described above for (A) 30, (B) 60, and (C) 90 min, and images of phosphorylated 2-NBDG in BECs (Fig. 3.9) were recorded. Fluorescence intensity derived from phosphorylated 2-NBDG also increased with incubation time, but average fluorescence intensity

for each incubation time measured was significantly lower compared to when the cells were not exposed to cocaine nor alcohol (graph in Fig. 3.9). To examine the effect of daily or repetitive use of cocaine (1 μM), alcohol (0.1%), and in combination, we exposed the cells to 1 uM of cocaine, 0.1% of alcohol, and 1 uM of cocaine + 0.1% of alcohol for about 60 minutes daily for three days. Finally, the glucose uptake protocol described above was followed. Fluorescence intensity derived from phosphorylated 2-NBDG also increased with incubation time (Fig. 3.10) as expected, but average fluorescence intensity for each incubation time measured was significantly lower compared to control (graph in Fig. 3.10).
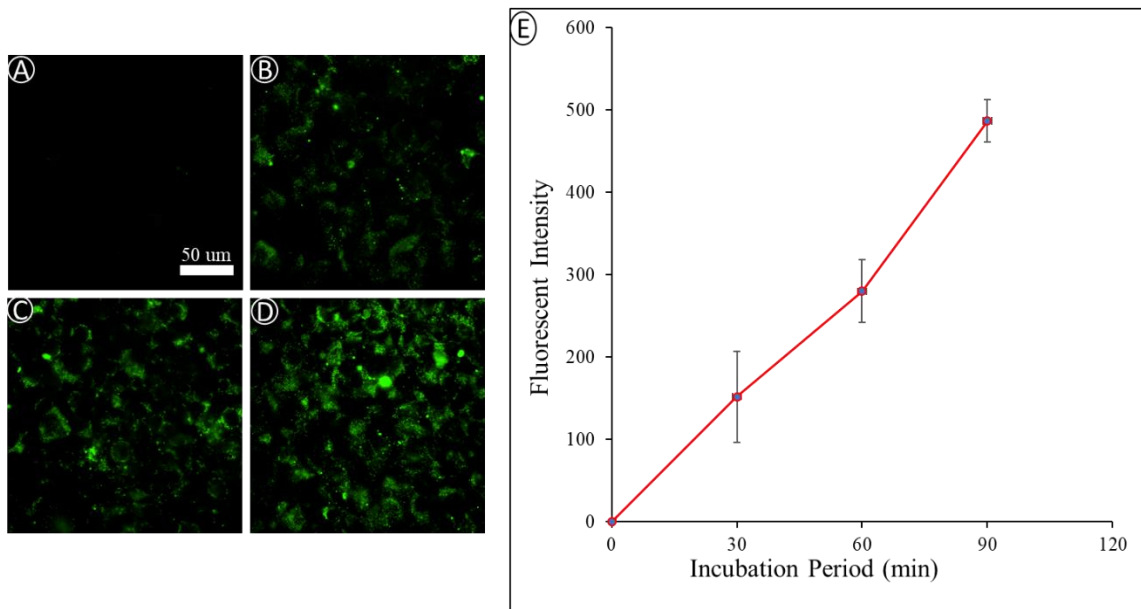
Figure 3. 8 - Control study of Glucose uptake by Primary Brain Microvascular Endothelial Cells using fluorescent glucose analog (D-Glucose, 2-deoxy-2-((7-nitro-2,1,3-benzoxadiazol-4-yl) amino) (2-NBDG). 2-NBDG was Phosphorylated in endothelial cells (ECs). Cells were incubated with 2-NBDG for either (A) 0, (B) 30, (C) 60, and (D) 90 minutes and then washed to remove any unmetabolized residual dye. (E) Fluorescence intensity derived from phosphorylated 2-NBDG in the ECs increases with the incubation time. Scale bars = 50 um, n = 6.
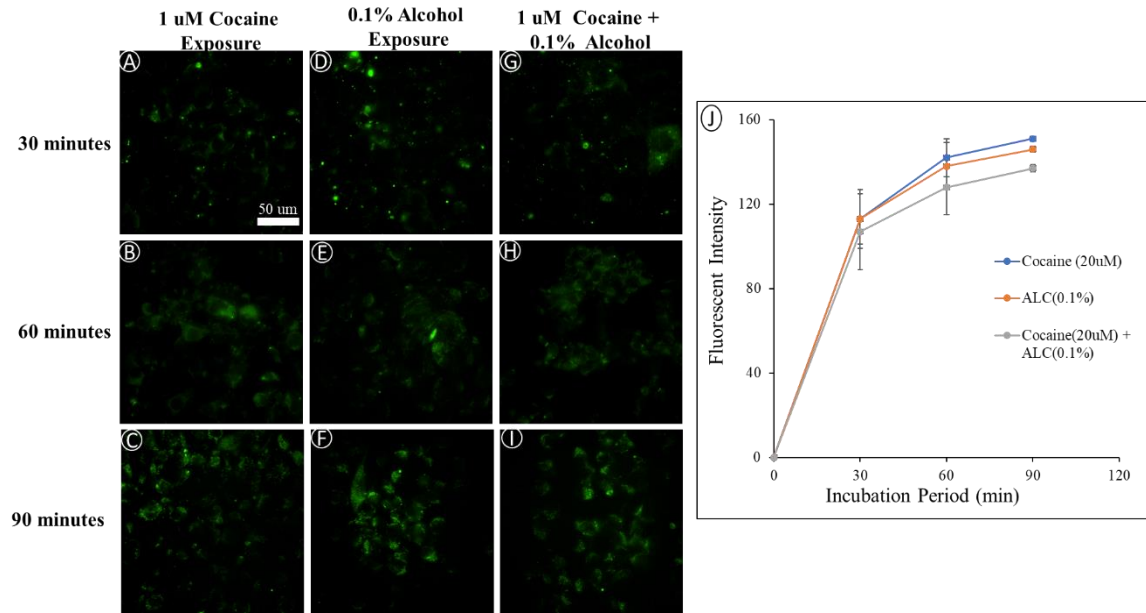
Figure 3. 9 - Cells were exposed to 1 uM of cocaine (A-C), 0.1% of alcohol(ALC) (D-F), and in a combination of both (G–I) for 1 hour and then glucose uptake was measured for 30, 60, and 90 using 2-NBDG. (J) Fluorescence intensity derived from phosphorylated 2-NBDG in the EC increased with incubation time but lower than the control. Scale bars = 50 um, n = 3.

51
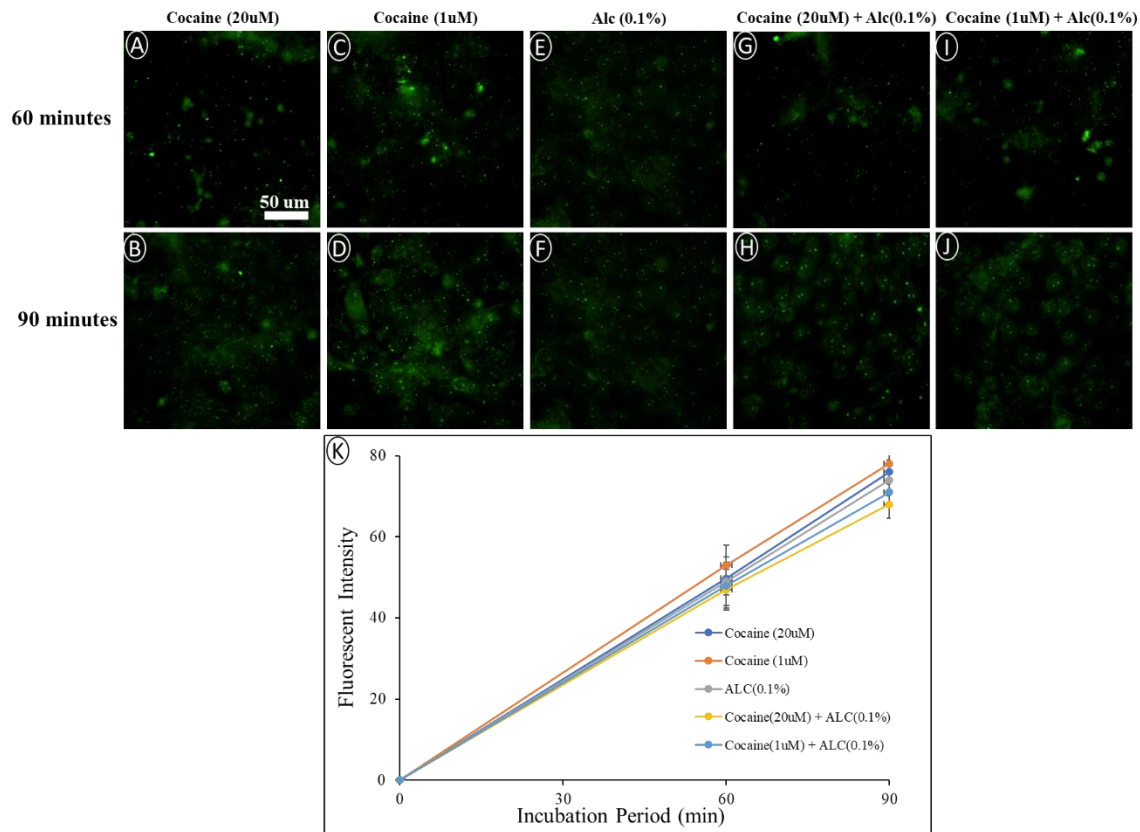
Figure 3. 10 - Cells were exposed to cocaine, alcohol (ALC), and in a combination daily for three days, and then glucose uptake was measured after 90 minutes incubation period using 2-NBDG. 20 uM of cocaine (A - B), 1 uM of cocaine (C - D), 0.1% of alcohol (E - F), 20 uM of cocaine + 0.1% of alcohol (G – H), 1 uM of 20 uM of cocaine + 0.1% of alcohol (I – J) were used for the treatment. Fluorescence intensity derived from phosphorylated 2-NBDG in the ECs increased with the incubation time but lower than the control (K). Scale bars = 50 um, n = 10.

3.3.4 BECs Cocaine and alcohol exposure increases ROS generation

To determine the effects of cocaine and alcohol in inducing excess production of reactive oxygen species (ROS), BECs were incubated with 20 uM of cocaine, 1 uM of cocaine, 0.1% of alcohol, (20 uM of cocaine + 0.1% of alcohol), and (1 uM of cocaine + 0.1% of alcohol) for 6 and 24 h. There was an increase in the expression of superoxide generation after 6 h (Fig. 3.11A - E), but the expression was reduced after 24 h (Fig. 3.1F - J). Changes in the fluorescent intensity are depicted in the graph (Fig. 3.11K).
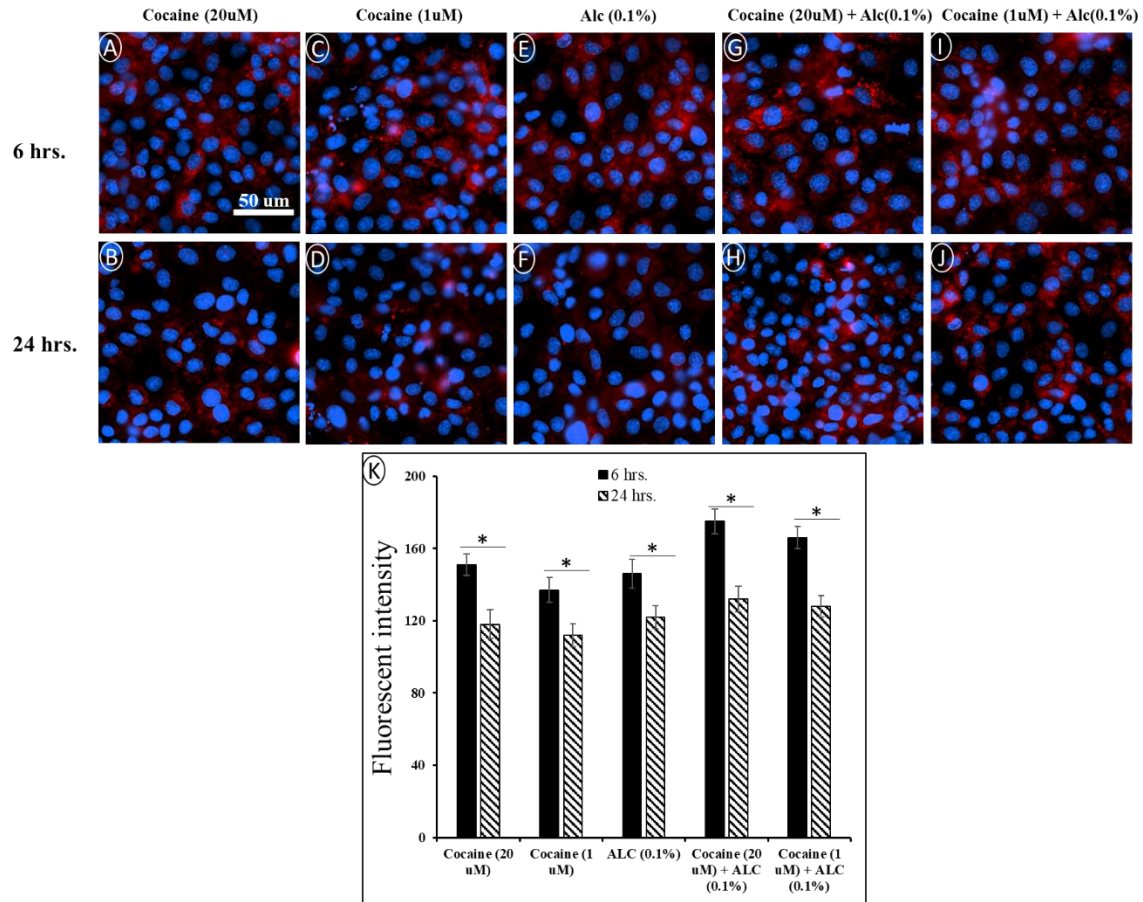
Figure 3. 11 - Injured brain endothelial cells show high levels of superoxide in response to cocaine, alcohol (ALC), and in a combination. 20 uM of cocaine (A - B), 1 uM of cocaine (C - D), 0.1% of alcohol (E - F), 20 uM of cocaine + 0.1% of alcohol (G - H), 1 uM of cocaine+ 0.1% of alcohol (I – J). Nuclei were stained with DAPI (blue). (K) Fluorescence intensity of superoxide expression was quantified, n = 6.

3.3.5 BECs Cocaine and alcohol exposure reduces cell viability over time

To determine endothelial cell viability after exposing BECs to cocaine and alcohol, cells were incubated with 20 uM of cocaine, 1 uM of cocaine, 0.1% of alcohol, (20 uM of cocaine + 0.1% of alcohol), and (1 uM of cocaine + 0.1% of alcohol) and the absorbance was measured using plate reader after 6 and 24 h of incubation. Reduction in the BECs viability was observed in both time points (Fig. 3.12) which explains why we observed ROS expressions in Figure. 3.11.
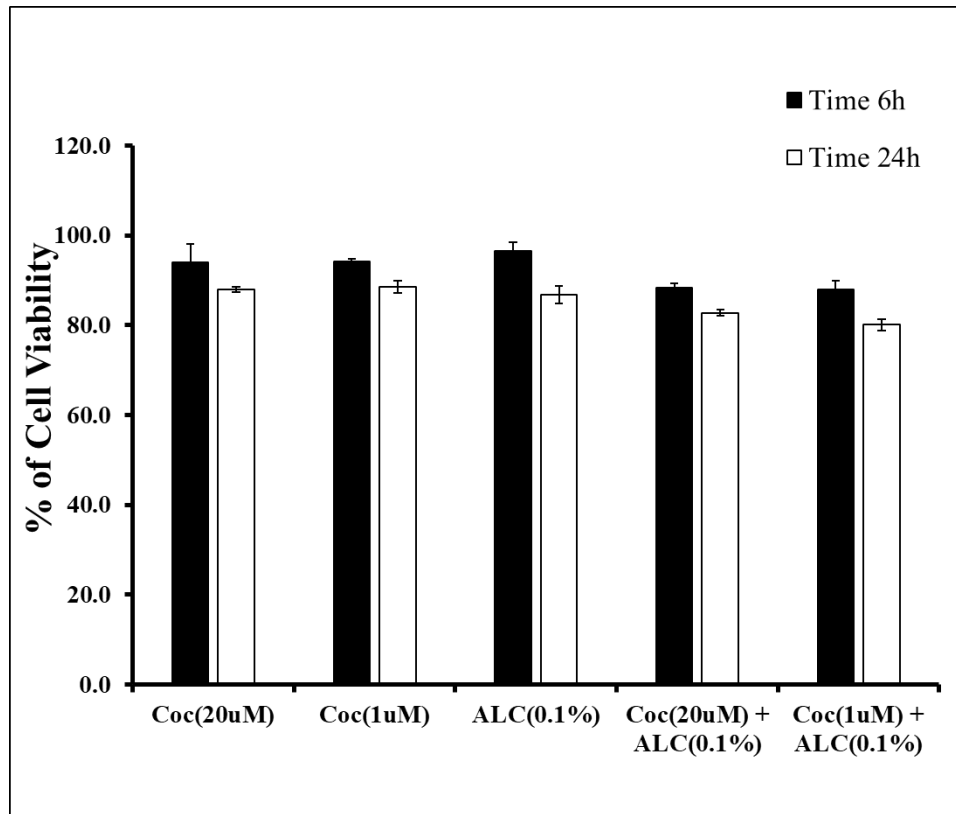
Figure 3. 12 - Injured brain endothelial cells show reduction in viability in response to cocaine, alcohol (ALC), and in a combination as described in figure 11, n = 6.

3.3.6 Evaluating the responses of cortical neurons to hyperglycemia

To examine some key characteristics relating to neuronal cell morphology, we cultured the cells up to seven days and then used immunolabeling to observe the structure and morphology. Both control (Fig. 3.13) and hyperglycemic-exposed neurons displayed the morphology of mature neurons and were positive for labeling with beta III tubulin, a widely used marker for neurons. Moreover, detailed fluorescent microscopy indicated that neurons showed similar ultrastructural characteristics as those previously described [125]. Finally, the glial contamination was significantly low (less than 0.5%), which agrees with the above-mentioned studies. On the other hand, we observed that hyperglycemic exposure reduced the expression of the neural network, size, and homogeneity of neurospheroids (Fig. 3.13B - C). Intriguingly, when the cells were treated with either P188 or NAC for one day, we observed the restoration of neurospheroids and realignment of the neural network (Fig. 3.13D - G). More interesting, P188, in combination with

NAC, showed a significant recovery in the neuron morphology (Fig. 3.13H - I) compared to control (Fig. 3.13A).
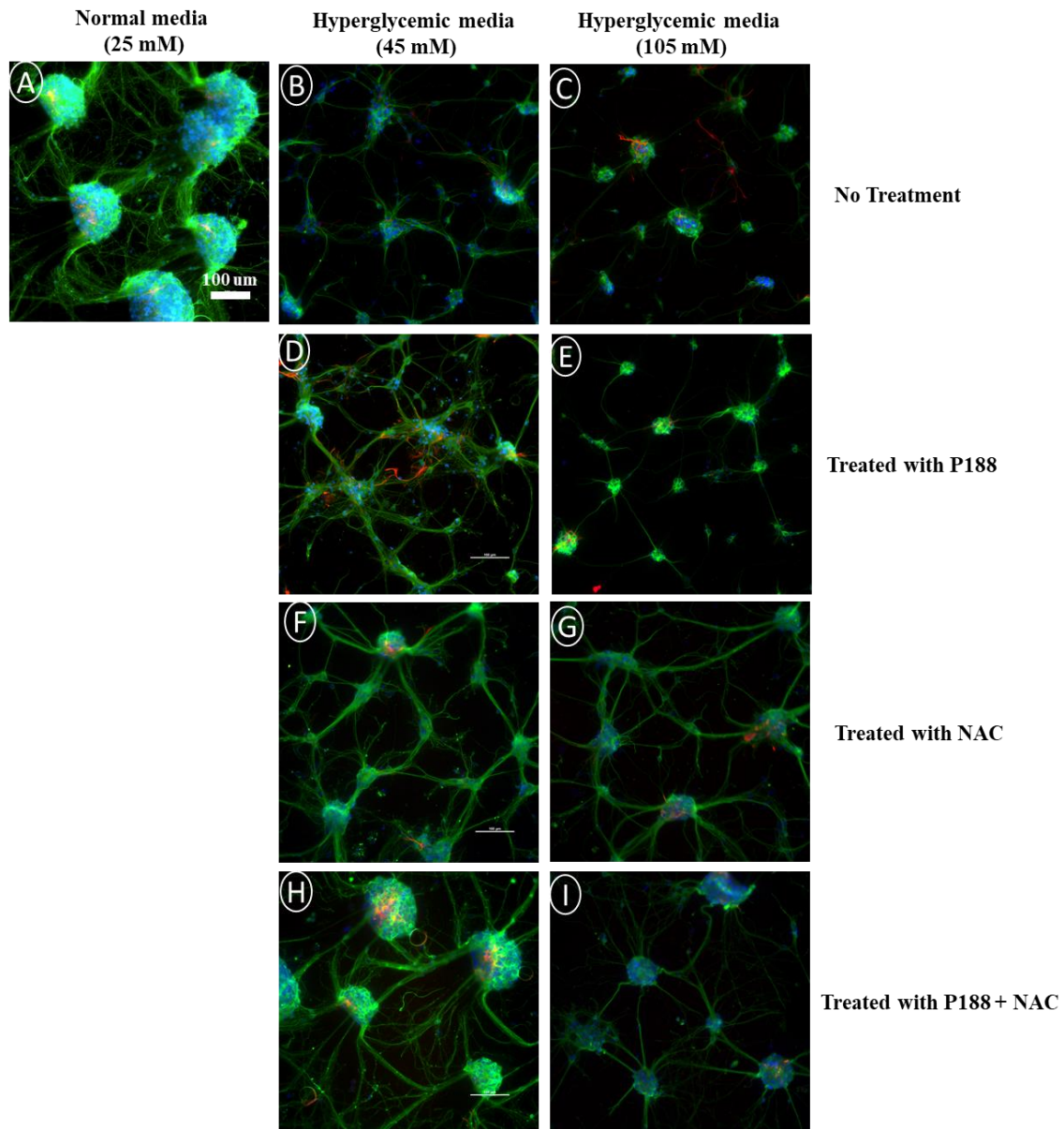
Figure 3. 13 - Double fluorescents labeling of beta III Tubulin (Green) and GFAP (Red) for E18 rat embryonic cortical neurons and astrocyte, respectively. (A) control, (B - C) Neurons exposed to different levels of hyperglycemic conditions. (D - E) cells treated with P188, (E - G) cells treated with NAC, and (H - I) cells treated with P188 + NAC after exposure to hyperglycemic conditions. Nuerospheroids restored in groups treated with P188, NAC, or in combination. Counter stained with DAPI. Notice the formation of homogenously sized neurospheriods in control cells. (n = 3, Scale bar = 100 um).

3.3.7 Neurospheroid Measurement

To access changes in the neurospheroid sizes caused by hyperglycemia, we measured the diameter of the spheroids from the neuron cells characterized above (Fig. 3.13). Nikon software (ND2) was used to generate the diameter of the spheroids. Spheroids diameter from the control were determined with minimal variability ($157.13 \pm 19.13 \, \mu m$) (Fig. 3.14). Following exposure to glycemic conditions, the heterogeneity in size of the spheroids increased and, in some cases, the neurospheroids become distorted to irregular shape (Fig. 3.13B and C) and (Fig. 3.14). However, treatment with P188, NAC or both restored the spheroid shape and size in cells exposed to hyperglycemic conditions (Fig. 3.13H) and (Fig. 3.14A). In contrast, an extreme hyperglycemic condition (105 mM) did not completely restore the shape or size (Fig. 3.13I) and (Fig. 3.14B).
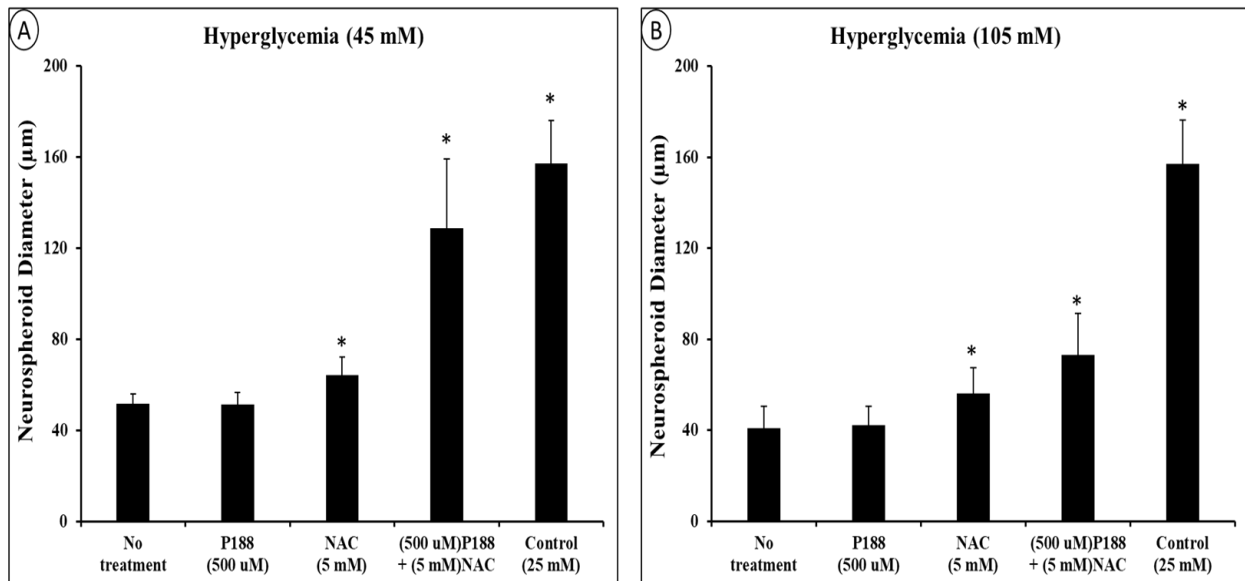
Figure 3. 14 - Quantifications of the effect of poloxamer 188 (P188), N-acetylcysteine (NAC), and P188+NAC treatments on neurospheroids size in a 2D array culture after hyperglycemia exposure. (A) hyperglycemia (45 mM) and (B) hyperglycemia (105 mM). All experimental groups were compared to the no treatment group. p < 0.05, n = 3.

3.3.8 Apoptosis induced by different levels of hyperglycemia

To determine the extent of neuronal apoptosis possibly induced by hyperglycemia exposure, the fragmentation of DNA, (a marker for apoptosis) was analyzed with DAPI staining after 24 h exposure to different levels of hyperglycemia. After DAPI staining, the nuclei in the control group were regular in shape while the nuclei in the different levels of hyperglycemia were highly

condensed and fragmented, likely a morphological indication apoptosis (Fig. 3.15A - C). The cell viability was determined and shown in Figure 3.15D.
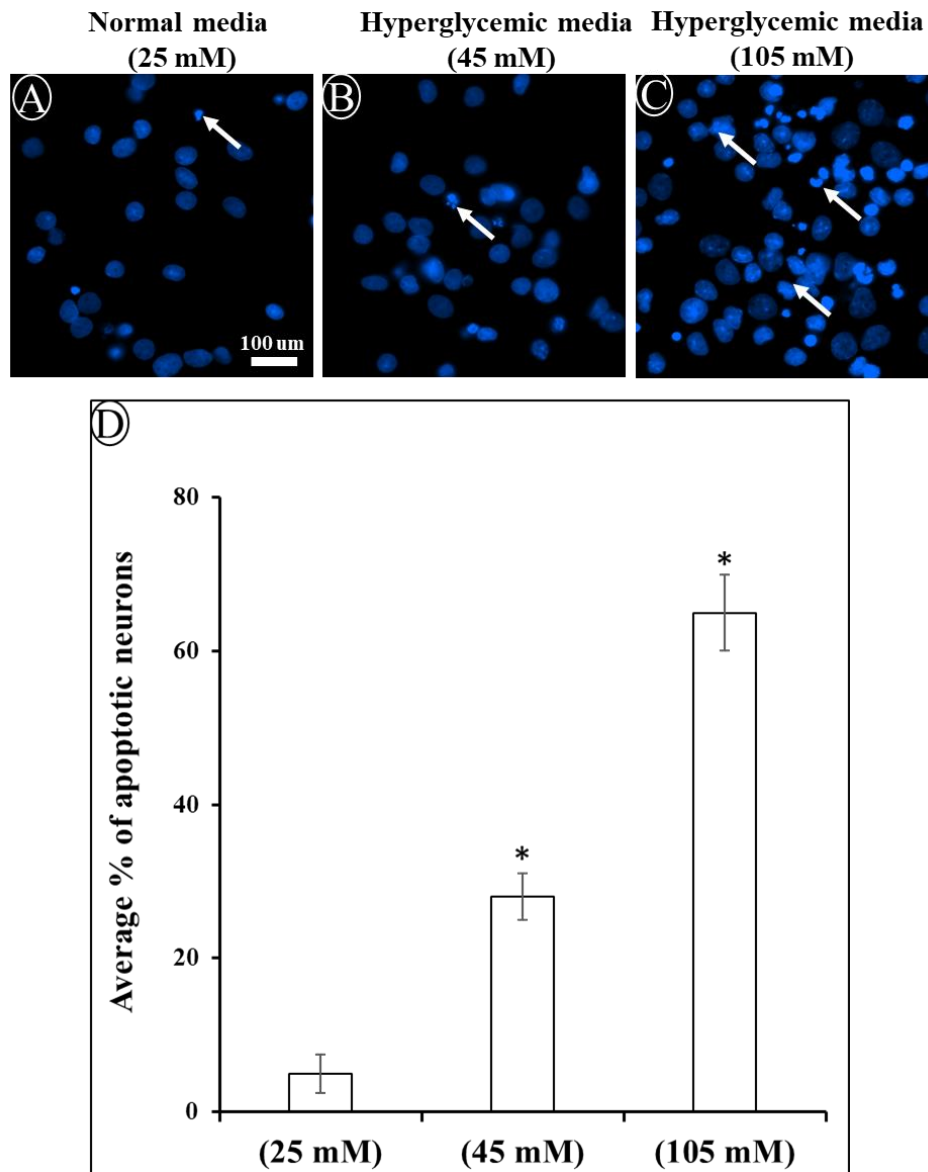
Figure 3. 15 - DAPI staining showing the rate of apoptosis caused by hyperglycemia. (A) Normal media (25 mM), (B) Hyperglycemic media (45 mM), and (C) Hyperglycemic media (105 mM) respectively. (D) Quantitative analysis of the average apoptotic cells at different experimental conditions. Arrows show the apoptotic nuclei. All groups were compared to the control p < 0.05, n = 3.

3.3.9 Effect of hyperglycemia on cortical neuron viability

To determine the effects of hyperglycemic conditions on cortical neurons viability, neurons were incubated in hyperglycemic media (HGM, 45 mM) for 24 h and then examined for viability using the LIVE/DEAD assay kit. The normal culture (control) did not affect the viability (Fig. 3.16A), but after exposure to HGM for one day, cell viability decreased (Fig. 3.16B). When P188, NAC, and P188 + NAC treatment was applied, the neuron cell viability appeared to have been restored (Fig. 3.16C - E).
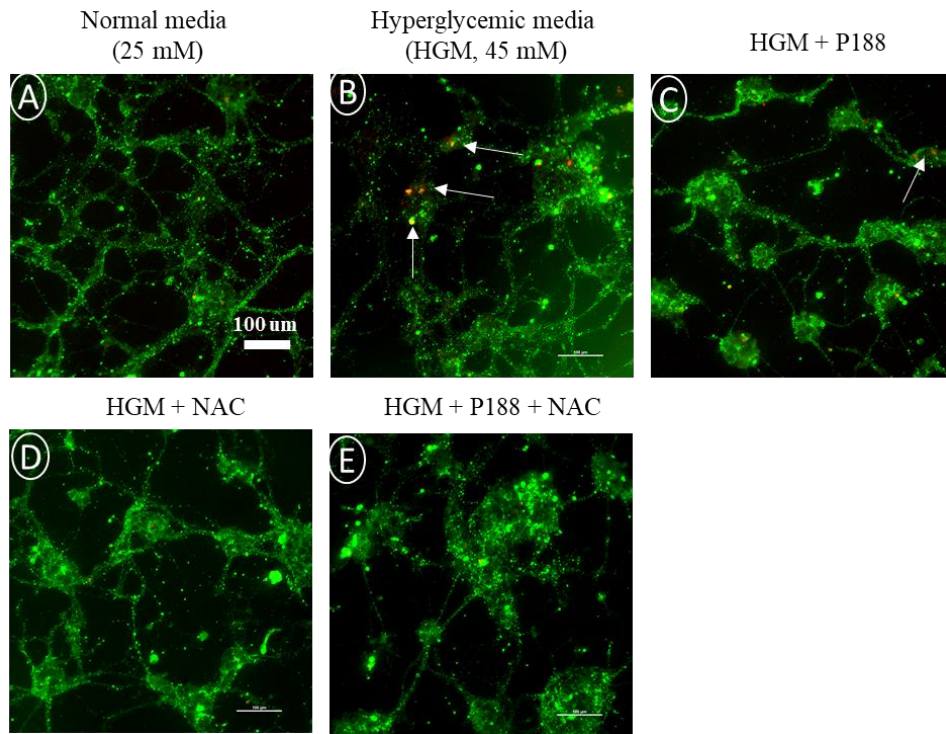
Figure 3. 16 - The viability of E18 rat embryonic cortical neurons at different experimental conditions using the LIVE/DEAD kit. Live (Green) and dead (Red) (A) control, (B) Neurons exposed to hyperglycemic conditions, (45 mM). (C) cells treated with P188, (D) cells treated with NAC, and (E) cells treated with P188 + NAC after exposure to hyperglycemic conditions (n = 3, Scale bar = 100 um).

3.3.10 Glucose alteration induced ROS expression in Cortical neurons

To determine the effects of hyperglycemic conditions on ROS activation in neurons, cortical neurons were exposed to hyperglycemic conditions, and mitoSox was used to determine the levels of ROS expression. After exposure of neuron cells to hyperglycemic conditions (45 mM) for 1-

day ROS level significantly increased (Fig. 3.17B). Treatment with P188 decreased the levels of ROS induced by hypo/hyperglycemic conditions (Fig. 3.14C). Treatment with NAC showed a significant reduction in the level of ROS produced (Fig. 3.17D). However, treating the cortical neurons with both P188 and NAC reduced ROS levels of expression (Fig. 3.17E) almost to the level of the control (Fig. 3.17A). Cortical neurons exposed to Hyperglycemic conditions showed a higher fluorescent intensity of ROS compared to the treatment groups and the control (Fig. 3.17).
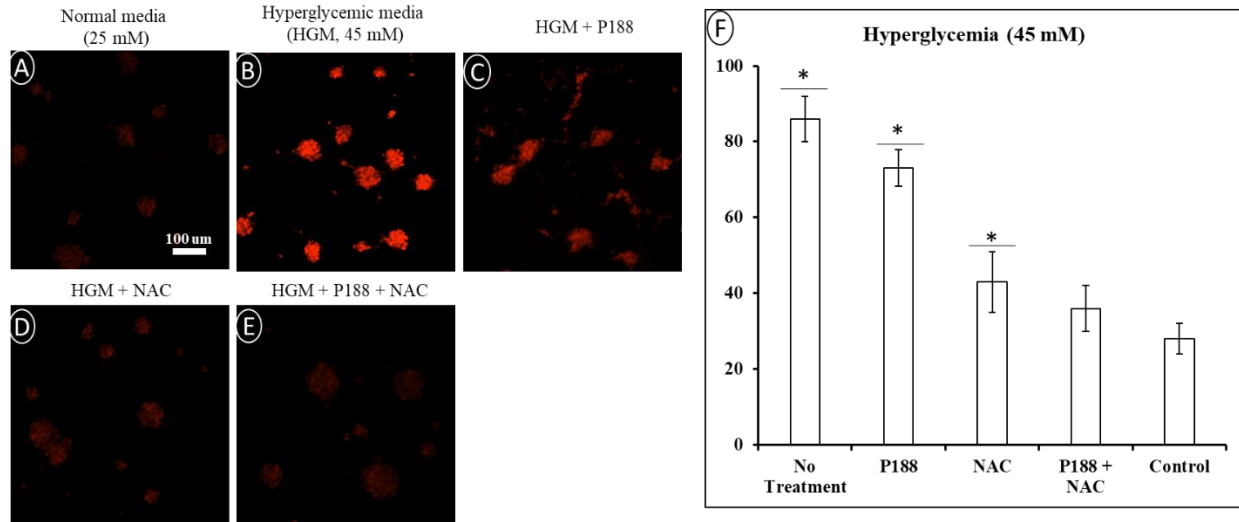
Figure 3. 17 - Intracellular superoxides in E18 rat embryonic cortical neurons one day after exposure to hyperglycemic conditions. (A) control, (B) Neurons exposed to hyperglycemic conditions, (45 mM). (C) cells treated with P188, (D) cells treated with NAC, and(E) cells treated with P188 + NAC after exposure to hyperglycemic conditions, (F) Quantitative analysis of the fluorescent intensity in neurons (n = 3, Scale bar = 100 um).

3.4   DISCUSSION

Glucose is the primary source of energy in the brain. GLUT1 is one of the main glucose transporters in the brain and is colocalized with ZO-1 so disrupting the transporter would likely disrupt the homeostasis of glucose metabolism. Defect in the GLUT1 function and BBB damage leads to high flow of glucose to the brain causing neurological damage/diseases such as neuropathy [110-112]. Hyperglycemic condition is frequently used as a standard model to study diabetic sensory neuropathy in vitro [113]. To confirm that neuron exposure to hyperglycemia is mediated by disrupted GLUT1 due to impairment of BBB barrier function, we measured the permeability

of MPBMEC monolayer to fluorescent glucose analog in cells exposed to microcavitation (5 blasts), (20 uM cocaine + 0.1% alcohol), or (1 uM cocaine + 0.1% alcohol). We observed a statistically significant increase in the permeability of the fluorescent glucose analog in cells exposed to 5 blasts - about 6-fold higher than the permeability of unexposed intact cells. A significant increase in the permeability was also observed in groups exposed to (20 uM cocaine + 0.1% alcohol) and (1 uM cocaine + 0.1% alcohol) (Fig. 3.4). Microcavitation is a plausible mechanism of cell detachment and disruption [118], and cocaine and alcohol has also been shown to have the capability of chemically altering the BBB integrity *in vitro* by affecting tight junction (TJ) protein expression [119]. In addition, our findings are also supported by previous studies on brain endothelial cells [120, 121]. Specifically, our results have shown that the relative loss of BECs integrity as demonstrated by changes in the glucose analog permeability is caused by the capability of cocaine and alcohol to differentially regulate the TJ protein distribution and expression in a concentration-dependent manner. However, upon treating the cells with P188 + NAC for 12 hrs, we observed a statistical decrease in the permeability of the fluorescent glucose analog compared to control cells (Fig. 3.4). The use of P188 as a membrane sealant is well documented [118], hence the potential to reduce permeability. NAC is an antioxidant which helps to quickly eradicate ROS and enhance faster regeneration of cells [122]. The combination of these two compounds suggests plausible potential to be used as therapeutics and is reported in this thesis for the first time for clinical efficacy.

Based on our permeability results, we concluded that hyperglycemia is likely an adverse effect when there is disruption of GLUT1 and leading to a higher permeability of glucose to the brain tissue. Several lines of evidence can be provided. We first validated the colocalization of GLUT1 and ZO-1 at the cell-cell membrane junction (Fig. 3.5A-C). We reported decreased GLUT1 and impairment in the BECs barrier functions of MPBMECs exposed to microcavitation, cocaine and alcohol. The levels of these impairments (ZO-1 degradation) correlated with disruption of GLUT1. Second, we showed that GLUT1 plays a critical role in the formation of the BBB tight junction and its organization (Fig. 3.5). Following exposure to different concentrations of cocaine (1, 2.5, 5, 10, and 20 uM), our data showed a progressive down-regulation of GLUT1 and ZO-1 expression at cell-cell contacts as the concentration increases (Appendix 2). Endothelial cells exposure to (20 uM cocaine + 0.1% alcohol) caused a rapid alteration of GLUT1 and ZO-1 and perforation (as shown by diffusion of GLUT1 into the nucleus) of the nucleus after just 5

minutes of incubation (Fig. 3.6). However, it took up to 25 minutes for significant reductions in both tight components to be observed in endothelial cells exposed to (1 uM cocaine + 0.1% alcohol) (Fig. 3.7), suggesting a concentration-dependent dysregulation of GLUT1 and ZO-1 at the cell-cell contacts.

To support our observation from the effects of cocaine and alcohol on the glucose transporters (GLUT1), we conducted a time-dependent study of glucose uptake and observed that the longer the incubation time, the longer the glucose uptake by MPBMECs (Fig. 3.8). The fluorescent intensity quantification showed a rapid uptake within 90 minutes (Fig. 3.8). On the other hand, we found that a low concentration of cocaine (1 µM) and in combination with 0.1% alcohol significantly decreased the glucose transporter protein-1 (GLUT1) expression and therefore decreased the rate of glucose uptake. Consequently, since a higher concentration of cocaine (20 µM) plus alcohol significantly suppressed the GLUT1 and ZO-1 protein expressions in BECs, it was concluded that it would likely decrease the rate of glucose uptake. Here, we have demonstrated that chronic use of cocaine and alcohol may interfere with glucose uptake and transport at the brain endothelium (Fig. 3.9). The fluorescent intensity quantification was much lower compared to the control (Fig. 3.9). Daily treatment with cocaine (1 and 20 µM), 0.1% alcohol, cocaine (20 µM) + 0.1% alcohol, and cocaine (1 µM) + 0.1% alcohol in primary MPBMECs culture for 3 days almost completely diminished the fluorescent glucose analog expressions (Fig. 3.10A-J). The fluorescent intensity quantification showed a very low intensity compared to the control (Fig. 3.10). The cocaine and alcohol exposure-induced overexpression of superoxide in BECs also correlated with the diminished levels of GLUT1 protein expression. The ROS expression increased 6 hrs after exposure and slightly decreased 12 h later (Fig. 3.11A-J). The fluorescent quantification showed statistical difference between 6 and 12 hrs. (Fig. 3.11K). Consequently, the cell viability reduced statistically after exposing the cells to cocaine and alcohol for 6 and 24 h (Fig. 3.12). This supports a postulate that excessive cocaine and alcohol exposure leads to the BECs barrier impairment. We also showed that cocaine and alcohol disrupt the glucose uptake by suppressing the GLUT1 expression followed by disruption of the BECs integrity, leading to an increased permeability of fluorescent glucose analog across the BECs. It would be of great benefit to understand the sequence or pattern of damage that can be caused by the combination of microcavitation + cocaine + alcohol on brain endothelial cells. The effect of mechanical plus chemical exposure will be elucidated in future studies. For now, we speculate that

the combination of mechanical (microcavitation) and chemical (cocaine + alcohol) disruption will cause additive or perhaps synergistically adverse damage to the tight junction complexes. Quantitative determination of such effects remains to be carried out.

Since glucose transporters are destroyed (Fig. 3.6 and 7), and the increased permeability across the BECs is attributed to the impairment of GLUT1 [109], we proceeded to determine the effect of hyperglycemia on neurons by exposing cortical neurons to hyperglycemic conditions (45 and 105 mM) (Fig. 3.13). Cortical neurons cultured in different hypoglycemic conditions (Fig. 3.13B - C) for 24 hrs displayed a loss of neural networks and shrinkage of neurospheroids. Interestingly, the administration of P188, NAC, and in combination restored, at least partially, the neurospheroid morphology and size and the neural network (Fig. 3.13D - I). The most significant effect was observed in the group treated with P188 + NAC (Fig. 3.13H-I). Neurospheroids are commonly used for *in vitro* disease modeling and drug screening. Neurospheroids act as anchoring points in the neural networks and enhances functionality. One notable aspect of this study is the display of thick bundles of dendrites extending outward from one neurospheroids to another, and our results are similar to previously reported studies [123-126]. In addition to the changes noted via fluorescent imaging, we also analyzed the images of the diameter, shape, and homogeneity of the neurospheroids. (Fig. 3.14). After one day of exposure to hyperglycemia, we observed a significant decrease in the diameter of neurospheroids and reduction in the neural network. With the P188+NAC treatment the neuronal cell morphology was restored back to normal in terms of neurospheroid diameter and enhanced the neural network (Fig. 3.13H and I). Diameter of neurons exposed to hyperglycemic conditions (45 mM) was restored to normal (Fig. 3.14A). However, the spheroid diameters of neurons exposed to an extreme and near lethal hyperglycemic condition (105 mM) were statistically smaller than the control even after the treatment with P188 + NAC for 24 hrs (Fig. 3.14B). While the combination of P188 + NAC may have limited restorative effects, we postulate that a longer treatment may demonstrate a marked restoration. Nevertheless, our data point to the potential use of P188 + NAC for neuron restoration and repaired functionality. In this study, we pointed out earlier that hyperglycemia causes a rapid increase of intracellular ROS, which reduces cell viability and leads to apoptosis. We therefore tested the hypothesis by exposing cortical neurons to hyperglycemic conditions (45 and 105 mM) for 24 hrs. Cortical neurons showed a condensed nuclear morphology, fragmented DNA and correlated with apoptosis (Fig. 3.15A - C). The quantification of non-viable cells shows that the higher the glucose concentration,

the higher the number of dead cells (Fig. 3.15). While it is not surprising, it accentuates the extent of detrimental effect that hyperglycemia has on neurons.

Furthermore, the effect of hyperglycemia on cortical neurons was further determined by neuronal cell viability (Fig. 3.16). As suspected, the viability reduced after exposure to hyperglycemia. The application of P188, NAC, and P188 + NAC increased the neuronal cell viability back to normal (Fig. 3.16C - E) as compared to the control (Fig. 3.16A). Hyperglycemia is associated with an increased ROS production and eventual apoptosis of neurons [114]. The overexpressed ROS is harmful to neuron and can cause loss of nerve fibers, axonal atrophy, and demyelination [115]. Excessive ROS accumulation can activate caspase-9/3 causing cell apoptosis [116]. Hyperglycemia induces oxidative stress of neurons in central nervous tissue in the diabetic encephalopathy [117]. In this study, we observed a high expression of ROS in groups exposed to hyperglycemic conditions (45 mM) (Fig. 3.17). Subsequently, the administration of P188, NAC, and P188 + NAC inhibited the generation of intracellular ROS caused by hyperglycemia (Fig. 3.17C-E). While the antioxidant NAC statistically reduced the ROS expression (Fig. 3.17D), the combination of P188 + NAC suppressed the expression of ROS (Fig. 17E) close to that of the control cells (Fig. 3.17A). This further provides evidence that hyperglycemia-induced oxidative injury is ROS-dependent that activates the Caspase-3 signaling pathway, leading to neuronal apoptosis. The combination of P188 + NAC acts as a neuroprotector by reducing cell apoptosis induced by hyperglycemia. Taken collectively, the results from this study imply that hyperglycemia causes neuronal damage, and a combination of P188 + NAC may be administered to reverse such damage and facilitate the survival of the affected neurons. In this *in vitro* model of brain endothelial cell barrier integrity, we did not investigate whether a pre-treatment of P188 + NAC plays a critical role in potentially protecting the neurons. However, as shown in chapter 2, we found that P188 induced protection against matrix metalloproteinases 2 and 9 (MMP2 and 9) in mouse primary brain microvascular endothelial cells. Therefore, we may propose a postulate that cortical neurons are likely protected in a pre-treatment by the P188 + NAC cocktail.

3.5   CONCLUSION

In conclusion, disruption of the blood-brain barrier leads to the unrestricted flow of glucose from the blood to the brain, causing hyperglycemia. The combination of the P188 + NAC cocktail showed a significant therapeutic potential to rescue and restore the neurospheroids sizes. To the best of our knowledge, the effect of P188 + NAC has not yet been reported. However, the mechanism(s) of P188 + NAC is yet to be fully elucidated. Nonetheless, we presented a reliable and physiologically-relevant methodology to mimic the brain tissue and engineered a platform for rapid drug screening for potential treatment of brain traumas and neurodegenerative diseases.

Chapter 4

AIM 3: To encapsulate P188 and the combination of P188 + NAC in PLGA nanoparticles to investigate the potential therapeutic treatment. Decorate the nanoparticles with PSGL-1 to target and stimulate proliferation and repair of brain endothelial tight junctions.

4.1   INTRODUCTION

The blood-brain barrier (BBB) is a unique, selective barrier formed by the brain endothelial cells (BECs). They form complex, tight junctions by the interaction of several tight junction proteins including zonula occludens protein 1 (ZO-1 and ZO-2). ZO-1 is carefully characterized in our previous work. It is validated that ZO-1 protein anchors occludins and claudins to the actin cytoskeleton in the cell [127] and allows for paracellular transport to be modulated in response to different stimuli [128]. Another key protein is vascular endothelial cadherin (VE-cad). It is an adheren junction protein specific to endothelial cells [129]. Claudin-5 is also a commonly used marker of tight junction formation in monolayers of brain microvascular endothelial cells [130]. Among these tight junction proteins, we focused on ZO-1 because it has been implicated as an important scaffold protein and contains multiple domains that bind a diverse set of junction proteins [181].

In Chapter 2, we developed a model with the capability to study structural and physiological alterations in the brain endothelial cells' tight junctions by microcavitation (mechanical trauma). In Chapter 3, we used the model to study the effects of hyperglycemia on cortical neurons by investigating the effects of mechanical (microcavitation) and chemical (psychostimulant drugs (PSDs), e.g., cocaine and alcohol) damage on glucose transporters (GLUT1). But the question remains; why are some brain injuries not properly diagnosed by the sophisticated imaging modalities and detection techniques that are currently available? To answer this question, we formulated the following postulates; when the brain endothelial cells (BECs) are injured or inflamed, it is possible that the brain lesions are below the resolution limit of various imaging modalities. Furthermore, amplification of pathophysiological responses may be accumulated over time but is initiated by specific interactions around or at the injury site. For example, microcavitation detaches cells in a small area that we referred to as a crater (see Fig. 4.11). The size of crater is likely below the MRI resolution, for example [182], and the cells at the periphery of the crater are activated and perhaps become apoptotic over time. This naturally leads

to another set of questions in which whether we can develop engineering techniques to identify and target the injured cells and then perhaps deliver reparative drugs and compounds to rescue them. Under this postulate, we can specifically target (diagnostic) and repair (therapeutic) the injured cells. In Chapter 4 is focused on the question of, "Can we target the injured cells for therapeutic purposes?"

The body naturally responds to inflammation due to stimuli from foreign materials. However, prolonged inflammation can lead to vascular rupture [131]. Vascular inflammation is typically induced by activation of endothelial cells in response to either biochemical or mechanical induction (Fig. 4.1). Under the inflammatory, stress or activated conditions, the endothelial cells express a high level of the selectins including the E and P – selectins. The expression of the selectins recruits other adhesion molecules such as P-selectin glycoprotein ligand-1 (PSGL-1) to the vascular walls [132-134]. Therefore, upregulation of E-selectin makes the endothelium a great target for diagnosis of injury and potential delivery for repairing [135]. The development of specific targeting particles that can serve a dual role as a diagnosing and drug-delivering agent is of great interest and in urgent need [136].
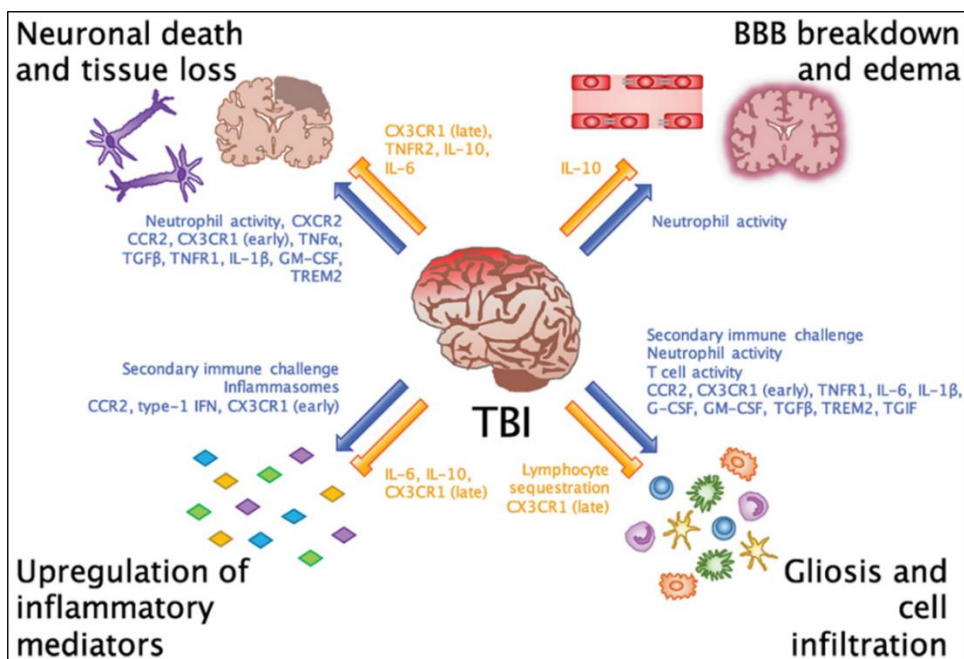
Figure 4. 1 - Schematics of the effects of the immune system in TBI: BBB breakdown and edema, upregulation of inflammatory mediators, and cell infiltration. Mckee et al. [171].

Nanoparticles (NPs) which can function as both therapeutic and diagnostic agents (i.e., theragnostic) [137] may be used as great tools for delivering therapeutic drugs to the target areas, hence reducing systemic administration of drugs and toxicity. However, most NPs are considered as foreign and are removed from circulation, thereby reducing the number of NPs that can reach its target [138]. Also, the brain endothelium has a unique feature which acts as a significant barrier to particles larger than 500 Dalton, unless specific conditions are present (e.g., activated endothelium) [139-141]. Only compromised endothelium allows particles and foreign substances to pass through. Targeted drug delivery focuses on the dosage, form, and route of administration [168], with the aim of modifying drug release profile, absorption, distribution, and elimination, hence improving product efficacy and safety, as well as patient convenience and compliance. The release of drug is often from diffusion, degradation, swelling, and affinity-based mechanisms [169]. Wide spectrum application of nanotechnology in pharmaceutical formulations is changing the scientific landscape of prevention, diagnosis, and treatment of diseases. Various pharmaceutical nanotechnology-based systems like liposomes, carbon nanotubes, quantum dots, dendrimers, polymeric nanoparticles, metallic nanoparticles, etc. have brought about revolutionary

changes in drug delivery as well as the total medical service system (Fig. 4.2). Nano-sized objects can be transformed in numerous ways to alter their characteristics (Fig. 4.3). Drug molecules in the nanometer range provide some unique features which can lead to prolonged circulation, improved drug localization, enhanced drug efficacy [168].
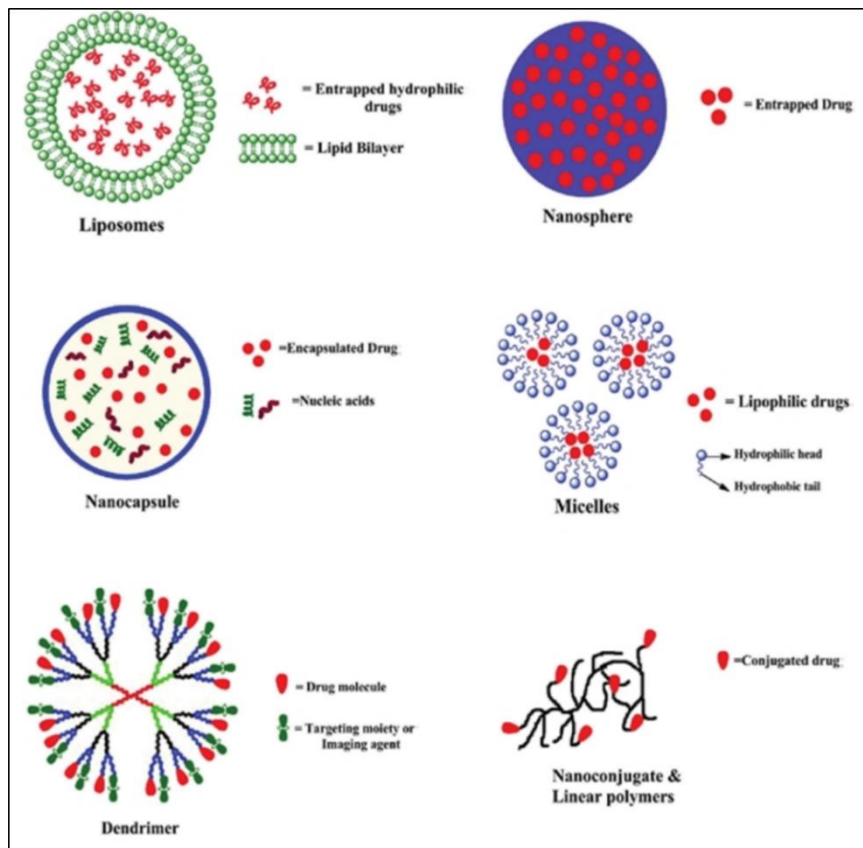
Figure 4. 2 - Schematics of different types of sustained-release formulations (Nanopharmaceuticals) Saad et al., [168].

The hydrophilic cover provides biocompatibility of the particles

Hydrophobic core contains drugs and released them controllably

Functional groups on the surface which provide the designed delivery

50 - 100 nm

The small size which provides good penetration into tissues
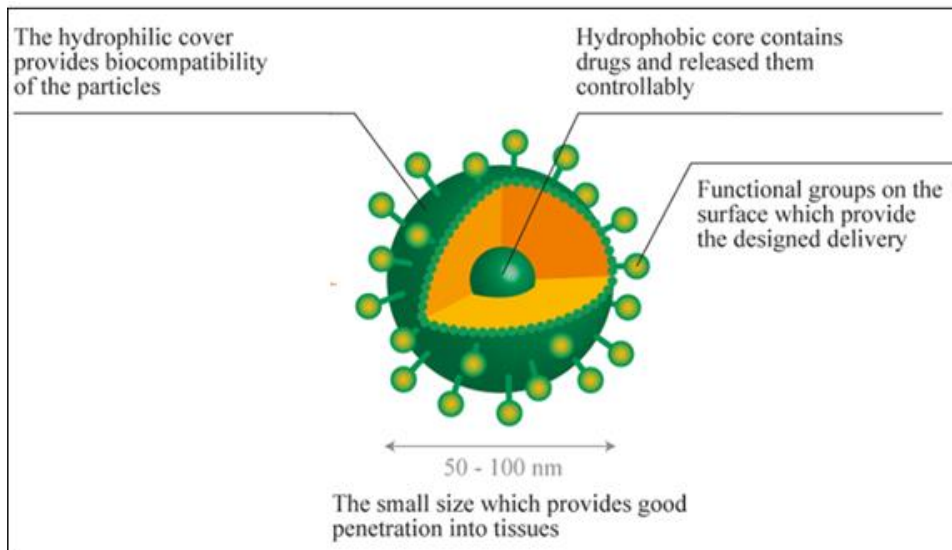
Figure 4. 3 - Schematics of a functionalized nanoparticle. Saad et al., [168].

Active targeting by modification of the NP surface with peptides or antibodies has improved cell-specific targeting [135]. However, studies utilizing antibodies that are only specific to a receptor showed only a slight increase in targeting efficiency *in vivo [142]*. The slight increase in targeting efficiency could be due to low binding of receptor-ligand efficiency. Therefore, a novel approach where a ligand can bind to receptors with high efficiency is necessary to address the issue of targeting efficiency. In this study, we will demonstrate that protein conjugated poly (lactic-co-glycolic acid; PLGA) NPs could be used to target the activated brain endothelium (Fig. 4.4). Once specific target is achieved; the potent drugs in the NPs can then be introduced to injury site to induce cellular repair and regeneration. This theragnostic approach was investigated by encapsulating P188 in PLGA NPs via a double emulsion method. The nanoparticles were functionalized with peptides against the activated endothelium-specific receptor, CD62e, which is overexpressed at sites of ECs injury. PLGA is an FDA-approved biodegradable polymer that is physically strong and highly biocompatible and has been extensively studied as delivery vehicles for DNA, drugs, proteins, and peptides [143]. Also, the physical properties of the polymer can be tuned by controlling some important parameters (molecular weight of the polymer, the ratio of lactide to glycolic acid). Depending upon the drug type, its concentration can be manipulated to achieve the desired dosage and release interval [144,145]. Poloxamer 188 (P188) + N-acetylcysteine (NAC) were encapsulated together into PLGA nanoparticles (NPs) to form P188 +

NAC PLGA NPs (from here on, we will refer to it as *"P188 + NAC NPs"*) and then conjugate with PSGL-1 to form PSGL-1 conjugated P188 + NAC PLGA NPs (from here on, we will refer to it as *"conjugated P188 + NAC NPs"*). P188 is an FDA approved biocompatible polymer with a lot of biomedical applications [175 – 178] (see full details in chapter 1 and 2). NAC is approved by FDA and is associated with so many health benefits [179 - 180] (details in previous chapters). The administration of conjugated P188 + NAC NPs to injured or activated BECs diminished ROS, increased cell viability, enhanced cell proliferation, statically increased the BECs integrity after chemically-induced injury and restored tight junction complex (GLUT1 and ZO-1). It appears evident that our conjugated P188 + NAC NPs can target, diagnose, deliver therapeutic drugs, and enhance cell proliferation. From this approach, effective diagnosis and therapy can be tailored by conjugating nanoparticles to a selectin ligand to target and deliver drugs to the injured cells. The idea is to establish targeted therapy and image the impacted blood-brain endothelium after blunt force trauma using the delivery of PSGL-1 conjugated nanoparticles.
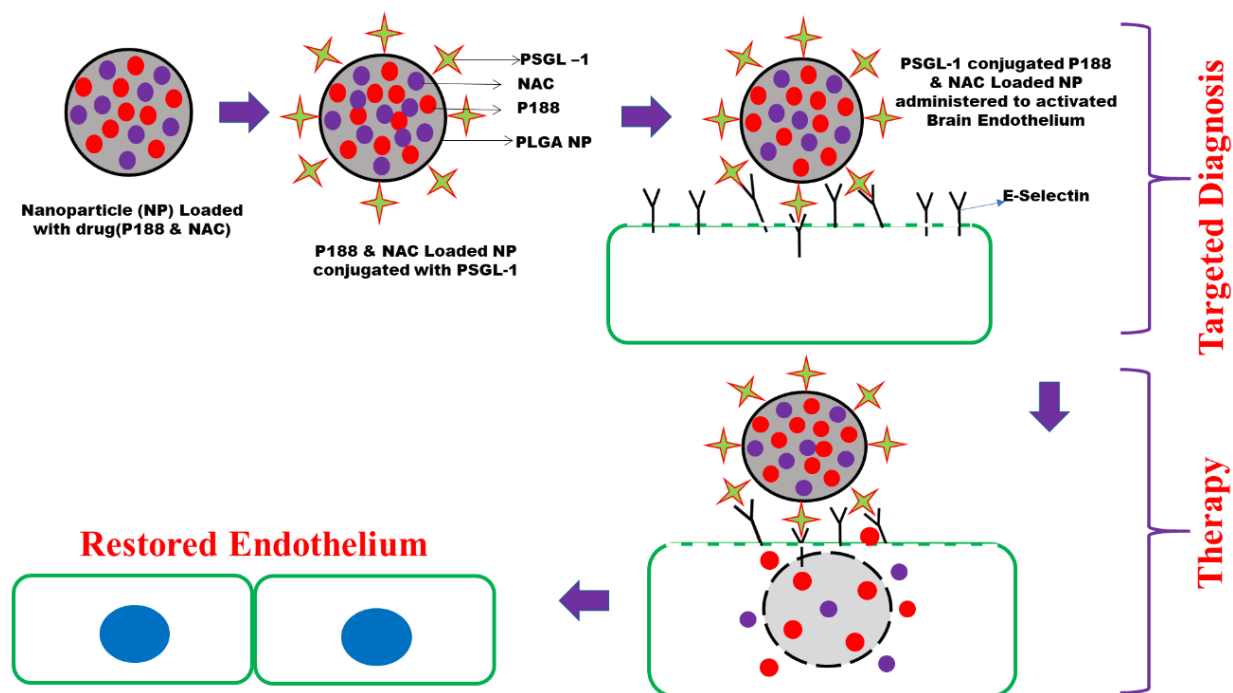
Figure 4. 4 - Schematics of our theragnostic approach: Injured endothelium with upregulated expression of E-selectin is targeted for proliferation. Fluorescent Dye is used for detection.

4.2 MATERIALS AND METHOD

4.2.1 Preparation and Characterization of P188, NAC, and P188-NAC loaded PLGA NPs

The double emulsion method was used to prepare P188, NAC, and P188 + NAC PLGA NPs. Briefly, the drug solution (water phase-w1) was formed by adding 0.2 mg of TAMRA conjugated P188 or 12 mg of NAC to 200 ul of DI water in a 0.5 ml centrifuge tube. Oil phase(o) was formed by adding 2 ml chloroform to the 50 mg PLGA and 10 ml 5% PVA solution was pipetted into a glass tube to form the second water phase(w2). P188 solution (W1) was added to the PLGA solution (O) and vortexed on high speed for 30 seconds to make a water-oil emulsion (W1/O) and then added to 5 % PVA solution dropwise using an aspirator pipet to get the water-oil-water emulsion (W1/O/W2). It was then vortexed at high speed for 2 minutes for emulsification before transferring to a 15ml beaker and stirred overnight, allowing chloroform to evaporate. The next day the above solution was collected into a 15ml centrifuge tube and centrifuged at 15000 rpm for 30 minutes. The supernatant was collected into another 15ml tube, and the obtained pellet was

washed, freeze-dried, and analyzed as described above. To prepared P188 + NAC PLGA NPs the same amount of PLGA and NAC as described above, was used with 10 ul of P188 solution following the protocol detailed above.

4.2.2   NPs size, Zeta Potential, and Morphology analysis.

One mg of each prepared NPs was suspended in DI water, mixed, and measured. The mean size, size distribution, and zeta potential of prepared NPs were measured by dynamic light scattering. The data were the averages of three measurements. The morphology of the NPs was examined by Scanning electron microscope (SEM). Briefly, particles were dropped onto a carbon-coated-on lacey support film and allowed to dry before characterization.

4.2.3   Drug Encapsulation Efficiency

The loading efficiency of all prepared NPs were determined. Briefly, 1 mg NPs were dissolved in 1 ml of dichloromethane (DCM) and sonicated. After evaporation of DCM for about 15 min, the solution left was used for fluorescence reading via high-performance liquid chromatography (HPLC). The results were converted into concentrations, and the loading efficiency for P188, NAC, and P188-NAC were 84.8, 77.6, and 28.3 respectively, and calculated using the following equation.

$$\text{Loading Efficiency} = \frac{\text{Original drug amount loaded} - \text{amount in nanoparticles}}{\text{Original amount}} * 100$$

4.2.4   In vitro drug release

For the release studies, 1 mg each from all prepared NPs were dispersed in 1 ml of release medium (pH 7.4) each to form a suspension. Each suspension was in three replicates in 1.5 ml centrifuge tubes and incubated at 37 °C. The release buffers were collected after centrifugation at 15,000 rpm for 30 min. The release buffers were replaced with fresh buffer at different periods and subjected to analysis using HPLC. The cumulative release of the model drug from each loaded NPs were plotted against time.

4.2.5 Cell Culture technique and characterization.

BALB/c Mouse Primary Brain Microvascular Endothelial Cells (MPBMECs) P3, from cell biologics, was grown in Endothelial Basal Medium-2(EBM-2) with EGM-2 kit (Lonza) in a flask coated with a gelatin-Based coating solution. For the experiment, MPBMECs (6.6×10^4 cells/cm^2) was directly seeded unto the cover glass coated with fibronectin (1μl/mL) and cultured with Endothelial Basal Medium from Lonza. Confluent cells were characterized by the tight junction and cytoskeletal proteins.

4.2.6 Brain endothelial cell Viability

Viability of cells following a 24-hour exposure to blank PLGA NPs (blank NPs), purified P188 (p-P188), NAC and P188 + NAC NPs was assessed with the MTT assay. It measures the metabolic conversion of the MTT salt (3-[4,5-dimethylthiazol-2- yl]-2,5-diphenyltetrazolinum bromide) by active mitochondrial dehydrogenases. Briefly, after exposure of BECs to blank NPs, p-P188, NAC and P188 + NAC NPs cells were treated with MTT (5 mg/ml) for 1 hour at 37°C. The formazan product generated was solubilized by the addition of 20% sodium dodecyl sulfate and 50% N, N-dimethylformamide, and quantified by measuring its absorbance at 490 nm. Untreated cells were taken as control with 100% viability. Resulting sample absorbance was used to calculate cell viability.

4.2.7 Endothelial Cells Activation

Confluent cells were exposed to TNF-α (10ng/ml) and incubated for 4 hrs. and then stained for selectins expression. Images were acquired to investigate E & P-Selectin expression after 1, 3, 6, and 24 h. This period was chosen based on our previous immunofluorescence observations that the earliest expression of inflammatory proteins on activated endothelial cells occurs between 1 to 6 hr, and the sustained expression of the selectins after 24 hr was of interest to complete this study.

4.2.8 Immunostaining for E & P-Selectin, and PSGL-1

Inflammatory markers in the brain endothelial cells were visualized using E & P-Selectin antibodies. Briefly, cells were activated by mechanical (microcavitation) and chemical (TNF-α) induction, fixed with 4% paraformaldehyde in PBS, permeabilized with 0.1% Triton X-100 for 3 minutes and blocked with 3% of BSA for 1 hour. Cells were incubated with the E and P-selectin

primary antibodies (1:500, 4.3 µg/ml, Santa Cruz., SC137054, and SC271267 respectively), and subsequently incubated with Alexa Fluor 488-conjugated goat anti-mouse IgG (1:1000, 2 µg/ml, Santa Cruz., SC516167). Nuclei counter-stained with DAPI.

4.2.9   Measurement of Mitochondrial Reactive oxygen species (ROS)

In this study, ROS was measured using a MitoSOX™ Red mitochondrial superoxide indicator, according to the manufacturer's instructions. Briefly, BECs were cultured on glass cover slides and exposed to TNF-α and Histamine for 4 h before treating with P188, NAC, and P188 + NAC. After treatments, the cells were incubated with 1 µM MitoSOX™ reagent working solution for 30 min under room temperature in the dark. After washing three times with PBS, the fluorescence was imaged with a fluorescent microscope.

4.2.10 Conjugation of PSGL to PLGA NPs

The functional ligand PSGL was bound to the surface of the PLGA NPs via the EDC-NHS chemistry as described elsewhere with modification [146]. Briefly, 120 mg of EDC added to 180 mg NHS and dissolved in 5 ml of MES buffer (0.1 M, pH 4.75). 20mg PLGA NPs were resuspended in the EDC-NHS solution and rotated for 2h at room temperature. After 2 h of incubation at room temperature with rotation, the resulting NPs were ultracentrifuge at 15,000 rpm for 30 min, (4º) washed three times with PBS, and then resuspended in PBS (1mg/ml). 80ul of 500 ug/ml of mouse PSGL antibody (Sino Biological, 50770-MCCH) was added to the NPs solution and incubated for 24h at (4º). Following the incubation, the NPs were collected by ultracentrifugation at 15,000 rpm for 30 min. The supernatant was used to determine peptide conjugation efficiency. Pallets were resuspended in DI water, freeze-dried, and stored for use.

4.2.11 Cellular Uptake of conjugated FITC labeled PLGA NPs

MPBMECs (2×10^4 cells per well) were cultured in a 96 well plate in Dulbecco's Modified Eagle's Medium (DMEM) supplemented with 2% fetal bovine serum (FBS) and 1% of penicillin at 37 °C for 24h. FITC-loaded NPs (1mg/ml) was used for the observation of cellular uptake at 37 °C for 4 h. Conjugated FITC NPs were added to two columns of the 96 well plate (one column activated with TNF-α and one column inactivated), and unconjugated FITC NPs were also added to activated and inactivated ECs. After uptake, the wells were washed three times with PBS and

then lysed by incubating with triton 1X for 1h. An aliquot from each well was collected and analyzed for fluorescence intensity and protein absorption with a microplate reader with excitation and emission wavelength at 430 nm and 485 nm, respectively.

4.2.12 In vitro injury Model and Comparative Assessment of P188, growth factors, and NAC

Primary mouse endothelial cells were seeded in 24-well plates (10×10^3 cells/well) and grown until confluence in complete endothelial cell media. Then a straight scratch was made with a P200 pipette tip, to simulate a wound. The cell debris was removed by washing with PBS. Wound size images were taken at time 0 h. The wounds were exposed to different single treatments; P188 (500 uM,), EPO (5 U/ml), VEGF (50 ng/ml), and NAC (0.82 mg/ml) and in combination (P188 + EPO, P188 + VEGF, and P188 + NAC) at the recommended therapeutic concentration in DMEM with 1% serum for 12 h. The cells without drug were used as the negative control and cells treated with 10% FBS was used as a positive control. The closure of a wound scratch was observed under a microscope (5× magnification) at 12 h after wounding. To quantify the closure of the wound scratch, difference between the wound width at time 0 and 12 h was determined. The scratch area was measured using ImageJ software (National Institutes of Health, Bethesda, MD, USA). Migration rate was expressed as a percentage of the wound scratch closure normalized by the initial wound area using the equation below. The mean values shown are from three independent experiments.

$$\text{Scratch closure rate} = \frac{\text{scratch area at time(h) 0} - \text{scratch area at time(h) 12}}{\text{scratch area at time 0}} * 100$$

After validating the injury model and determining the drug with high proliferation efficiency, cells were pre-incubated with green cell tracker for 30 minutes before exposing it to blast (microcavitation). The cells were properly washed with hanks buffer to remove debris and returned to the incubator in different experimental media conditions for investigation of the wound closure in response to microcavitation. Injury area closure was calculated, as mentioned above.

4.2.13 Measurement of Endothelial cell permeability

The custom-designed diffusion chamber and method used here to determine the permeability of 10 kDa tracer have been described in detail in Chapter 2.

4.2.14 Effects of conjugated P188 + NAC NPs on BECs tight junction complex

For GLUT-1 and ZO-1 expressions, BECs were cultured on glass coverslips until 80-100% confluent and then exposed to TNF-α (10ng/ml) for 4 hours. Fixed in 4% paraformaldehyde, permeabilized in (0.3% Triton X-100 for 3 minutes, blocked with 3% bovine serum albumin at room temperature for 1 hr and incubated with Alexa Fluor 555 and 488 conjugated GLUT-1 and ZO-1 antibody respectively. After that, cells were rinsed and counterstained with DAPI. Rinsed, mounted, imaged, and analyzed.

4.2.15 Statistical analysis

All data analysis was executed using one-way and two-way ANOVA (R-Studio Software) to analyze differences between group(s) with one or more independent variables. $p < 0.05$ was considered a significant difference. *Post hoc* analysis was done using Tukey's honest significant difference (HSD). All data were reported as mean ± standard deviation.

4.3 RESULTS

4.3.1 Characterization of all fabricated NPs

To prepare the NPs for this study PLGA-50-50 (24,000 – 30,000 MW) was used for fabrication. NPs were prepared, and TEM images indicated that all NPs maintained uniform size (Fig. 4.5.) and the zeta potential (Table 4). The NPs hydrodynamic particle sizes are, 153 +/- 12, 194 +/- 3, 141 +/- 1.4, and 212 +/- 12 nm for blank, P188, NAC, and P188 + NAC loaded NPs respectively. The blank nanoparticles had significantly higher sizes than the NAC loaded NPs, but the P188 and P188 + NAC NPs were significantly larger than the blanks. The loading efficiency for P188 and NAC was determined to be 84.8% and 28.3% via a direct method (this done by dissolving the NPs to use its contents for estimation of loading efficiency). The zeta potential for P188, NAC, and P188 + NAC NPs was -32 +/- 1.01, -28 +/- 0.66, -29.15 +/- 0.41, and -26.59 +/- 2.51 mV. (Zeta potential is a measure of the magnitude of the electrostatic or charge repulsion/attraction between particles and **is** one of the fundamental parameters known to affect stability. The low loading efficiency of NAC, when compared to P188, is attributed to factors such as the molecular weight

of the compound, rapid diffusion of the drug from the nanoparticles, human error, and systemic error. Any of these errors or in combination, can reduce the fluorescence intensity. However, the combination of P188 and NAC can increase the loading efficiency.

TEM Images of Nanoparticles
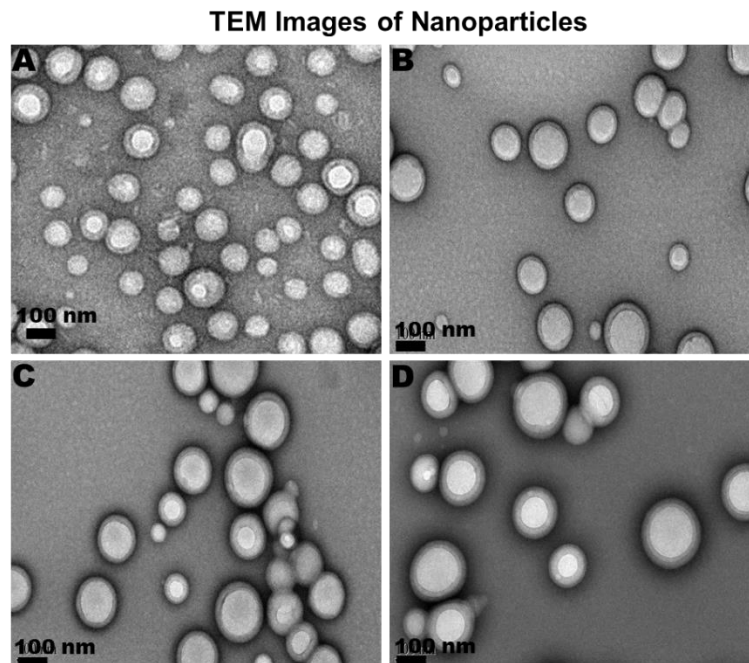
Figure 4. 5 - TEM images of PLGA nanoparticles. (A) blank PLGA NPs, (B) P188 loaded PLGA NPs, (C) NAC loaded NPs, and (D) P188 + NAC loaded PLGA NPs. Scale bar = 100.

Table 4 - NPs characterization: physical properties of synthesized PLGA NPs

Nanoparticle Batch	Size (nm)	Poly Dispersity	Zeta Potential (mV)
Blank PLGA NPs	153 +/- 12	0.052 +/- 0.01	-32 +/- 1.01
P188 loaded PLGA NPs	194 +/- 3	0.186 +/- 0.01	-28 +/- 0.66
NAC loaded PLGA NPs	141 +/- 1.4	0.126 +/- 0.04	-29.15 +/- 0.41
E-selectin targeted, P188/NAC loaded PLGA NPs	212 +/- 12	0.056 +/- 0.04	-26.59 +/- 2.51

The P188 release from the PLGA NPs was carried out throughout 4 weeks, while the NAC release was only for a week. The fluorescence intensity measurements from the release were converted into concentration using standard curve, and the drug released was converted to a percentage drug release, and percentage drug release was further converted to a percentage cumulative drug release. The percentage of cumulative drug release was plotted over time (four weeks) (Fig. 4.6). A burst release of P188 was observed after an hour with about 12% then a steady release for 28 days while NAC was at about 5%. Five percent release after an hour is a lot considering the fact that only 28.3% OF NAC was loaded into the NPs. The molecular weight of NAC could be a factor here. Hundred percent of NAC loaded was completely release after 7 days.
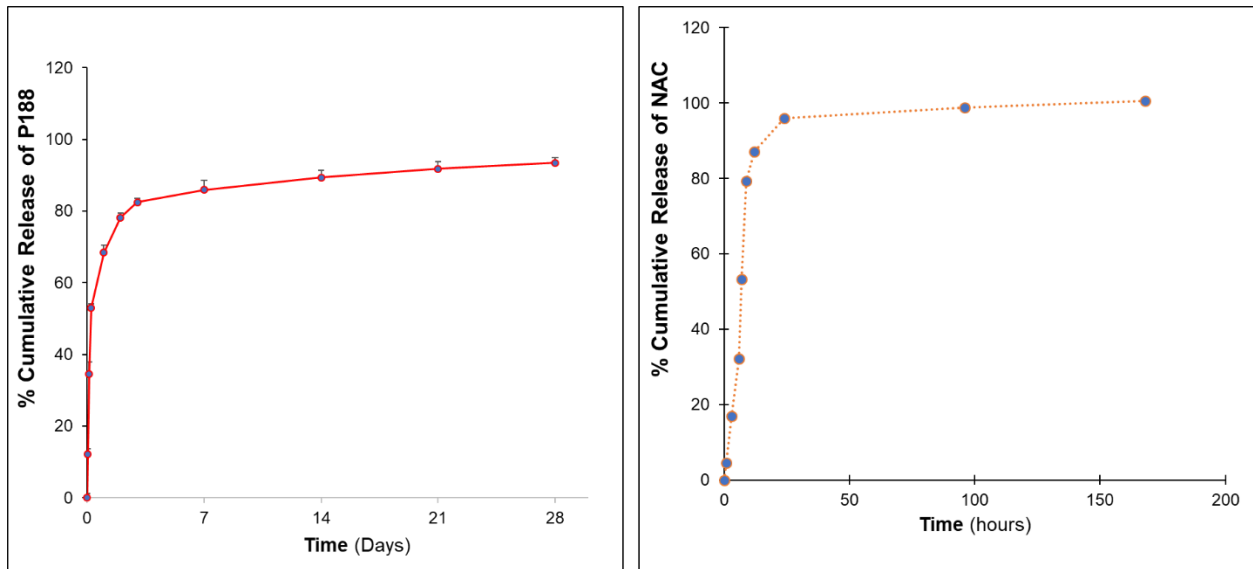
Figure 4. 6 - The P188 and NAC release profile of PLGA NPs

4.3.2 Characterization of Tight Junction Proteins

The MPBMECs used in this study were characterized by tight junction proteins and cytoskeletal structure expressions. The tightly packed monolayers expressed tight junction protein; ZO-1 and Occludin-5 at the confluence (Fig. 4.7A and B) as previously documented. Immunostaining confirms the expression of actin filaments (Fig. 4.7C).
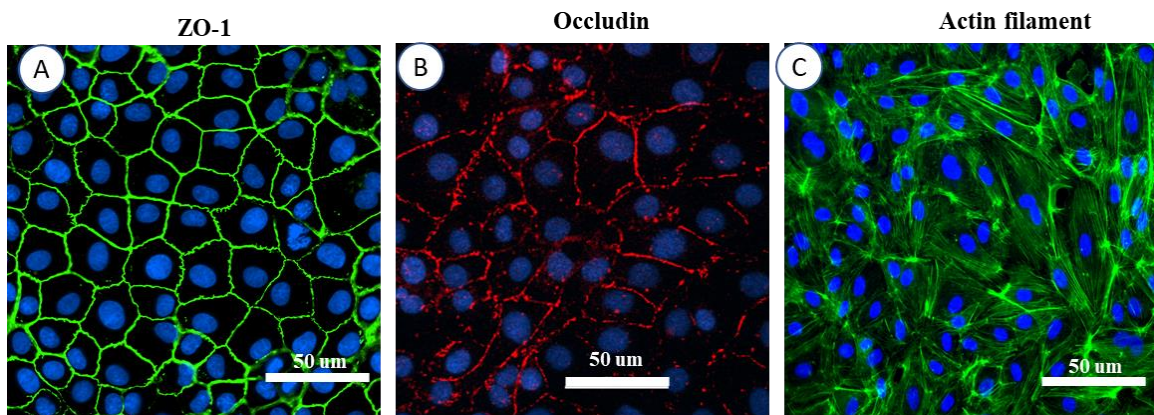
Figure 4. 7 - Characterization of the endothelial cell's tight junction features and cytoskeletal fibers. Tight junction protein (A) ZO-1 (B) Occludin. (C) shows a well-organized actin filament.

4.3.3. Cytotoxicity Testing

All fabricated NPs were tested for toxicity to the cells. Exposure of MPBMECs to blank PLGA NPs (b-PLGA), purified P188 (p-P188), NAC, and P188 + NAC NPs resulted in a dose-dependent inhibition of cell viability specifically for b-PLGA, p-P188 and P188 + NAC NPs as measured by the MTT assay (Fig. 4.8A, B and D). After 24 hours, the effect was evident for 1500 - 2000 µg b-PLGA (Fig. 4.8A), p-P188 at 750 µM dose also inhibited cell proliferation (Fig. 4.8B), and 2000 µg P188 + NAC NPs. In contrast, even the highest dose of NAC tested (20 mM) did not inhibit proliferation as compared to the control. These doses were used in further experiments.
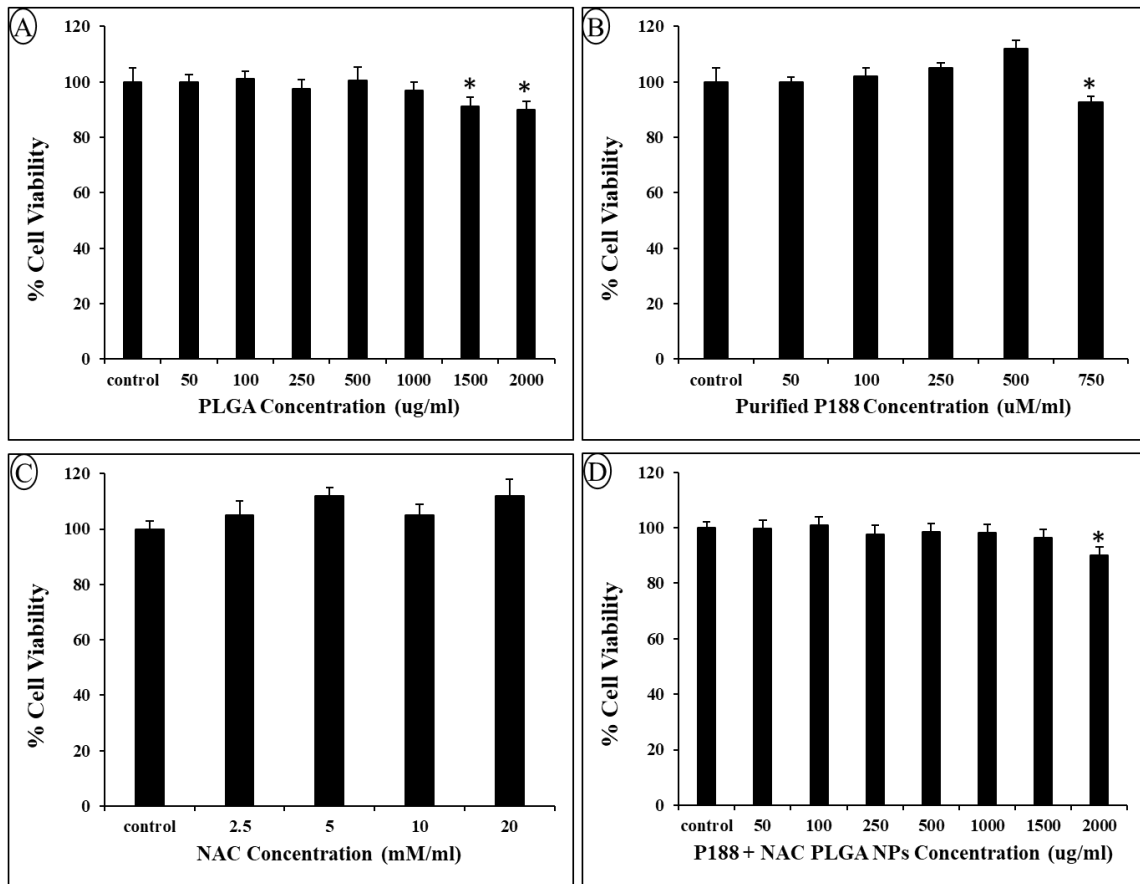
Figure 4. 8 - Effect of blank PLGA NPs (b-PLGA), purified P188 (p-P188), and NAC on endothelial cell viability. MPBMECs were treated with increasing doses of (A) b-PLGA, (B) p-P188, and (C) NAC for 24 h. After the exposure, cell viability was measured with the MTT test (n=3). Data expressed as a percentage of control at the same time point. Asterisks represent a significant difference compared to respective control. P < 0.05.

4.3.4 TNF-α Administration, E and P-Selectin Expression

To validate that E-selectin is a suitable candidate for targeting at inflammation, we incubated BECs with TNF-α to generate focal inflammatory lesions as a model for BBB disruption. As previously reported, the administration of TNF-α induced the up-regulation of E- and P-selectin. At 1 hr after administration, we observed high expression of P-selectin and few E-selectin (Fig. 4.9C and D). After 3 hr, we observed a very high expression of both E & P-Selectin (Fig. 4.9E and F). However, after 6 hr., the expression of P-selectin went down, but the expression of E-selectin was still elevated (Fig. 4.9G and I). The same was observed for 24 hr (Fig. 4.9J and K). All experimental groups were compared to the control (Fig. 4.9A and C). To confirm that the selectins upregulation is chemically induced we incubated the cells with TNF-α and histamine and we observed similar results compared to TNF-α alone (Fig. 4.10A and B). After performing an extensive set of control experiments, MPBMECs monolayers were exposed to microcavitation to determine the expression of E-selectin after blast exposure. Cells were returned into the incubator under no serum media condition for 1 to 3 hours to validate the expression of E-selectin as observed in the chemically (TNF-α and histamine) induced cells. As demonstrated before, the fluorescent expression of E-selectin was significantly upregulated after 3 h in comparison to the 1 h time point (Fig. 4.11).
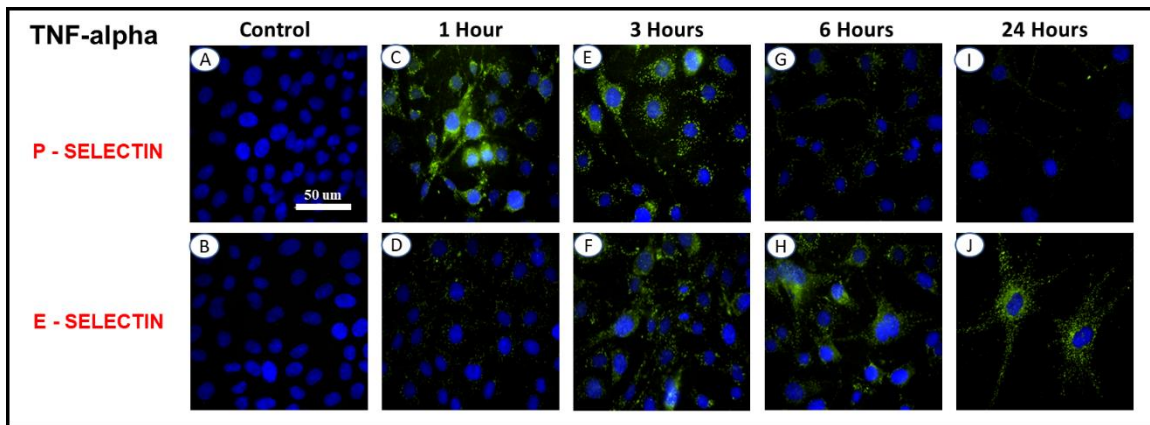
Figure 4. 9 - E and the P-selectin expression on whole cells with TNF-α stimulation. MPBMECs monolayers were incubated with TNF-α (10 ng/ml). Control (A & B). After 4 h stimulation, cells were incubated in fresh serum-free medium for 1 h (C & D), 3 h (E & F), 6 h (G & H), and 24 h (I & J) before immunofluorescence staining for the expression of E & P-selectins. Control cells were also examined (A & B).
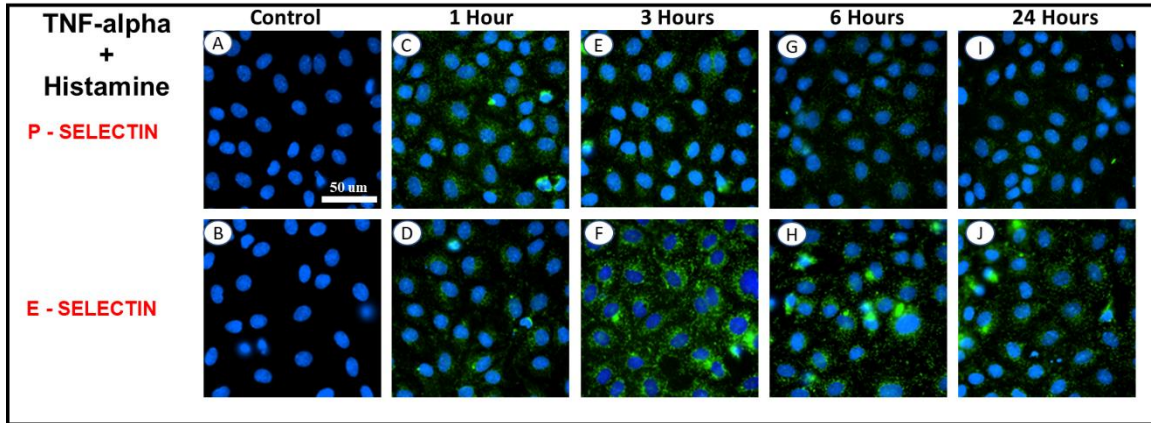
Figure 4. 10 - E and the P-selectin expression on whole cells with TNF-α + Histamine stimulation. MPBMECs monolayers were incubated with TNF-α (10 ng/ml). Control (A & B). After 4 h stimulation, cells were incubated in fresh serum-free medium for 1 h (C & D), 3 h (E& F), 6 H (G & H), and 24 h (I & J) before immunofluorescence staining for expression of E & P-selectin.
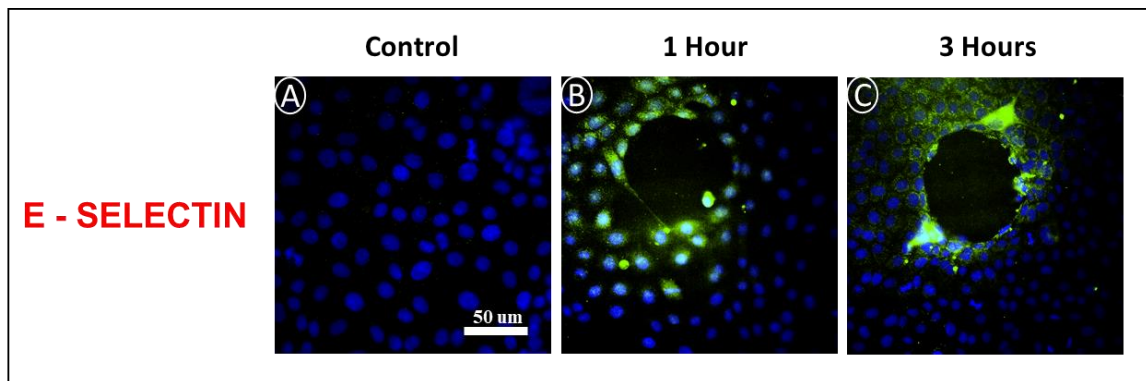
Figure 4. 11 - E-selectin expressions on MPBMECs exposed to microcavitation (5 blasts). Control (A), cells were incubated in fresh serum-free medium for 1 h (B) and 3 h (C) after blasts before immunofluorescence staining for the expression of E-selectin.

4.3.5 BECs TNF-α and Histamine exposure increases ROS generation

To confirm the induction of inflammation on endothelial cells by TNF-α and histamine. BECs were exposed to TNF-α and histamine and imaged for superoxide expression, and the fluorescent intensity was also measured using MitoSox that binds to superoxide. After 4 h of BECs incubation with TNF-α and histamine, there was an increase in the expression of superoxide generation (Fig. 4.12A-E). Interestingly, after treating the cells with P188, NAC, or P188 + NAC, the expression

of ROS was suppressed. Changes in the fluorescent intensity are depicted in Figure 4.12K. The combination of P188 and NAC significantly depleted ROS almost to the level of control.
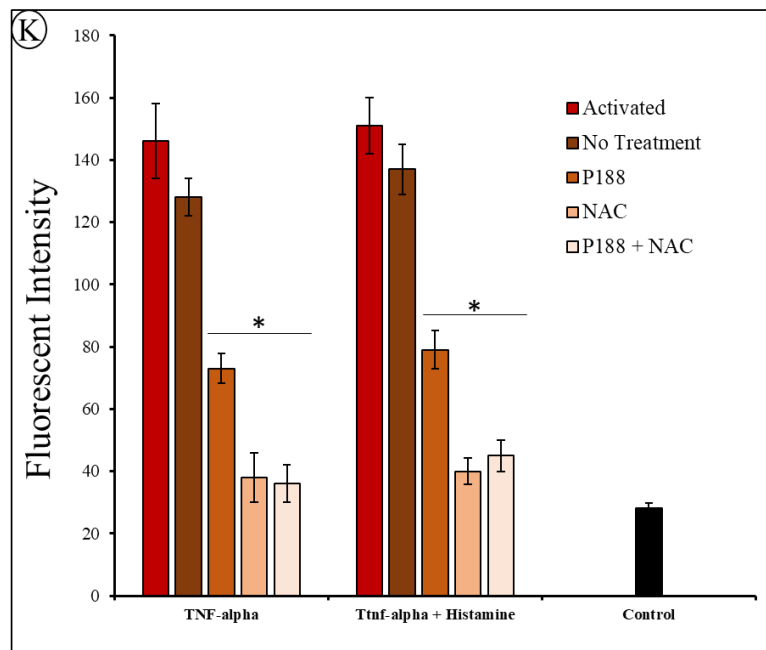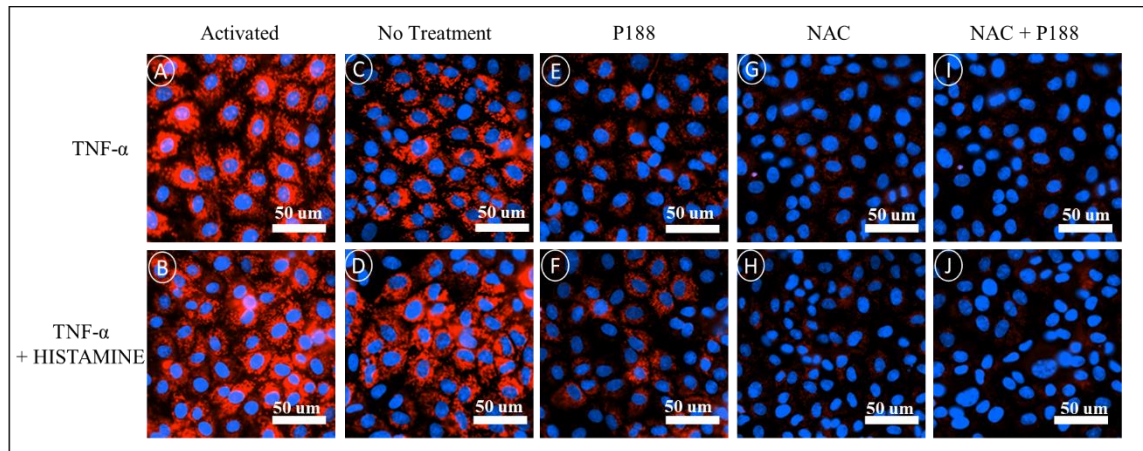
Figure 4. 12 - Injured brain endothelial cells (A and B) shows high levels of superoxide in response to TNF-α or combination with histamine. (C and D) If left untreated, the superoxide level persisted. (E thru H) P188 or NAC (antioxidant) treatment noticeably diminished the superoxide expression. (I & J) When treated simultaneously with NAC and P188, the superoxide level was essentially reduced to the baseline. Nuclei were stained with DAPI (blue). (K) Quantification of the fluorescent intensity of superoxide expressions, $p < 0.05$, n = 6.

4.3.6   Conjugation, binding, and cellular uptake

To validate conjugation and cellular uptake of conjugated NPs, BECs were incubated with conjugated NPs. The conjugation of PLGA NPs to PSGL protein used in this experiment resulted in 41.86 +/- 0.13% yield. The following formula was used [147]: $Conjugation\ Efficiency = \frac{(A-P)}{A} * 100$, where A is the initial amount of antibody, and P is the protein in supernatant. The binding and uptake of PSGL-1-PLGA NPs into TNF-α activated endothelium were determined in the mouse primary brain microvascular endothelial cells (MPBMECs). Following incubation, fluorescently labeled PSGL-1-PLGA NPs were internalized by MPBMECs with high affinity, whereas cells treated with non-targeted PLGA NPs had a minimal level of internalization (Fig. 4.13A-D) and (Fig. 4.13E). Quantification of protein concentration in those cell lysates showed that cells treated with PSGL-1-PLGA NPs had five times higher level of protein than that of the PLGA NPs incubated cells, indicating more efficient binding and uptake of MPBMECs targeted NPs (Fig. 4.13E). The time-dependent study was carried out to determine the duration of time needed for most NPs to be internalized. Fluorescent images show that the longer the wait time, the longer the degree of internalization (Fig. 4.14A-D). This was supported by the protein concentration analysis (Fig. 4.14E).
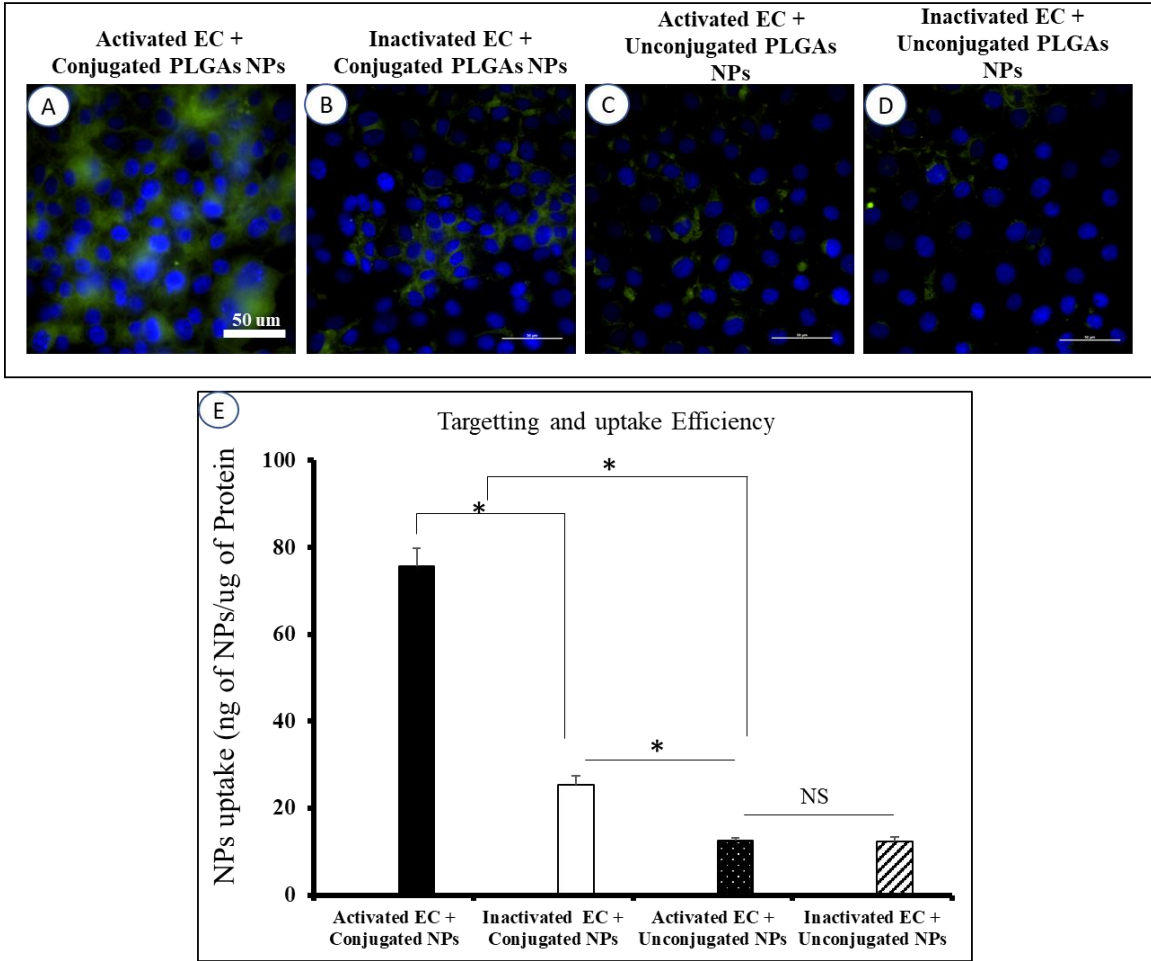
Figure 4. 13 - In vitro imaging of internalization of PSGL-1 conjugated FITC-PLGA nanoparticles (green). (A) Activated EC + Conjugated PLGA NPs, (B) Inactivated EC + Conjugated PLGA NPs, (C) Activated EC + Unconjugated PLGA NPs, and (D) Inactivated EC + Unconjugated PLGA NPs. (E) Histogram showing ng of NPs internalized per ug of protein, p < 0.05, n = 6.
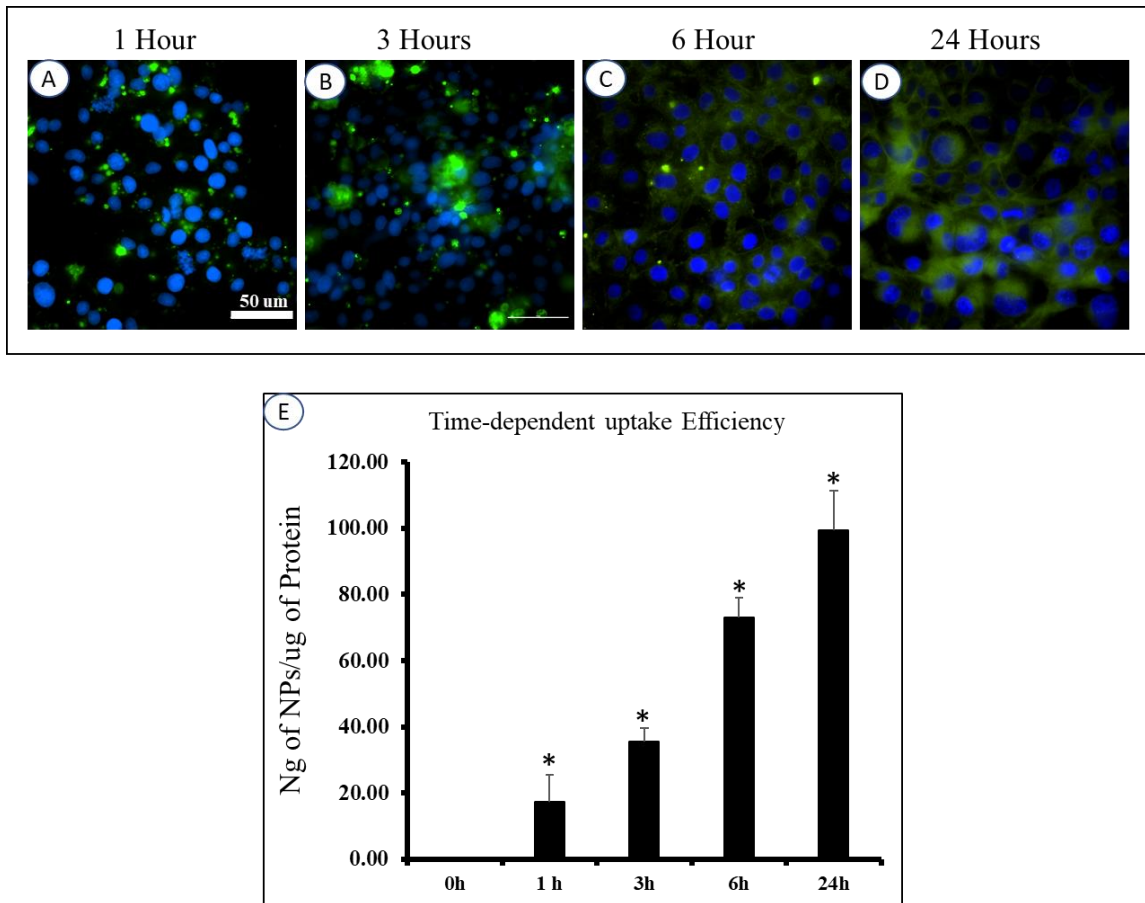
Figure 4. 14 - Time-dependent in vitro imaging of internalization of PSGL-1 conjugated FITC-PLGA nanoparticles (green) on activated MPBMECs. (E) Histogram showing ng of NPs internalized per ug of protein, $p < 0.05$, $n = 6$.

4.3.7 Evaluation of P188, growth factors, and NAC for cell migration

We evaluated the effect of non-biologics [Poloxamer 188(P188) and N-acetylcysteine (NAC)] and growth factors [erythropoietin (EPO) and vascular endothelial growth factor (VEGF)] in single and in combination on endothelial cell proliferation via a traditional scratch injury model. Images of cells captured at time 0 (T_0) (Fig. 4.15 and 4.17) for single and combination treatment. The white lines in the images define a specific analysis region that was identically placed within each well. Following 12 h of incubation (Fig. 4.16 and 4.18), BECs fills in and close the wound in positive control samples with a percentage closure of 37.1 +/- 1.8%, whereas negative control showed no significant activities with only 24.3 +/- 1.1%. The single treatment groups showed great migration with a closure percentage of about (60.6 +/- 0.7%, 60.4 +/- 1.4%, 65.8 +/- 1.9%, and 54

+/- 1.7%) for P188, EPO, VEGF, and NAC respectively (Fig. 4.16). As expected, the combination groups showed quite a significant migration with a percentage of (81.2 +/- 0.8%, 92.5 +/- 0.7%, and 90.7 +/- 1.55%) for P188 + EPO, P188 + VEGF, and P188 + NAC respectively (Fig. 4.18). These results indicate that the combination of either EPO, VEGF, and NAC with P188 have the potential for BECs migration and proliferation.
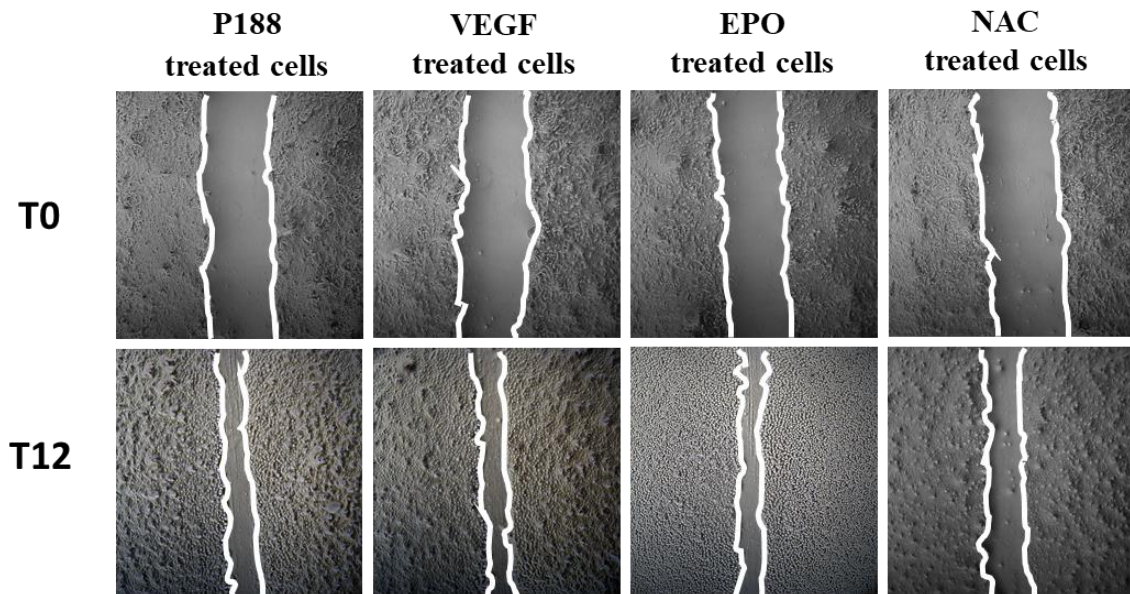
Figure 4. 15 - Representative phase-contrast micrographs of cells treated with VEGF (50 ng), P188 (500 uM), EPO (5 U), and NAC (5 mM) for 0 and 12 h (5× magnification).
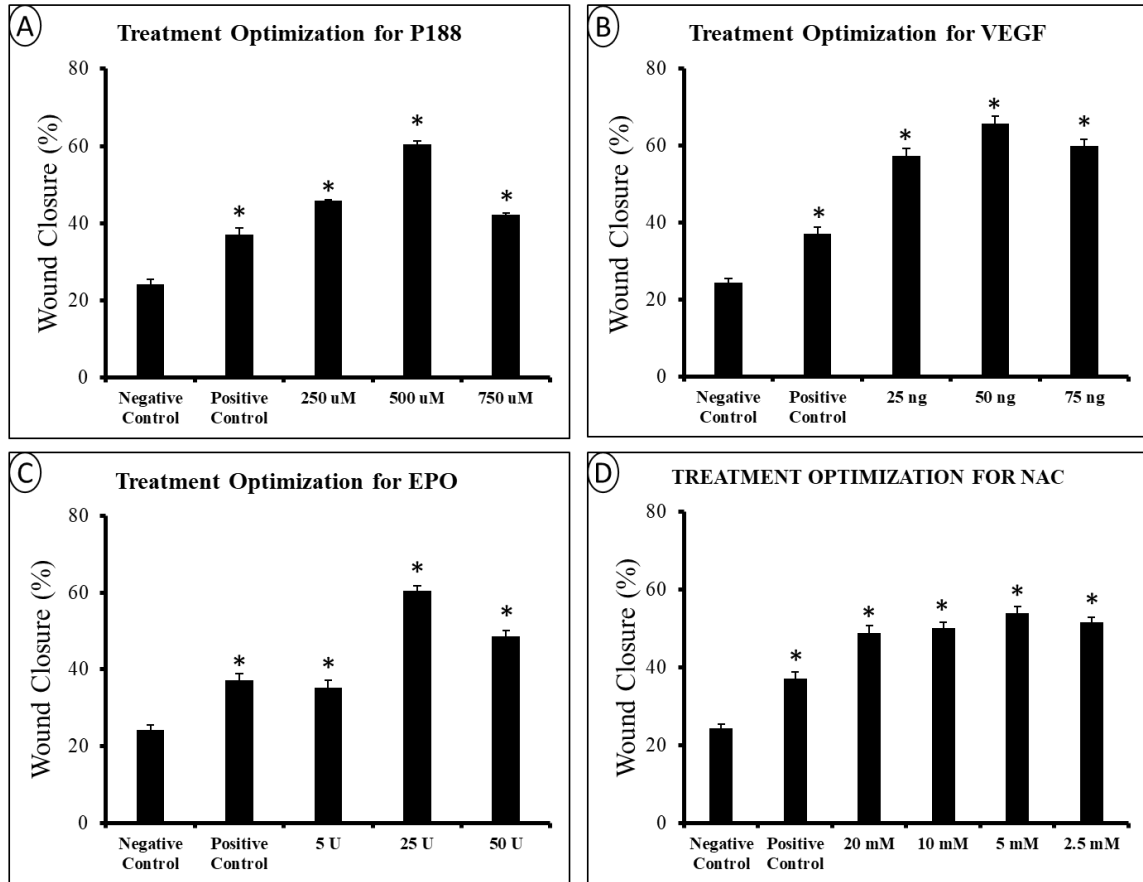
Figure 4. 16 - Graphs depicting the quantification of the effects of the different treatments on scratch wound healing. Average values obtained from three independent experiments. Wound closure rates are expressed as a percentage of scratch closure after 12 h compared to the initial area. (A) P188, (B) VEGF, (C) EPO, (D) NAC. All treatment groups were compared to the negative control, p < 0.05, n = 3.
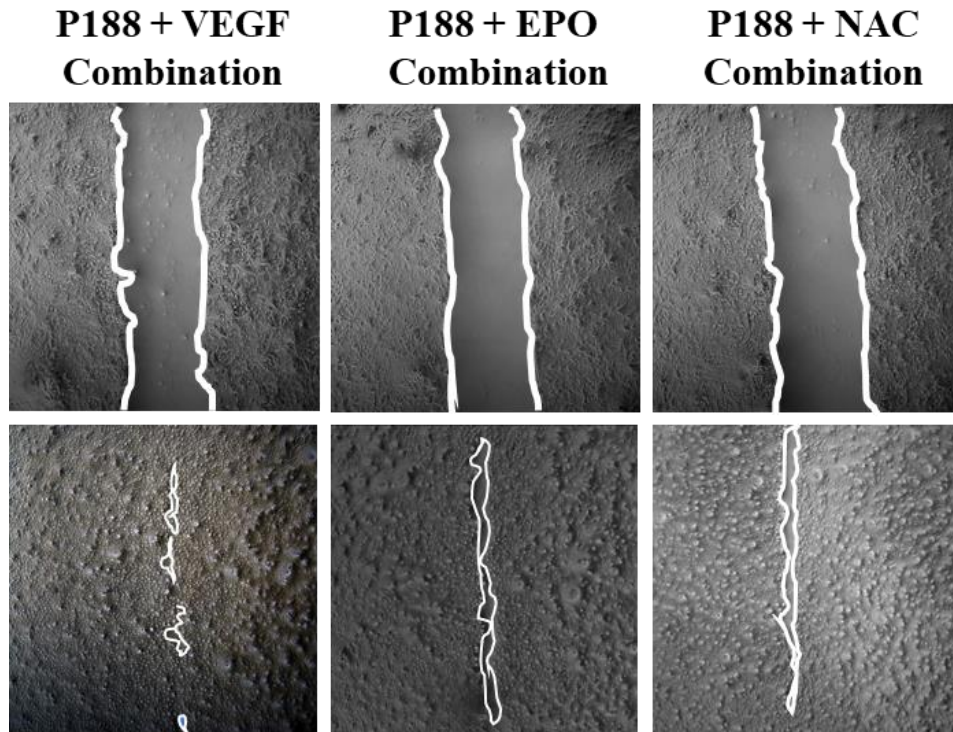
Figure 4. 17 - Representative phase-contrast micrographs of cells treated with P188 + VEGF, P188 + EPO, and P188 + NAC for 0 and 12 h (5× magnification).
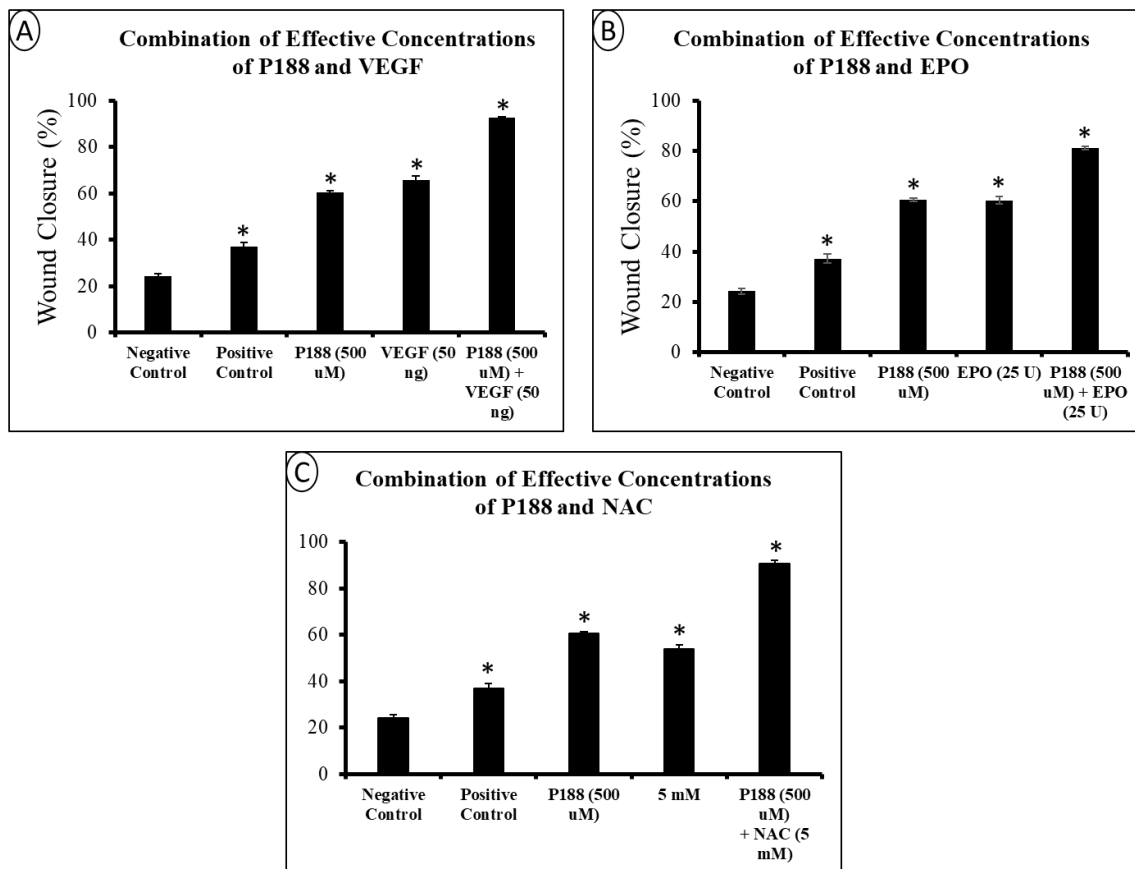
Figure 4. 18 - Quantification of the effects of combination treatments on scratch wound healing. Wound closure rates are expressed as a percentage of scratch closure after 12 h compared to the initial area. All treatment groups were compared to the negative control, p < 0.05, n = 3.

4.3.8. Effect of conjugated P188 + NAC on endothelial cell migration & crater closure

To determine the potency of conjugated P188 + NAC NPs to enhance proliferation, NPs were loaded with the combination of P188 and NAC and administered to the cells post- microcavitation to stimulate proliferation/migration. From the wound injury model, P188 and NAC showed great potential for cell migration (Fig. 4.19A and B). Therefore, we wanted to repopulate at a faster rate by conjugating P188 + NAC PLGA NPs with PSGL-1 for injury site targeting. Damaged brain endothelial cells were treated with PSGL-1 conjugated P188 + NAC PLGA NPs for 12 hours. P188 + NAC free drug was used as positive control while DMEM + 1% FBS was used as a negative control. Cells from both experimental and positive groups repopulated the crater areas within 12

hours (Fig. 4.19). Statistically, there was no difference in the crater closure between the experimental and positive groups (Fig. 4.19J). All results were compared to the negative control.
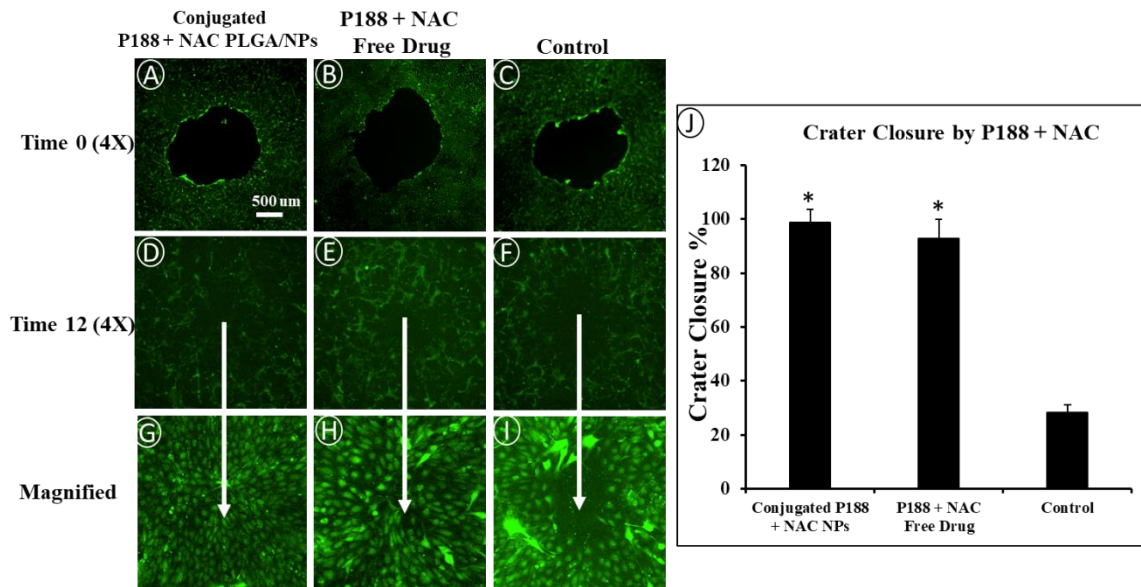
Figure 4. 19 - P188-NAC PLGA loaded NPs and P188-NAC free drug induces proliferation/migration after 12 hrs. to close injury crater. (A-C) injury site at time 0. (D-F) migration/proliferation induced by conjugated P188 + NAC NPs and P188 + NAC free drug after 12 hrs of treatment. (D – I) 10X magnification of "D – F" (J) Quantitative analysis of crater closure. Experimental groups compared to control, p < 0.05, n = 3.

4.3.9   Therapeutic effect of conjugated P188 + NAC NPs on BECs permeability

The therapeutic potentials of conjugated P188 + NAC NPs was further validated by measuring the permeability of 10 kDa dextran molecules across brain endothelial cells exposed to TNF-α and those treated with conjugated P188 + NAC NPs after TNF-α exposure. Since 10 kDa tracer is large in size, the permeability should be negligible in control cells as shown in Figure 4.20 below. However, there was an increased permeability in cells exposed to TNF-α compared to the baseline (EC monolayer). Interestingly, the treatment with conjugated P188 + NAC NPs for 12 h restored the permeability close to normal (Fig. 4.20). This confirmed that P188 + NAC have the capability to repair the BEC tight junction to prevent transport of large molecules.

10 KDa FLUORESCENT DEXTRAN
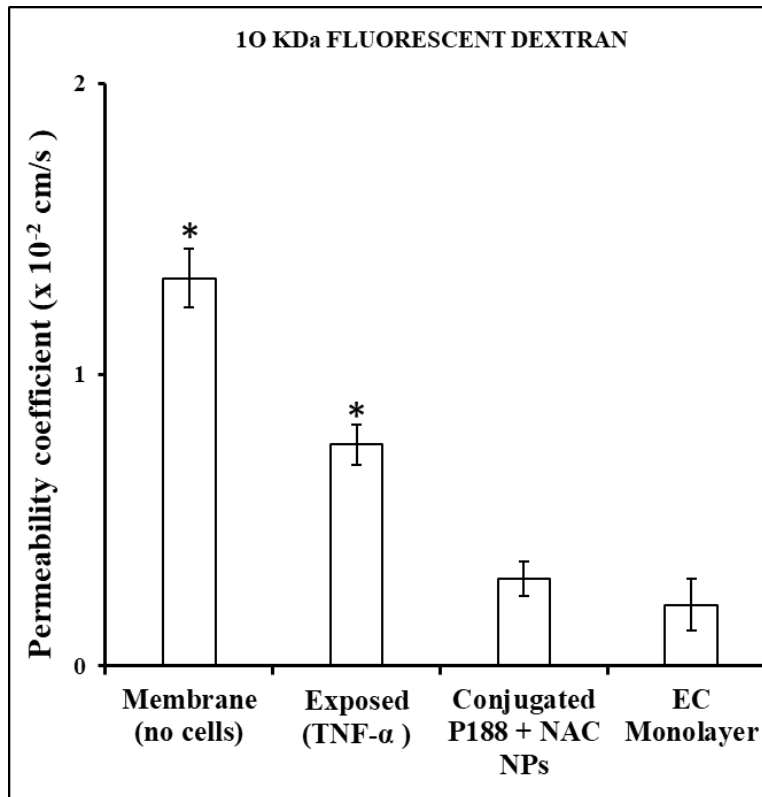
Figure 4. 20 - Graph showing the permeability coefficient (P) of 10 KDa. Increase in permeability is correlated to TNF-alpha exposure. However, treatment with conjugated P188 + NAC NPs significantly reduced the permeability. All groups compared to control (EC Monolayer) p < 0.05, n = 3.

4.3.10 Therapeutic effect of conjugated P188 + NAC NPs on GLUT1 expression

To test conjugated P188 + NAC NPs therapeutic potentials to repair disrupted tight junction proteins, we exposed the BECs to TNF-α (10ng/ml) for 4 hrs. and evaluated GLUT1 and ZO-1 expression. Immunocytochemistry detection indicates a substantial decrease in GLUT1 and ZO-1 expression in BECs exposed to TNF-α (Fig. 4.21A, D, and G) compared to control cells (Fig. 4.21 C, F, and I). Following treatment with conjugated P188 + NAC NPs, Immunocytochemistry showed significant restoration of the colocalized proteins (GLUT1 and ZO-1) (Fig. 4.21B, E, and H). These findings further provide evidence that P188 has therapeutic potential.
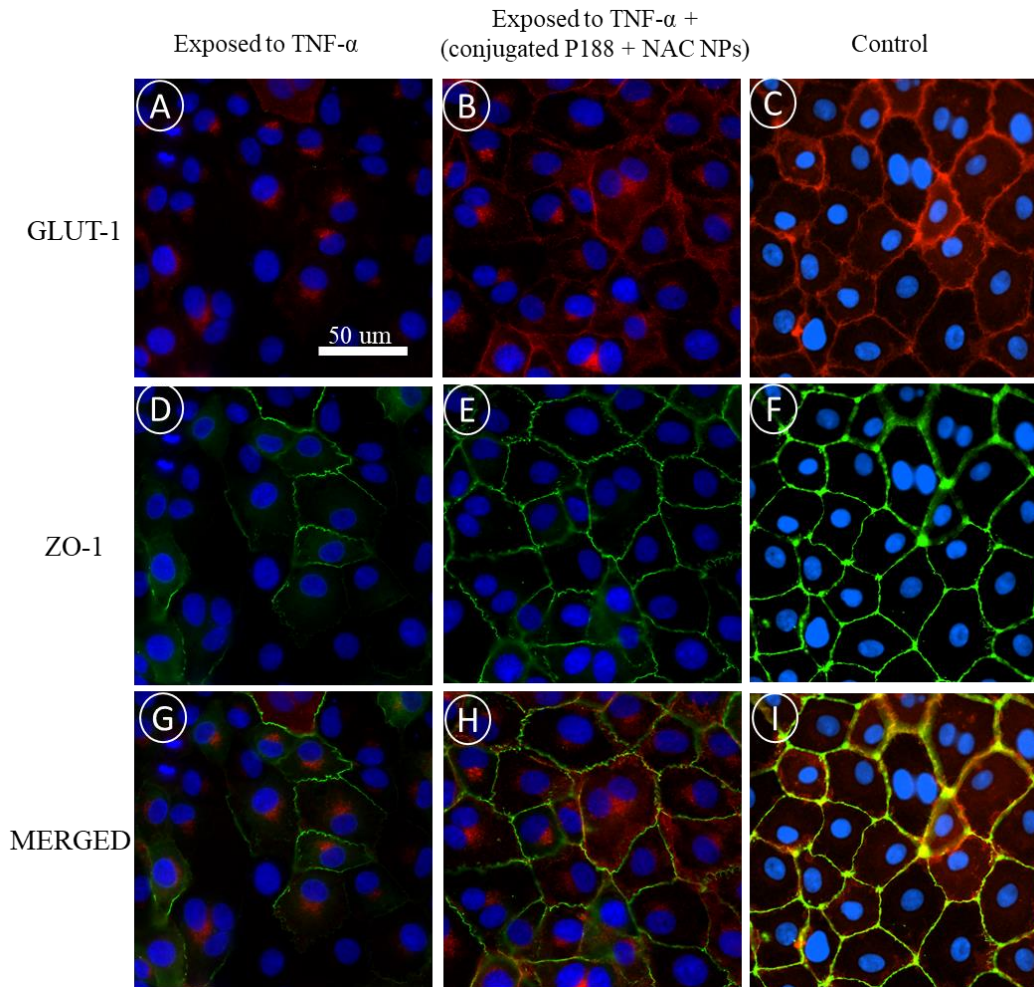
Figure 4. 21 - Therapeutic effects of P188 + NAC NPs on GLUT-1 and ZO-1 expression in mouse primary brain microvascular endothelial cells (MPBMECs) after the disruption of Brain Endothelium (BE) integrity by TNF-alpha. Immunofluorescent expression of GLUT-1(red), ZO-1(green), and merged image. DAPI (blue – nuclei).

4.4   <u>DISCUSSION</u>

For the effective treatment of disrupted brain endothelial cells, a theragnostic approach offers clinical advantages, including, delivering high drug concentrations to target the injury site, which can mediate enhanced therapeutic responses. We successfully developed and characterized drug-loaded PLGA NPs for various applications using transmission electron microscope (TEM) and dynamic light scattering techniques (Fig. 4.5 and Tab. 4.1). For proof of concept, fluorescent dye-loaded NPs were conjugated to peptides (PSGL) (conjugated FITC-PLGA NPs) following an

existing protocol [166] with few modifications to enhance stability, binding affinity, and specificity. The release kinetics for each drug was properly studied and calibrated for this study. Fluorescence-based or conjugated NPs enhances the potential to monitor targeted drug delivery in real-time. A polymer with the molecular weight that is capable of releasing drugs at the right physiological pH is of great necessity. We observed that PLGA (50/50) of molecular weight of 24,000 to 30,000 has a better releasing kinetic within the physiological conditions compared to other molecular weights. However, the loading efficiency by the double emulsion method was smaller than expected, especially with NAC. Normally, it would be expected that the loading would be high, but that is not the case here, which is in contradiction to what Andreas et al., [148] reported; that double emulsion is an adequate emulsification procedure for the encapsulation because of high encapsulation outcome [148]. Combining NAC with P188 will enhance the loading efficiency of NAC, because P188 has a larger molecular weight and it is a surfactant.

Following proof of concept, P188 and NAC were both used as drugs (Fig 4.6). The amount of drug-loaded in the delivery particle plays a great role in the rate and duration of drug release. It is speculated that particles with a higher drug content possess a larger initial burst release than those having lower content because of their smaller polymer to drug ratio [149]. Hydrophobic interactions and rapid degradation of particles have also been shown to play a part in the burst release [150]. For P188, most of the release took place after day 3 and then sustained after day 7 till day 28. This makes sense because the sustained release is very important in pharmaceutical industries to eliminate multiple applications [151]. However, sustained-release depends upon so many factors such as the amount of drugs loaded, the solvent used, temperature, drug characteristics, drug-polymer interactions, and rate of degradation [152]. On the contrary, NAC release was rapid as most of the release was after 12 h and sustained after 24 h for 7 days. Hundred percent of NAC was release after day 7. The fast release rate of NAC is attributed to its smaller molecular weight. In addition, NAC could have easily diffused through the NPs pores. The fast release phenomenon fits well into the aim of this study. NAC is an antioxidant, so releasing it early in the first few hours of the treatment process may enhance the suppression of reactive oxygen species (ROS) and block various inflammatory cascades, allowing P188 to promote migration and proliferation without superoxide inhibitions.

After characterizing the key features of brain endothelial cells (BECs) such as occludin, ZO-1, and actin filaments (Fig 4.7), we evaluated the cytotoxicity of P188, NAC, and P188 + NAC NPs on BECs by performing MTT assay. The results were compared with the cytotoxicity of blank-PLGA/NPs. The growth of cells was inhibited significantly by1500 – 2000 ug/ml concentrations of blank-PLGA/NPs (Fig 4.8A). Cell viability to P188 was tested by incubation cells with different concentrations (50 – 750 uM) of P188 solutions. We only observed a significant reduction in the cell viability at 750 uM (Fig 4.8B). NAC (2.5 – 20 mM) did not affect cell cytotoxicity at the tested concentrations (Fig 4.18C). The viability of MPBMECs was tested by incubating cells with (50, 100, 250, 500, 1000, 1500, and 2000 ug/ml) concentrations of P188 + NAC NPs. Only the 2000 ug/ml concentration showed a significant reduction in viability (Fig 4.8D). The synthesized NPs in our studies were deemed biocompatible and non-toxic to tissues and cells. In addition to appropriate biocompatibility and biodegradability [188], the size and surface properties of NPs have desirable effects on the pharmacokinetic and bio-disposition, and thus are key properties for consideration for biomedical applications [189]. The size of NPs is an important factor for biodistribution and blood clearance processes [190, 191]. For example, prolongation of NP circulation half-life, which can result in an improved time window for more efficient delivery of NPs to target organs, can be achieved by surface conjugation of nanoparticles. On the other hand, longer prolongation can lead to an increased toxicity. We have shown that conjugated P188-NAC NPs maintains cell viability after 24 hours incubation period. We did not test for longer exposure of brain endothelial cells (BECs) to PLGA NPs because the half-life of PLGA NPs in different organs is well documented. The average particle sizes ranged from 140 nm to 200 nm and were deemed suitable to evade both filtrations in livers and kidneys. The result is also supported by the negative surface zeta potential values of the NPs, which is in favor of a long-circulation in the blood [192, 193]. The half-life of PLGA in the lungs, heart, kidney, liver, and serum are 7.40 +/- 0.65, 11.34 +/- 2.25, 11.59 +/- 1.00, 8.15 +/- 0.47, and 6.05 +/- 0.78 hours respectively [194]. The PLGA nanoparticles have a unique drug delivery characteristic that can be used as intranasal sustained-release delivery vehicles [195] for P188 + NAC for potential treatment of the traumatic brain injuries.

To investigate the ability of conjugated NPs to target and specifically adhere to activated or injured endothelium, we first confirmed the expressions of E-selectins on injured BECs. A significant barrier that has impeded the systemic administration of NPs from reaching the target

site is endocytosis, degradation, and elimination [155]. These setbacks can be addressed by using a stable polymer and conjugated with a protein that is specific for the target site. PSGL-1 plays an important role in mediating adhesion and targeting activated endothelium and at the same time, help the PLGA NPs to avoid rapid recognition by the immune system. Our results indicated that PSGL-1 exhibited excellent recognition and targeting of endothelial cells activated by tumor necrotic factor-α (TNF-α). The MPBMECs that we used is a great model because it displays key characteristics that are present in an inflammatory microenvironment and promotes the expression of MMPs when activated. We were able to utilize specific receptor proteins to recognize and adhere to activated endothelial [153]. E-selectin, which is overexpressed in activated endothelial [87 and 88] were upregulated in brain endothelial cells exposed to TNF-α (Fig. 4.9) and TNF-α + Histamine (Fig. 4.10). It was also overexpressed in cells exposed to microcavitation (blasts) and returned to the incubator for one to three hours (Fig. 4.11). The fact that E-selectin is only expressed in injured, inflamed, diseased, or disrupted endothelial cells makes it a suitable candidate for therapeutic target, and it is also known to be involved in leukocyte recruitment toward activated endothelium.

Oxidative stress is an important determinant of endothelial injury [156] which influences a number of cellular responses by turning on several intracellular signaling cascades in endothelial cells, leading to the progression of vascular diseases [157]. We showed that TNF-α and Histamine stimulate ROS generation in endothelial cells (Fig. 4.12A-D), and then examined the effect of poloxamer 188, NAC (antioxidants), and P188 + NAC on ROS induced by TNF-α and Histamine. ROS expression was suppressed by these non-biological compounds (Fig. 4.12E-J). Significant effect was observed in cells treated with NAC and P188+NAC (Fig. 4.12G-H, I-J). Based on these observations, P188 and NAC may be able to accelerate vascular regeneration through ROS suppression. NAD(P)H oxidase is a major source of ROS generation in vascular endothelial cells, and critical in the regulation of oxidative stress in the vasculature [158]. Dysregulated NAD(P)H oxidase activity is associated with marked endothelial dysfunction in various states of vascular diseases [159]. Fluorescent intensity quantification depicts the effects of TNF-α and Histamine, and the therapeutic efficacy of P188 and NAC (Fig. 4.12K).

Upon confirmation of E-selectin expressions, FITC-PLGA NPs were conjugated and used. We tested the binding of such nanoprobes to E-selectin expressing primary brain endothelial cells.

We found that conjugated FITC-PLGA NPs selectively bound to the cell surface when incubated at 37° C (Fig. 4.13A-D). Protein concentration quantification also confirmed the uptake of the particles (Fig. 4.13E). Using confocal microscopy, we further observed the time-dependent uptake of conjugated FITC-PLGA NPs into endothelial, which overexpress E-selectin (Fig. 4.14). Quantifying the protein concentrations validated the time-dependent conjugated FITC-PLGA NPs. The binding of conjugated nanoparticles to endothelial cells is important for adequately evaluating target specificity and biodistribution of the E-selectin-targeted nanoparticles in brain endothelial cells. To determine whether the resulting conjugated FITC-PLGA NPs retain the target specificity to E-selectin-expressing cells, we incubated non-targeting FITC-PLGA-NPs with inactivated endothelial cells, which has a no level of E-selectin expression [167] at 37°C for 4 h. We detected a very small number of FITC-PLGA-NPs in the endothelial cells. Likewise, a few numbers of unconjugated FITC-PLGA-NPs were detected after incubating with E-selectin expressing endothelial cells (Fig. 4.13).

We tested the potency of poloxamer 188 (P188), vascular endothelial growth factor (VEGF), erythropoietin (EPO), and N-acetylcysteine (NAC) to regenerate disrupted or injured brain endothelial cells using wound injury model after 12 hrs. (Fig. 4.15). Wound healing is a complex and dynamic process, including inflammation, proliferation, and remodeling, in which migration of fibroblasts plays an essential role in wound repair [160]. P188 increases dermal cell migration, growth factor expression, and vascularization in a burn wound model [161]. The role of VEGF in wound healing is the stimulation of angiogenesis. Wound-healing angiogenesis involves multiple steps including vasodilation, basement membrane degradation, endothelial cell migration, and proliferation [162]. EPO can inhibit apoptosis and stimulate the proliferation and migration of mature endothelial cells and has effects on maturation and remodeling of the wounds [163]. NAC though not proven to be directly involved in wound closure, can attenuate ischemic renal failure in animal [164] and prevents acute renal dysfunction in noncardiac patients with chronic renal insufficiency exposed to small doses of contrast agents during computed tomography [165]. We investigated different concentrations of P188 (250, 500, and 750 uM) in serum-free media in this study and we observed 66.6% wound closure from the therapeutic dose (500 uM) (Fig. 4.16A). Various concentrations of VEGF (25, 50, 75 ng) was also investigated, and as expected, 65.8% wound closure was observed from the therapeutic dose (50 ng) (Fig. 4.16B). On the contrary, only 35.3% wound closure was observed from the therapeutic dose for EPO (5 U),

rather higher (60.4%) wound closure was observed with 25 U (Fig. 4.16C). Among the concentrations (2.5, 5, 10, and 20 mM) of NAC investigated, 54% wound closure was observed with the therapeutic dose (5 mM) (Fig. 4.16D). To investigate the combined efficacy of P188 + VEGF, P188 + EPO, and P188 + NAC, we incubated brain endothelial cells with scratch injury wound the different combination cocktails for 12 hrs. (Fig. 4.17). We observed 92.5%, 81.2%, and 90.7% wound closure with P188 + VEGF, P188 + EPO, and P188 + NAC treated cells respectively (Fig. 4.18). P188 + VEGF demonstrated a higher wound closure than the other two combination cocktails. However, the application of VEGF is limited by its poor stability at the room temperature. Hence, the need for a non-biological compound that is stable at and beyond room temperature. Therefore, we chose P188 + NAC as our best option and use for the remainder of the study.

We postulated from the scratch wound injury model results that the application of conjugated P188 + NAC NPs can proliferate and migrate BECs to fill damaged area induced by microcavitation (blasts). To test this hypothesis, monolayers of MPBMECs were preincubated with green cell tracker before blast exposure. Cells exposed to the blast were treated with conjugated P188 + NAC NPs for 12 h. fluorescent images were taken after 12 h were compared to those taken at the initial time point. To test the potency of the conjugated P188 + NAC NPs, the results were compared to positive control (P188 + NAC free drug), and negative control (DMEM with no drug) results (Fig. 4.19). We observed 98.7%, 92.9%, and 28.3% crater closure for conjugated P188 + NAC NPs, positive control, and negative control, respectively (Fig. 4.19J). This proves that with conjugated nanoparticles, we can target the injury area and enhance proliferation and migration.

In line with the findings from the crater closure by conjugated P188 + NAC NPs, we investigated the potential use of conjugated P188 + NAC NPs to restore permeability. Exposure of BECs to TNF-α induced an increase in the paracellular flux of labeled 10 kDa dextrans (Fig. 4.20). However, decreased permeability was observed in cells treated with conjugated P188 + NAC NPs (Fig. 4.20). Closer analysis of permeability in the treated cells indicates that the paracellular fluxes of 10 kDa dextran molecule demonstrated a steady-state dynamic throughout the experiment. Our results validate the potential of conjugated P188 + NAC NPs to be used for brain endothelial cell injury site targeting to restore disrupted blood-brain barrier. The permeability

result was supported by evaluating the effects of conjugated P188 + NAC NPs on disintegrated colocalized tight junction complex (GLUT1 and ZO-1). Our results demonstrate that TNF-α potentially compromised BBB integrity, as evidenced by a significantly decreased expression of GLUT1 and ZO-1. Interestingly, when the cells exposed to TNF-α were treated with conjugated P188 + NAC NPs, we observed restoration of GLUT1 and ZO-1 (Fig. 4.21). P188 + NAC has the potential to restore and regenerate. The mechanism of action regarding the combinatory therapy of P188 + NAC is yet to be elucidated.

4.5 <u>CONCLUSION</u>

In conclusion, the development of targeted therapeutic approaches provides a means to address an unmet clinical challenge in the treatment of traumatic brain injuries. The present study demonstrated the use of fluorescent NPs to visualize internalization in activated endothelial cells, and we report for the first time that a novel P188 + NAC combination has a direct effect on brain vascular endothelial cells; promoting proliferation and migration. Our findings provide a potential role for P188 + NAC in the regeneration of disrupted brain endothelial cells. This knowledge may contribute to the development of new therapies for other brain pathologies.

Chapter 5

5.1 <u>SUMMARY</u>

Development of a robust yet relatively simple *in vitro* cell-based method for predicting BBB permeability is urgently needed. A cell-based model offers the potential to account for paracellular drug/molecule diffusional processes, metabolism, and active transport processes. The cell-based model should also account for interactions between a drug and cells of interest for the development of an effective *in vitro* drug screening model. In addition, protocols need to be evaluated that may allow brain endothelial cell cultures to be more effectively exploited as a screening tool over longer passages without losing the key *in vivo* like characteristics of brain endothelial cells.

Mouse primary brain microvascular endothelial cells (MPBMECs) used in this project closely resemble the *in vivo* cell phenotype. In Chapter 2, we established and characterized an *in vitro* model of MPBMEC culture on a PETE membrane. Bio-transport properties were quantitatively determined, and changes in the permeability coefficients due to chemical (e.g., TNF-a) or mechanical (microcavitation) traumas have been experimentally measured. The FDA-approved amphiphilic copolymer (poloxamer P188) was shown to restore the permeability, which suggests the brain endothelium had been compromised but repaired by the P188 treatment. Such reparative effects of P188 are likely mediated by suppression of MMP-2 & 9 and by reestablishing the integrity of tight junction. These molecular events are postulated to attenuate the extent of damage caused by TBI. Finally, the model designed, developed, and tested in this study is simple to engineer, effective, reproducible, and convenient to be used as a platform for therapeutic studies.

In Chapter 3, we concluded that the disruption of the blood-brain barrier leads to an unregulated flow of glucose from the blood to the brain, causing hyperglycemia. The combination of the P188 + NAC cocktail showed a significant therapeutic potential to rescue and restore the neurospheroids sizes. Hence, the restored brain endothelium can improve the brain functionality by protecting the neural network and enhancing connectivity. To the best of our knowledge, such effects of P188 + NAC have not yet been reported. However, the mechanism(s) of P188 + NAC remains to be elucidated. Nonetheless, we presented a reliable and physiologically-relevant methodology to mimic the brain tissue and provided a therapeutic potential to mitigate hyperglycemia that might arise from altered BBB integrity.

In Chapter 4, we concluded that the development of targeted therapeutic approaches should provide a means to address an unmet clinical challenge in the treatment of traumatic brain injuries. The studies demonstrated the use of fluorescent NPs to visualize internalization in activated endothelial cells, and we reported for the first time that a novel P188 + NAC combination has a direct effect on brain vascular endothelial cells; promoting proliferation and migration. Our findings provide a potential role for P188 + NAC in the regeneration of disrupted brain endothelial cells. These findings may contribute to the development of new therapies for other brain pathologies.

5.2   LIMITATIONS AND ALTERNATE STRATEGIES

Before the adoption of a model, fundamental limitations must be addressed. One of the limitations of our model is the lack of flow (shear), as all experiments were done under static conditions. There is a need for the model to be modified to incorporate the dynamic blood flow to better mimic the physiological conditions. The blood-brain barrier model used in this study can be modified to include shear flow by incorporating a circulating or pulsating pump. This will enhance the investigation of the effect of blood flow on brain endothelial cells, interactions between drugs and cells, and bio-transport. Blood flow is physiologically relevant because oxygen supply to the brain and the removal of carbon dioxide are blood-flow dependent, meaning that the maintenance of normal physiological blood flow plays a significant role in regulating transport across the BBB [200].

Experimental outcomes remain to be computationally modeled. Such an effort may lead to overcome the challenge of laborious experiments and provide a comprehensive understanding of the BBB damage mechanism and subsequent consequences to the brain tissue [198, 199]. Also, all experiments were done in 2D; therefore, 3D models mimicking the brain tissue, and vasculature would be also helpful. The development of a physiologically relevant 3D brain model will extend the findings documented in this thesis. However, suitable 3D scaffolds for the brain tissue are not well established because of difficulties in the selection and characterization of the proper and adequate scaffold materials. The scaffold material properties play a critical role in cellular behavior [201, 202]. Selection of extracellular matrix material is one of the significant challenges in developing tissue-engineered models of the BBB since about 85% of the brain volume is cells

[203, 204]. Collagen 1 is mainly used in different labs as a viable scaffold for a wide range of applications [205, 206]. One of the main drawbacks to using collagen hydrogels as scaffolds for tissue engineering is that the collagen scaffolds are highly variable and dependent on many fabrication parameters, such as collagen source and gelation pH [207]. More importantly, collagen type I is not present in the healthy brain [204]. The extracellular space consists of a hyaluronic acid-based extracellular matrix and brain interstitial fluid [208, 209]. One may propose to use hyaluronic acid to engineer BBB models that will incorporate brain endothelial cells with neurons, astrocytes, and other glial cells for providing structural support for BBB.

In additionally, the potential alteration of brain endothelial cells caused by simultaneous exposure to both mechanical (microcavitation) and chemical (cocaine + alcohol) trauma should be further investigated. This type of combined traumas is speculated to result in cognitive and psychiatric problems [210], which are said to be a major contributor to long-term disability [211, 212]. Excessive use of psychostimulant drugs (PSDs) is one of the most common psychiatric problems following TBI. Cognitive impairment is estimated to occur in about 30% of patients suffering from mild TBI (mTBI) [213], and there is evidence showing an increased substance abuse following mTBI [214]. However, there is no clinical or experimental evidence on the combined effects of microcavitation and addictive use of PSDs. Understanding the mechanisms involved in restoration of the damage tissue may help in designing effective therapies. Therefore, the *in vitro* blood-brain barrier model designed in this thesis can be utilized to examine and characterize the outcome from the combined exposure of brain endothelial cells to microcavitation and PSDs.

Finally, the potential outcome of pre-treating cortical neurons with P188 + NAC before exposure to hyperglycemic conditions should be explored. In Chapter 2, we validated the protective effects of P188 against matrix metalloproteinases 2 and 9 (MMP-2 and 9), and NAC has also been shown to suppress MMP-9 expression [215]. In another study, it was reported that a bifunctional antioxidant acted as a neuroprotectant against hemin (oxidized form of heme)-induced damage in primary cultures of cerebellar granule neurons (CGNs) of rats [216]. However, strategies to protect the brain endothelium prior to a trauma are lacking. The BBB model that was used throughout this thesis may be utilized to determine the potential of pre-treatment of P188 + NAC to protect and maintain primary cortical neuron functionality.

APPENDIX
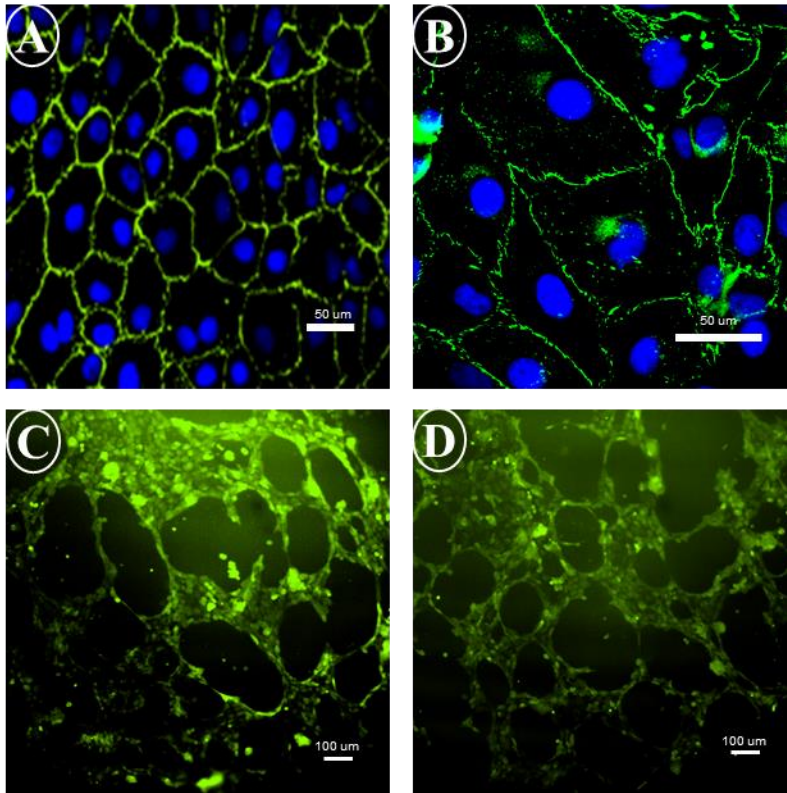
Appendix 1. (A and B) Immunofluorescence staining demonstrating the expression of endothelial cell tight junction-associated marker, ZO-1 (green) at passage 5 and 6 of culture respectively. Nuclei counter-stained with DAPI (blue). (C and D, passages 5 and 6) Reorganization of MPBMECs that were grown initially on top of a Matrigel for 6 hours into interconnecting cords of cells, appearing as a network of endothelial cells.

C

50 um

D

50 um
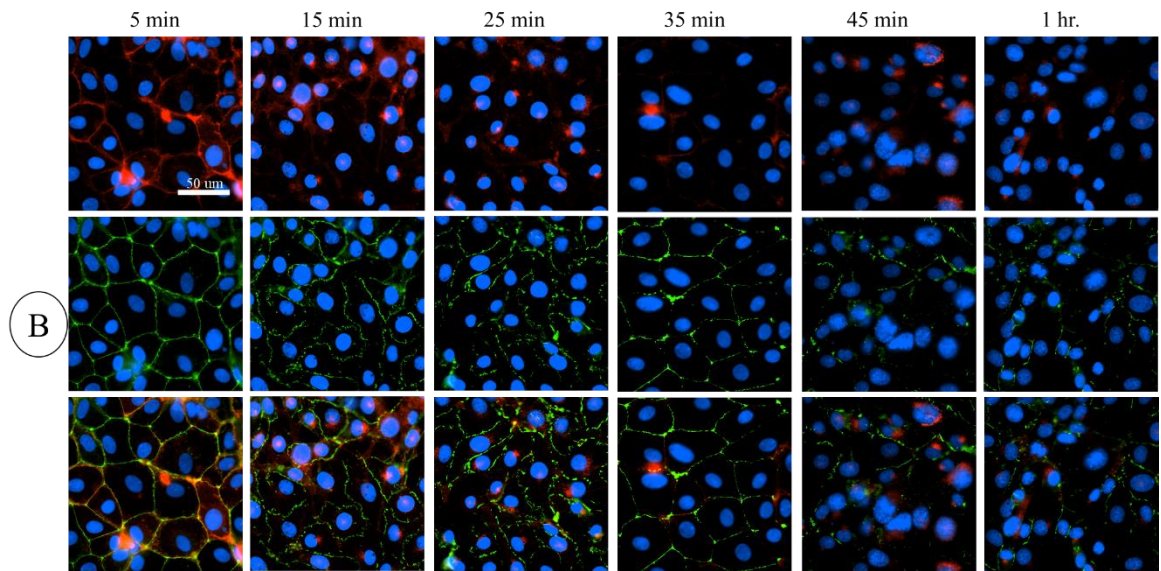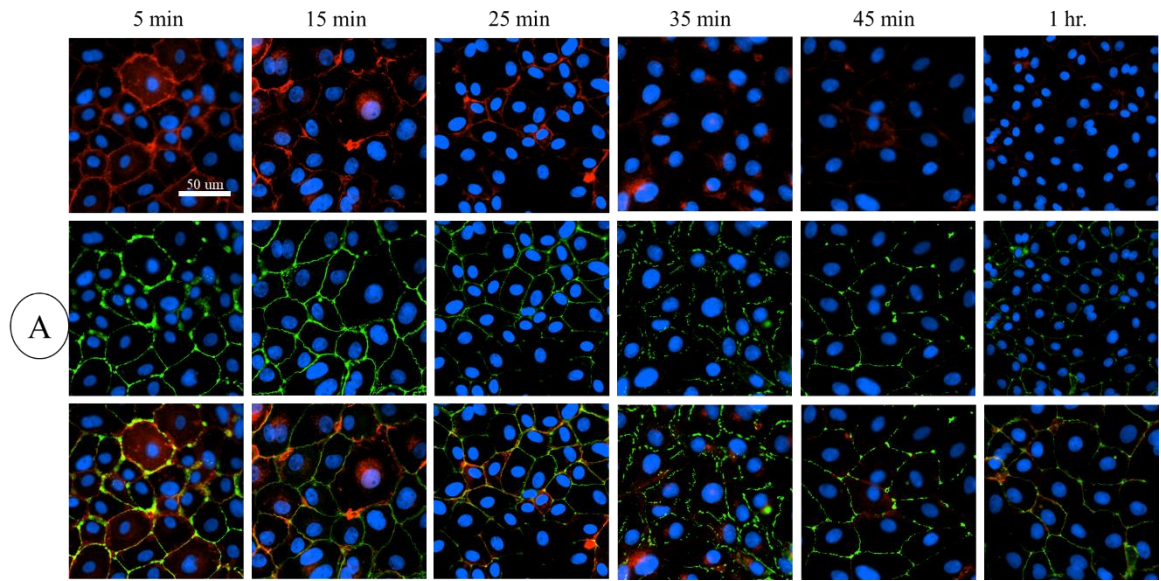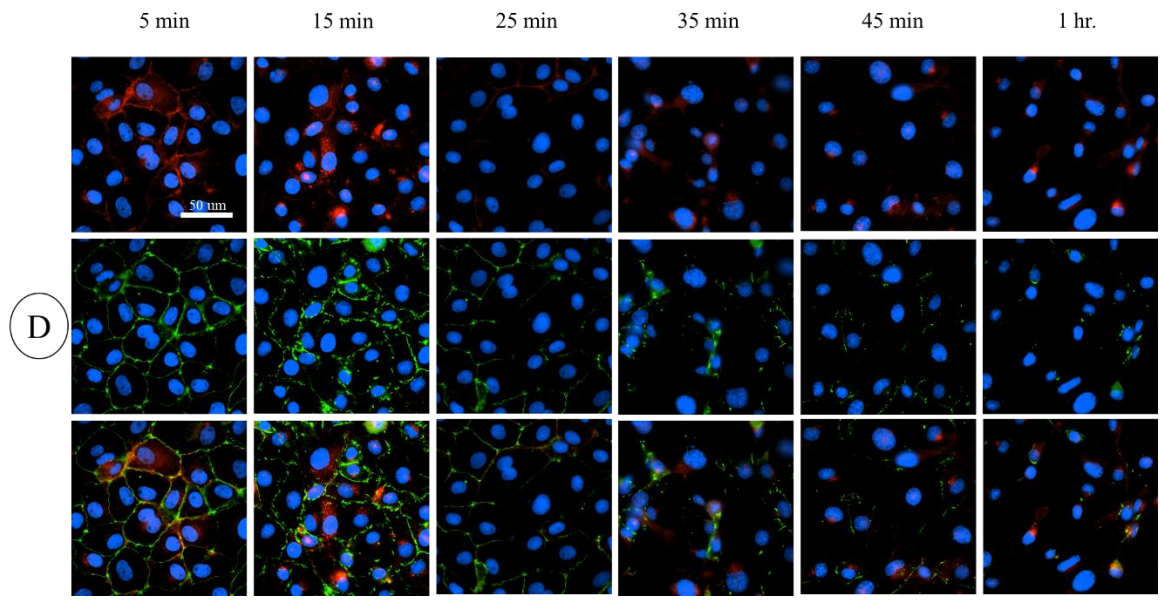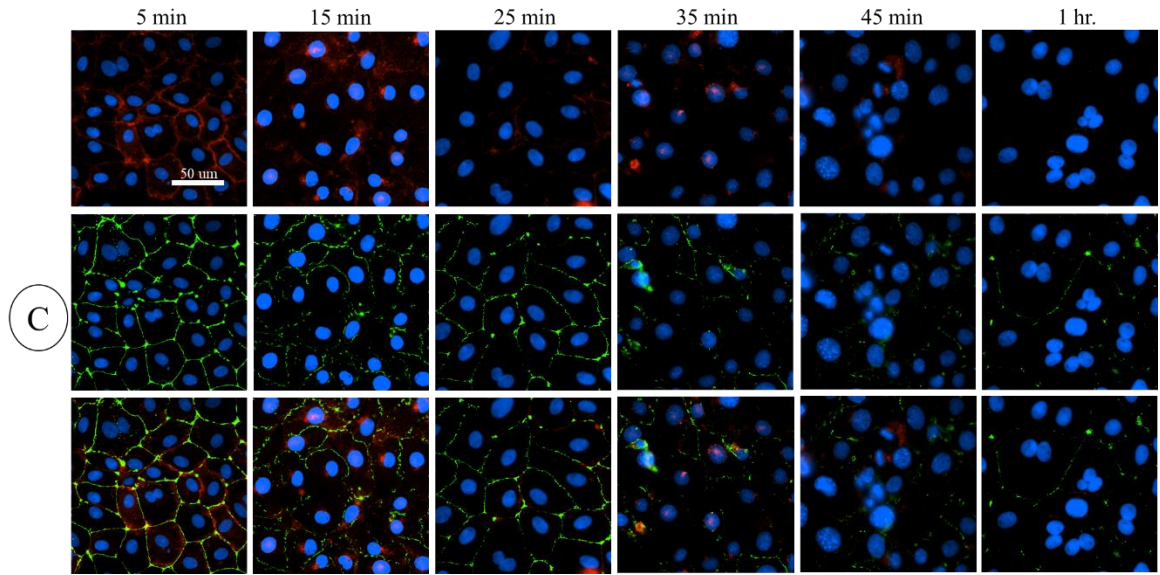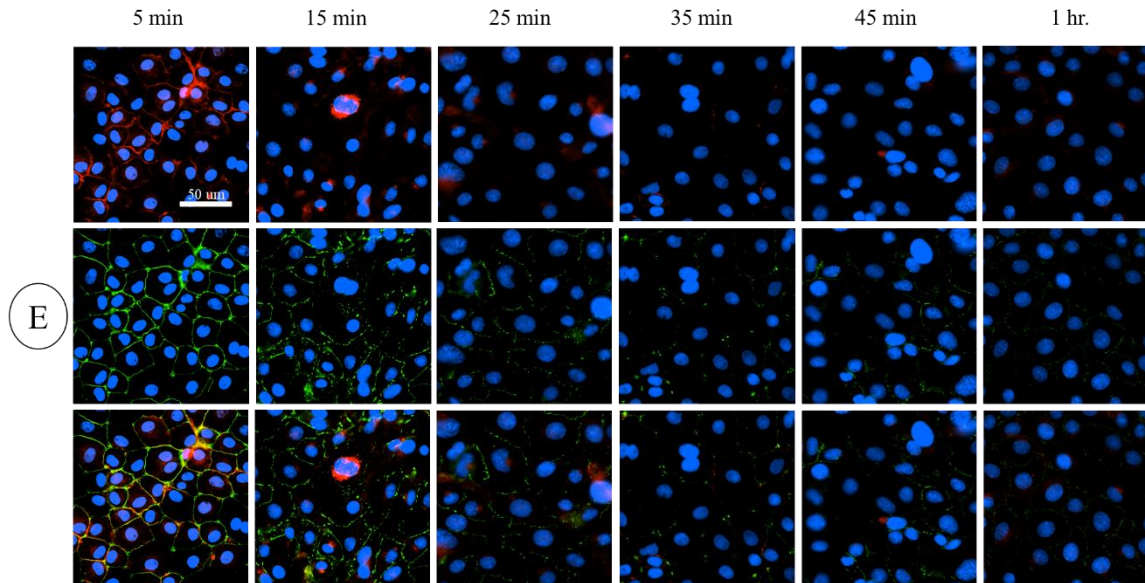
Appendix 2. Effects of Cocaine (**A** = 1 uM, **B** = 2.5 uM, **C** = 5 uM, **D** = 10 uM, and **E** = 20 uM) on ZO-1 expression in mouse primary brain microvascular endothelial cells (MPBMECs): Disruption of GLUT-1 affects the integrity of Brain Endothelium (BE). Immunofluorescent expression of GLUT-1(red), ZO-1(green) and merge image in MPBMECs. DAPI (blue - nuclei).

REFERENCES

1. Begley, D. J. & Brightman, M. W. Structural and functional aspects of the blood–brain barrier. Prog. Drug Res. 61, 40–78 (2003).
2. Hawkins, B. T. & Davis, T. P. The blood–brain barrier/neurovascular unit in health and disease. *Pharmacol. Rev.* 57, 173–185 (2005).
3. Pardridge, W. M. Blood–brain barrier drug targeting: the future of brain drug development. *Mol. Interv.* **3**,90–105 (2003).
4. Rajani R.M., Williams A. (2017) Endothelial cell–oligodendrocyte interactions in small vessel disease and aging. Clin. Sci. (Lond.) 131, 369–379.
5. Abbott, N.J., Rönnbäck, L. & Hansson, E. Astrocyte-endothelial interactions at the blood-brain barrier. *Nat. Rev. Neurosci.* **7**, 41–53 (2006).
6. Obermeier, B., Daneman, R. & Ransohoff, R.M. Development, maintenance and disruption of the blood-brain barrier. *Nat. Med.***19**, 1584–1596 (2013).
7. Ransohoff, R.M. & Engelhardt, B. The anatomical and cellular basis of immune surveillance in the central nervous system. *Nat. Rev. Immunol.* **12**, 623–635 (2012).
8. Butt, A. M., Jones, H. C. & Abbott, N. J. Electrical resistance across the blood–brain barrier in anaesthetized rats: a developmental study. *J. Physiol. (Lond.)* 429, 47–62 (1990).
9. Wolburg, H. & Lippoldt, A. Tight junctions of the blood–brain barrier: development, composition and regulation. *Vasc. Pharmacol.* 38, 323–337 (2002).
10. Abbott, N.J., Ronnback, L. and Hansson, E. 2006. Astrocyte–endothelial interactions at the blood–brain barrier. *Nature Reviews / Neuroscience*. 7, (Jan. 2006).
11. Yeh WL, Lin CJ, Fu WM: Enhancement of glucose transporter expression of brain endothelial cells by vascular endothelial growth factor derived from glioma exposed to hypoxia. Mol Pharmacol. 2008, 73 (1): 170-177. 10.1124/mol.107.038851.
12. Simpson IA, Carruthers A, Vannucci SJ: Supply and demand in cerebral energy metabolism: the role of nutrient transporters. J Cereb Blood Flow Metab. 2007, 27 (11): 1766-1791. 10.1038/sj.jcbfm.9600521.
13. Daneman, R. The blood-brain barrier in health and disease. *Ann. Neurol.* **72**, 648–672 (2012).
14. Aird, W.C. Phenotypic heterogeneity of the endothelium: I. Structure, function, and mechanisms. *Circ. Res.* **100**, 158–173 (2007).
15. Aird, W.C. Phenotypic heterogeneity of the endothelium: II. Representative vascular beds. *Circ. Res.* **100**, 174–190 (2007).
16. Neuwelt, E.A. *et al.* Engaging neuroscience to advance translational research in brain barrier biology. *Nat. Rev. Neurosci.***12**, 169–182 (2011).
17. Hallmann, R. *et al.* Expression and function of laminins in the embryonic and mature vasculature. *Physiol. Rev.* **85**, 979–1000 (2005).
18. Lyman M, Lloyd DG, Ji X, Vizcaychipi MP & Ma D. Neuroinflammation: the role and consequences. *Neurosci Res* 2014; 79: 1–12.

19. Furtado, D., Bjornmalm, M., Ayton, S., Bush, A.I., Kempe, K., Caruso F. Overcoming the blood-brain barrier: the role of nanomaterials in treating neurological diseases. Adv. Mater. (2018), p. e1801362

20. Didier, N. *et al.* Secretion of interleukin-1β by astrocytes mediates endothelin-1 and tumour necrosis factor-α effects on human brain microvascular endothelial cell permeability. *J. Neurochem.* 86, 246–254 (2003).

21. French, J.A. & Pedley, T.A. Clinical practice. Initial management of epilepsy. *N. Engl. J. Med.* **359**, 166–176 (2008).

22. Freese C, et al. 2014. A novel blood–brain barrier co-culture system for drug targeting of Alzheimer's disease: Establishment by using acitretin as a model drug. PLoS One 9:e91003.

23. Helms HC, et al. 2014. An electrically tight in vitro blood–brain barrier model displays net brain-to-blood efflux of substrates for the ABC transporters, P-gp, Bcrp and Mrp-1. AAPS J 16:1046–1055.

24. Eigenmann D, et al. 2013. Comparative study of four immortalized human brain capillary endothelial cell lines, hCMEC/D3, hBMEC, TY10, and BB19, and optimization of culture. Fluids Barriers CNS 10:33.

25. Helms HC, Brodin B. 2014. Generation of primary cultures of bovine brain endothelial cells and setup of cocultures with rat astrocytes. Methods Mol Biol 1135:365–382.

26. Garberg P, Ball M, Borg N et al (2005) In vitro models for the blood-brain barrier. Toxicol In Vitro 19(3):299–334.

27. Gaillard, P. J., Voorwinden, H., Nielsen, J., Ivanov, A., Atsumi, R., Engman, H., Ringbom, C., de Boer, A. G., and Breimer, D. D. (2001). Establishment and functional characterization of an in vitro model of the blood–brain barrier, comprising a co-culture of brain capillary endothelial cells and astrocytes. *Eur. J. Pharm. Sci.* 13:215–222.

28. Helms, H. C, Abbott, N. J, Burek, M, Cecchelli, R, et al. In vitro models of the blood–brain barrier: an overview of commonly used brain endothelial cell culture models and guidelines for their use. J Cereb Blood Flow Metab. 2016;36(5):862–90.

29. Meairs, S., Alonso, A. 'Ultrasound, microbubbles and the blood—brain barrier.' Prog. Biophysics Molecular Biol. 93 (2007): 354–362.

30. Adhikari U, Goliaei A, Berkowitz ML (2016) Nanobubbles, cavitation, shock waves and traumatic brain injury. Phys Chem Chem Phys 18:32638–32652.

31. Chodobski, A., Zink, B.J. & Szmydynger-Chodobska, J. Blood-brain barrier pathophysiology in traumatic brain injury. Transl. Stroke Res. 2, 492–516 (2011).

32. Prior S., Gander B., Lecaroz C., Irache J.M., Gamazo C. Gentamicin-loaded microspheres for reducing the intracellular *Brucella abortus* load in infected monocytes. J. Antimicrob. Chemother., 53 (2004), pp. 981-988.

33. Kinoshita, M., McDannold, N., Jolesz, F., Hynynen, K. Targeted delivery of antibodies through the blood–brain barrier by MRI-guided focused ultrasound. Biochem. Biophys. Res. Commun., 340 (2006), pp. 1085-1090

34. Dean O, Giorlando F, Berk M. *N*-acetylcysteine in psychiatry: current therapeutic evidence and potential mechanisms of action. *J Psychiatry Neurosci*. 2011;36(2):78-8621118657

35.   Rushworth GF, Megson IL. Existing and potential therapeutic uses for N-acetylcysteine: the need for conversion to intracellular glutathione for antioxidant benefits. Pharmakol Ther. 2014;141(2):150–159.

36.   Franzén, B. et al. Gene and protein expression profiling of human cerebral endothelial cells activated with tumor necrosis factor‑α. Mol. Brain Res. 115, 130–146 (2003).

37.   Kaya, D. et al. VEGF protects brain against focal ischemia without increasing blood–brain barrier permeability when administered intracerebro‑ventricularly. *J. Cereb. Blood Flow Metab. 25, 1111–1118 (2005).*

38.   Kawakami, M., Sekiguchi, M., Sato, K., Kozaki, S. & Takahashi, *M.* Erythropoietin receptor-mediated inhibition of exocytotic glutamate release confers neuroprotection during chemical ischemia. *J. Biol. Chem. 276, 39469–39475 (2001).*

39.   Martínez-Estrada, O. M. et al. Erythropoietin protects the in vitroblood–brain barrier against VEGF-induced permeability. *Eur. J. Neurosci. 18, 2538–2544 (2003).*

40.   Centers for Disease Control and Prevention (2016) Report to Congress on traumatic brain injury in the United States: Epidemiology and rehabilitation. National Center for Injury Prevention and Control; Division of Unintentional Injury Prevention, Atlanta.

41.   Blennow K, Brody DL, Kochanek PM, Levin H, McKee A, Ribbers GM, Yaffe K, Zetterberg H. Traumatic brain injuries. Nat Rev Dis Primers. 2016; 2:16084.

42.   Salzar, R.S., Treichler, D., Wardlaw, A., G. Weiss, Goeller J. (2017). Experimental investigation of cavitation as a possible damage mechanism in blast-induced traumatic brain injury in post-mortem human subject heads.

43.   Iwaskiw, A.S., Ott, K.A., Armiger, R.S., Wickwire, A.C., Alphonse, V.D., Voo, L.M., Carneal, C.M., Merkle, A.C.: The measurement of intracranial pressure and brain displacement due to short-duration dynamic overpressure loading. Shock Waves **28**(1) (2018).

44.   Janelidze S, Hertze J, Nagga K, Nilsson K, Nilsson C, Swedish Bio FSG, Wennstrom M, van Westen D, Blennow K, Zetterberg H, Hansson O (2017) Increased blood-brain barrier permeability is associated with dementia and diabetes but not an amyloid pathology or APOE genotype. Neurobiol Aging 51:104–112

45.   Sweeney, M.D., Sagare, A.P., Zlokovic. B.V., Blood-brain barrier breakdown in Alzheimer disease and other neurodegenerative disorders. Nat. Rev. Neurol., 14 (2018), pp. 133–150

46.   Coisne, C., Engelhardt, B., 2011. Tight junctions in brain barriers during central nervous system inflammation. Antioxid. Redox Signal. 15, 1285–1303.

47.   Ribecco-Lutkiewicz, M., Sodja, C., Haukenfrers, J., Haqqani, Arsalan., and Ly, D. 2018. A novel human induced pluripotent stem cell blood-brain barrier model: Applicability to study antibody-triggered receptor-mediated transcytosis. *Scientific Reports*. 8, (2018), 1873.

48.   Pardridge, W. M. Blood-brain barrier drug targeting: the future of brain drug development. *Mol Interv* 3(90–105), 151 (2003).

49.   Meairs, S. and Alonso, A. Ultrasound microbubbles and the blood-brain barrier. Prog. Biophys. Mol. Biol., 93 (2007), pp. 354-362.

50.   Collis, J., Manasseh, R., Liovic, P., Tho, P., and Ooi, A. et al. Cavitation microstreaming and stress fields created by microbubbles. Ultrasonics, 50 (2010), pp. 273-279.

51. Cheslow, L, Alvarez, JI. Glial-endothelial crosstalk regulates blood–Brain barrier function. Curr Opin Pharmacol 2016; 26: 39–46.

52. Smith, E. S., Jonason, A., Reilly, C., Veeraraghavan, J., Fisher, T., Doherty, M., et al. (2014). SEMA4D compromises blood-brain barrier activates microglia and inhibits remyelination in neurodegenerative disease. *Neurobiol. Dis.* 73C, 254–268.

53. Shetty AK, Mishra V, Kodali M, Hattiangady B (2014) Blood-brain barrier dysfunction and delayed neurological deficits in mild traumatic brain injury induced by blast shock waves. Front Cell Neurosci 8:232. doi:10.3389/fncel.2014.00232.

54. Wang, W. *et al.* Using functional and molecular MRI techniques to detect neuroinflammation and neuroprotection after traumatic brain injury Brain Behav. Immun., 64 (2017), pp. 344-353.

55. Pearson-Leary J, Eacret D, Chen R, et al. Inflammation and vascular remodeling in the ventral hippocampus contributes to vulnerability to stress. Transl. Psychiatry 7(1), e1160 (2017)

56. Abbott, N. J. Astrocyte–endothelial interactions and blood–brain barrier permeability. *J. Anat.* 200, 629–638 (2002).

57. Kacem K, Lacombe P, Seylaz J, Bonvento G**.** Structural organization of the perivascular astrocyte endfeet and their relationship with the endothelial glucose transporter: a confocal microscopy study. *Glia* 23, 1–10 (1998).

58. Bauer, H. C., Bauer, H. Neural induction of the blood–brain barrier: still an enigma. *Cellular Mol. Neurobiol.* 20, 13– 28 (2000).

59. Doggett, T. M., and Breslin, J. W. Acute alcohol intoxication-induced microvascular leakage. Alcohol Clin Exp Res, 38 (2014), pp. 2414-2426.

60. Sun, S., Kanagaraj, J., Cho, L., Kang, D., Xiao, S. and Cho, M. 2015. Characterization of Subcellular Responses Induced by Exposure of Microbubbles to Astrocytes. *Journal of Neurotrauma*. 32, 19 (2015), 1441–1448.

61. Goeller, J., Wardlaw, A., Treichler, D., O'Bruba, J., and Weiss, G. Investigation of cavitation as a possible damage mechanism in blast-induced traumatic brain injury. J Neurotrauma, 29 (2012), pp. 1970-1981.

62. Salzar, R.S., Treichler, D., Wardlaw, A., Weiss, G., Goeller, J.: Experimental investigation of cavitation as a possible damage mechanism in blast-induced traumatic brain injury in post-mortem human subject heads. J. Neurotrauma **34**(8), 1589–1602 (2017).

63. Kanagaraj, J., Chen, B., Xiao, S. and Cho, M. 2018. Reparative Effects of Poloxamer P188 in Astrocytes Exposed to Controlled MC. *Annals of Biomedical Engineering.* 46, 2 (2018), 354–364.

64. Arnaoutova, I. & Kleinman, H. K. *In vitro angiogenesis: endothelial cell tube formation on gelled basement membrane extract*. Nature Protoc. 5, 628–635 (2010).

65. psychcentral.com/news/2012/06/08/mild-brain-injury-in-combat-maylead-to-ptsd-/ 39891 .html].

66. Menon, V. & Uddin, L. Q. *Saliency, switching, attention and control: a network model of insula function. Brain Struct. Funct.*214, 655–667 (2010).

67. Moloughney, J. G. & Weisleder, N. *Poloxamer 188 (p188) as a membrane resealing reagent in biomedical applications*. *Recent Pat. Biotechnol.* **6**, 200–211 (2012).

68. Brilha, S., Ong, C., Weksler, B., Romero, N., Couraud, P.-O. and Friedland, J. 2017. Matrix metalloproteinase-9 activity and a downregulated Hedgehog pathway impair blood-brain barrier function in an in vitro model of CNS tuberculosis. *Scientific Reports*. 7, 1 (2017), 16031.

69. Wang, T., Chen, X., Wang, Z., Zhang, M., Meng, H., Gao, Y., Luo, B., Tao, L. and Chen, Y. 2015. Poloxamer-188 Can Attenuate Blood–Brain Barrier Damage to Exert Neuroprotective Effect in Mice Intracerebral Hemorrhage Model. *Journal of Molecular Neuroscience*. 55, 1 (2015), 240–250.

70. Abhyankar VV, Wu M, Koh C-Y, Hatch AV. (2016) A Reversibly Sealed, Easy Access, Modular (SEAM) Microfluidic Architecture to Establish In Vitro Tissue Interfaces. PLOS ONE 11(5): e0156341. doi: 10.1371/journal.pone.0156341.

71. Li, G., Simon, M., Cancel, L., Shi, Z.-D., Ji, X., Tarbell, J., Morrison, B. and Fu, B. 2010. The permeability of Endothelial and Astrocyte Cocultures: In Vitro Blood-Brain Barrier Models for Drug Delivery Studies. *Annals of Biomedical Engineering*. 38, 8 (2010), 2499–2511.

72. Kwak M, Musser AJ, Lee J, Herrmann A (2010) DNA-functionalised blend micelles: mix and fix polymeric hybrid nanostructures. Chem Commun 46:4935–4937.

73. Weksler, B. et al. 2005. Blood-brain barrier-specific properties of a human adult brain endothelial cell line. *The FASEB Journal*. 19, 13 (2005), 1872–1874.

74. Dejana, E., Tournier-Lasserve, E. and Weinstein, B. 2009. The Control of Vascular Integrity by Endothelial Cell Junctions: Molecular Basis and Pathological Implications. *Developmental Cell*. 16, 2 (2009), 209–221.

75. Tornavaca, O., Chia, M., Dufton, N., Almagro, L., Conway, D., Randi, A., Schwartz, M., Matter, K. and Balda, M. 2015. ZO-1 controls endothelial adherens junctions, cell-cell tension, angiogenesis, and barrier formation. *The Journal of Cell Biology*. 208, 6 (2015), 821–838.

76. Higashida, T., Kreipke, C.W., Rafols, J.A., Peng, C., Schafer, S., Schafer, P., Ding, J.Y., Dornbos 3rd, D., Li, X., Guthikonda, M., Rossi, N.F., Ding, Y., 2011. The role of hypoxia-inducible factor-1alpha, aquaporin-4, and matrix metalloproteinase-9 in blood brain barrier disruption and brain edema after traumatic brain injury. J. Neurosurg.114, 92–101.

77. Yang, Y., Thompson, J.F., Taheri, S., Salayandia, V.M., McAvoy, T.A., Hill, J.W., Yang, Y., Estrada, E.Y., Rosenberg, G.A., 2013. Early inhibition of MMP activity in ischemic rat brain promotes expression of tight junction proteins and angiogenesis during recovery. J. Cereb. Blood Flow Metab. 33, 1104–1114.

78. Mark, K.S., Davis, T.P., 2002. Cerebral microvascular changes in permeability and tight junctions induced by hypoxia-reoxygenation. Am. J. Physiol. Heart Circ. Physiol. 282, H1485–1494.

79. Kousik, S.M., Napier, T.C., Carvey, P.M. The effects of psychostimulant drugs on blood brain barrier function and neuroinflammation Front. Pharmacol., 3 (2012).

80. Abbott, N. J., Patabendige, A. A., Dolman, D. E., Yusof, S. R., and Begley, D. J. (2010). Structure and function of the blood-brain barrier. *Neurobiol. Dis.* 37, 13–25.

81. Madsen, S. J., and Hirschberg, H. (2010). Site-specific opening of the blood-brain barrier. *J Biophotonics* 3, 356–367.

82. Vannucci SJ, Maher F, Simpson IA. Glucose transporter proteins in brain: delivery of glucose to neurons and glia. Glia 1997 Sep;21(1):2-21.

83.   Birnbaum MJ, Haspel HC, Rosen OM. Cloning and characterization of a cDNA encoding the rat brain glucose-transporter protein. Proc Natl Acad Sci U S A 1986 Aug; 83(16):5784-5788.

84.   Bondy CA, Lee WH, Zhou J. Ontogeny and cellular distribution of brain glucose transporter gene expression. Mol Cell Neurosci 1992 Aug;3(4):305-314.

85.   Morgello S, Uson RR, Schwartz EJ, Haber RS. The human blood-brain barrier glucose transporter (GLUT1) is a glucose transporter of gray matter astrocytes. Glia 1995 May;14(1):43-54.

86.   Pardridge WM. Blood-brain barrier biology and methodology. J Neurovirol 1999 Dec;5(6):556-569.

87.   Pardridge WM, Boado RJ, Farrell CR. Brain-type glucose transporter (GLUT-1) is selectively localized to the blood-brain barrier. Studies with quantitative western blotting and in situ hybridization. J Biol Chem 1990 Oct 15;265(29):18035-18040.

88.   Farrell CL, Yang J, Pardridge WM. GLUT-1 glucose transporter is present within apical and basolateral membranes of brain epithelial interfaces and in microvascular endothelia with and without tight junctions. J Histochem Cytochem 1992 Feb;40(2): 193-199.

89.   Klip A, Tsakiridis T, Marette A, Ortiz PA. Regulation of expression of glucose transporters by glucose: a review of studies in vivo and in cell cultures. FASEB J 1994 Jan; 8(1):43-53.

90.   Au KK, Liong E, Li JY, Li PS, Liew CC, Kwok TT, et al. Increases in mRNA levels of glucose transporters types 1 and 3 in Ehrlich ascites tumor cells during tumor development. J Cell Biochem 1997 Oct 1;67(1):131-135.

91.   Vemula S, Roder KE, Yang T, Bhat GJ, Thekkumkara TJ, Abbruscato TJ. A functional role for sodium-dependent glucose transport across the blood-brain barrier during oxygen glucose deprivation. J Pharmacol Exp Ther 2009 Feb;328(2):487-495.

92.   Ngarmukos C., Baur E. L. and Kumagai A. K. (2001) Co-localization of GLUT1 and GLUT4 in the blood–brain barrier of the rat ventromedial hypothalamus. *Brain Res.* 900, 1– 8.

93.   Dick A, Harik S, Klip A, Walker D. Identification and characterization of the glucose transporter of the blood–brain barrier by cytochalasin B binding and immunological reactivity. *Proc Natl Acad Sci U S A* 1984; 81: 7233 7.

94.   Nottet H, Persidsky Y, Sasseville VG *et al.* Mechanisms for the transendothelial migration of HIV-1-infected monocytes into brain. *J Immunol* 1996; 156: 1284 95.

95.   Sasseville VG, Newman WA, Lackner AA *et al.* Elevated vascular cell adhesion molecule-1 in AIDS encephalitis induced by simian immunodeficiency virus. *Am j Pathol 1992; 141: 1921 30.*

96.   Sasseville VG, Newman W, Brodie SJ, Hesterberg P, Pauley D, Ringler DJ. Monocyte adhesion to endothelium in simian immunodeficiency virus-induced AIDS encephalitis is mediated by vascular cell adhesion molecule-1/alpha 4 beta 1 integrin interactions. *Am J Pathol* 1994; 144: 2740.

97.   Fiala, M., Singer, E. J., Commins, D., Mirzapoiazova, T., Verin, A., Espinosa, A., Ugen, K., Bernas, M., Witte, M., Weinand, M., and Lossinsky, A. S. (2008). HIV-1 Antigens in neurons of cocaine-abusing patients. *Open Virol. J.* 2, 24–31.

98.   Dhillon, N. K., Peng, F., Bokhari, S., Callen, S., Shin, S. H., Zhu, X., Kim, K. J., and Buch, S. J. (2008). Cocaine-mediated alteration in tight junction protein expression and

modulation of CCL2/CCR2 axis across the blood-brain barrier: implications for HIV-dementia. *J. Neuroimmune Pharmacol.* 3, 52–56.

99. Dallasta, L. M., Pisarov, L. A., Esplen, J. E., Werley, J. V., Moses, A. V., Nelson, J. A., Achim, C. L. (1999) Blood-brain barrier tight junction disruption in human immunodeficiency virus-1 encephalitis. *Am. J. Pathol.* 155, 1915– 1927.

100. Persidsky, Y., Gendelman, H. E. (2003) Mononuclear phagocyte immunity and the neuropathogenesis of HIV-1 infection. *J. Leukoc. Biol.* 74, 691– 701.

101. Gaspar, J.M., Castilho, Á., Baptista, F.I., Liberal, J., and Ambrósio, A.F. Long-term exposure to high glucose induces changes in the content and distribution of some exocytotic proteins in cultured hippocampal neurons. Neuroscience, 171 (2010), pp. 981-992

102. Christianson, J.A. Ryals, J.M. Johnson, M.S., Dobrowsky, R.T. Wright, D.E. Neurotrophic modulation of myelinated cutaneous innervation and mechanical sensory loss in diabetic mice. Neuroscience, 145 (2007), pp. 303-313

103. Giannini, S., Benvenuti, S., Luciani, P. et al. Intermittent high glucose concentrations reduce neuronal precursor survival by altering the IGF system: the involvement of the neuroprotective factor DHCR24 (Seladin-1). J. Endocrinol., 198 (2008), pp. 523-532

104. Tomlinson, D.R. Gardiner, N.J. Glucose neurotoxicity. Nat. Rev. Neurosci., 9 (2008), pp. 36-45

105. Akude, E., Zherebitskaya, E., Chowdhury, S.K. et al. Diminished superoxide generation is associated with respiratory chain dysfunction and changes in the mitochondrial proteome of sensory neurons from diabetic rats. Diabetes, 60 (2011), pp. 288-297

106. Chowdhury, S.K., Zherebitskaya, E., Smith, D.R. et al Mitochondrial respiratory chain dysfunction in dorsal root ganglia of streptozotocin-induced diabetic rats and its correction by insulin treatment. Diabetes, 59 (2010), pp. 1082-1091.

107. Rushworth GF, Megson IL. Existing and potential therapeutic uses for N-acetylcysteine: the need for conversion to intracellular glutathione for antioxidant benefits. Pharmakol Ther. 2014;141(2):150–159.

108. Itoh, Y., Abe, T, Takaoka, R & Tanahashl, N. Fluorometric determination of glucose utilization in neurons in vitro and in vivo. J. Cereb. Blood Flow Metab. 24, 993-1003 (2004).

109. Abdul Muneer et al. Impairment of brain endothelial glucose transporter by methamphetamine causes blood-brain barrier dysfunction. Molecular Neurodegeneration 2011 6:23.

110. Ueta, K. *et al. Long-term treatment with the Na^+-glucose cotransporter inhibitor T-1095 causes sustained improvement in hyperglycemia and prevents diabetic neuropathy in Goto-Kakizaki rats*. *Life Sci.* **76**, 2655–2668 (2005).

111. Smith, A. G. & Singleton, J. R. *Impaired glucose tolerance and neuropathy*. *Neurologist* 14, 23–29 (2008).

112. Vincent, A. et al., 2011. Diabetic neuropathy: cellular mechanisms as therapeutic targets. Nat. Rev. Neurol., 7 (2011), pp. 573-583.

113. Hattangady, N.G., Rajadhyaksha, N.G. A brief review of in vitro models of diabetic neuropathy. International Journal of Diabetes in Developing Countries, 29 (2009), pp. 143-149

114. Vincent, A.M., Edwards, J.L., McLean, L.L., et al. Mitochondrial biogenesis and fission in axons in cell culture and animal models of diabetic neuropathy Acta Neuropathol., 120 (2010), pp. 477-489.

115. Xu X, Jiang H, Liu H, Zhang W, Xu X, Li Z (2012) The effects of galanin on dorsal root ganglion neurons with high glucose treatment in vitro. Brain Res Bull 87: 85–93.

116. Russell, J. W., Golovoy, D., Vincent, A. M., and Mahendru P. et al. High glucose-induced oxidative stress and mitochondrial dysfunction in neurons. FASEB J., 16 (2002), pp. 1738-1748.

117. Arnal, E., Miranda, M., and Barcia, J., et al. Lutein and docosahexaenoic acid prevent cortex lipid peroxidation in streptozotocin-induced diabetic rat cerebral cortex. Neuroscience, 166 (2010), pp. 271-278.

118. Chen, B., Tjahja, J., Malla, S., Liebman, C. and Cho, M. Astrocyte Viability and Functionality in Spatially Confined Microcavitation Zone. *ACS Applied Materials & Interfaces* 2019 *11* (5), 4889-4899. DOI: 10.1021/acsami.8b21410.

119. Sharma, H. S., Muresanu, D., Sharma, A., Patnaik, R. Cocaine-induced breakdown of the blood–brain barrier and neurotoxicity. Int. Rev. Neurobiol., 88 (2009), pp. 297-334.

120. Kinoh, H., Sato, H., Tsunezuka, Y., Takino, T. Kawashima, et al. MT-MMP, the cell surface activator of proMMP-2 (pro-gelatinase A), is expressed with its substrate in mouse tissue during embryogenesis. J. Cell Sci., 109 (Pt 5) (1996), pp. 953-959

121. Nair, M. P., Schwartz, S. A., et al. Drug abuse and neuropathogenesis of HIV infection: role of DC-SIGN and IDO. J. Neuroimmunol., 157 (2004), pp. 56-60.

122. Lin, C. H., Lin, K. F., Mar, K., Lee, S. Y., Lin, Y. M. Antioxidant N-acetylcysteine and glutathione increase the viability and proliferation of MG63 cells encapsulated in the gelatin methacrylate/VA-086/blue light hydrogel system. Tissue Eng. Part C Methods, 22 (2016), pp. 792-800.

123. Lee, H.-K. *et al*. Three-Dimensional Human Neuro-Spheroid Model of Alzheimer's Disease Based on Differentiated Induced Pluripotent Stem Cells. *PLoS One* 11, e0163072 (2016).

124. Jorfi M, D'Avanzo C, Tanzi RE, Kim DY, Irimia D. Human neurospheroid arrays for in vitro studies of Alzheimer's disease. Sci Rep. 2018; 8:2450.

125. Jorfi, M., D'Avanzo, C., Kim, D. Y. & Irimia, D. Three-Dimensional Models of the Human Brain Development and Diseases. *Adv. Healthc. Mater.* **7**, 1700723 (2018).

126. Jeong, G. S. *et al*. Networked neural spheroid by neuro-bundle mimicking nervous system created by topology effect. *Mol. Brain* 8, 17 (2015).

127. Chiba H, Osanai M, Murata M, Kojima T, Sawada N. Transmembrane proteins of tight junctions. Biochimica Et Biophysica Acta-Biomembranes. 2008;1778(3):588–600. Pmid :ISI:000254691500004.

128. Mizuno, N., Niwa, T., Yotsumoto, Y., and Sugiyama, Y., Impact of drug transporter studies on drug discovery and development. *Pharmacol. Rev.*, 55,425–461 (2003).

129. Dejana E, Orsenigo F, Lampugnani MG. The role of adherens junctions and VE-cadherin in the control of vascular permeability. Journal of Cell Science. 2008;121(13):2115–22. pmid:ISI:000256879900002.

130. Cecchelli R, Berezowski V, Lundquist S, Culot M, Renftel M, Dehouck MP, et al. Modelling of the blood-brain barrier in drug discovery and development. Nature Reviews Drug Discovery. 2007;6(8):650–61. pmid: ISI:000248486400020.

131. Buckley CD, Gilroy DW, Serhan CN, Stockinger B, Tak PP. The resolution of inflammation. Nature reviews Immunology. 2013; 13:59–66.

132. Molinaro R, Boada C, Del Rosal GM, Hartman KA, Corbo C, Andrews ED. et al. Vascular Inflammation: A Novel Access Route for Nanomedicine. Methodist Debakey Cardiovasc J. 2016; 12:169–74.

133. Pober JS, Sessa WC. Evolving functions of endothelial cells in inflammation. Nat Rev Immunol. 2007; 7:803–15.

134. Galvani S, Sanson M, Blaho VA, Swendeman SL, Obinata H, Conger H. et al. HDL-bound sphingosine 1-phosphate acts as a biased agonist for the endothelial cell receptor S1P1 to limit vascular inflammation. Sci Signal. 2015;8:ra79.

135. Zhang S, Ermann J, Succi MD, Zhou A, Hamilton MJ, Cao B. et al. An inflammation-targeting hydrogel for local drug delivery in inflammatory bowel disease. Science translational medicine. 2015; 7:300ra128.

136. Gilroy DW, Lawrence T, Perretti M, Rossi AG. Inflammatory resolution: new opportunities for drug discovery. Nature reviews Drug discovery. 2004; 3:401–16.

137. Xie J, Lee S, Chen X. Nanoparticle-based theranostic agents. Adv Drug Deliv Rev. 2010; 62:1064–79.

138. Yang B, Han X, Ji B, Lu R. Competition Between Tumor and Mononuclear Phagocyte System Causing the Low Tumor Distribution of Nanoparticles and Strategies to Improve Tumor Accumulation. Curr Drug Deliv. 2016;13:1261–74.

139. Helms HC, Abbott NJ, Burek M, Cecchelli R, Couraud PO, Deli MA, Forster C, Galla HJ, Romero IA, Shusta EV, et al. In vitro models of the blood–brain barrier: an overview of commonly used brain endothelial cell culture models and guidelines for their use. J Cereb Blood Flow Metab. 2016;36(5):862–90.

140. Wolff A, Antfolk M, Brodin B, Tenje M (2015) In vitro blood-brain barrier models-an overview of established models and new microfluidic approaches. J Pharm Sci. doi: 10.1002/jps.24329.

141. Banerjee, J, Shi, Y, Azevedo, HS. In vitro blood-brain barrier models for drug research: state-of-the-art and new perspectives on reconstituting these models on artificial basement membrane platforms. Drug Discov Today 2016; 21: 1367–1386.

142. Nehoff H, Parayath NN, Domanovitch L, Taurin S, Greish K. Nanomedicine for drug targeting: strategies beyond the enhanced permeability and retention effect. Int J Nanomedicine. 2014;9:2539–55.

143. Doane TL, Burda C. The unique role of nanoparticles in nanomedicine: imaging, drug delivery, and therapy. Chemical Society Reviews. 2012; 41: 2885-911.

144. Cohen-Sela, E., Chorny, M., Koroukhov, N., Danenberg, H. and Golomb, G. 2009. A new double emulsion solvent diffusion technique for encapsulating hydrophilic

molecules in PLGA nanoparticles. *Journal of Controlled Release*. 133, 2 (2009), 90–95.

145. Makadia, H. and Siegel, S. 2011. Poly Lactic-co-Glycolic Acid (PLGA) as Biodegradable Controlled Drug Delivery Carrier. *Polymers*. 3, 3 (2011), 1377–1397.

146. Hermanson, Greg T. 2013 Bioconjugate Techniques, Academic Press, London

147. Moura CC, Segundo MA, Neves JD, Reis S, Sarmento B. Co-association of methotrexate and SPIONs into anti-CD64 antibody-conjugated PLGA nanoparticles for theranostic application. Int JNanomedicine. 2014;9:4911–4922.

148. Andreas, K., Zehbe, R., Kazubek, M., Grzeschik, K., Sternberg, N., Bäumler, H., Schubert, Sittinger, H. M. and Ringe, J. 2011. Biodegradable insulin-loaded PLGA microspheres fabricated by three different emulsification techniques: Investigation for cartilage tissue engineering. *Acta Biomaterialia*. 7, 4 (2011), 1485–1495.

149. Huang X, Brazel CS. On the importance and mechanisms of burst release in matrix-controlled drug delivery systems. Journal of Controlled Release. 2001; 73: 121-36.

150. Zur Mühlen A, Schwarz C, Mehnert W. Solid lipid nanoparticles (SLN) for controlled drug delivery – Drug release and release mechanism. European Journal of Pharmaceutics and Biopharmaceutics. 1998; 45: 149-55.

151. Brigger I, Dubernet C, Couvreur P. Nanoparticles in cancer therapy and diagnosis. Advanced Drug Delivery Reviews. 2002; 54:6 31-51.

152. Jain, R. 2000. The manufacturing techniques of various drug loaded biodegradable poly(lactide-co-glycolide) (PLGA) devices. *Biomaterials*. 21, 23 (2000), 2475–2490.

153. Ley K, Laudanna C, Cybulsky MI, Nourshargh S. Getting to the site of inflammation: the leukocyte adhesion cascade updated. Nat Rev Immunol. 2007;7:678–89.

154. Palomba R, Parodi A, Evangelopoulos M, Acciardo S, Corbo C, de Rosa E. et al. Biomimetic carriers mimicking leukocyte plasma membrane to increase tumor vasculature permeability. Sci Rep. 2016;6:34422.

155. Wilhelm S, Tavares AJ, Dai Q, Ohta S, Audet J, Dvorak HF. et al. Analysis of nanoparticle delivery to tumours. Nature Reviews Materials. 2016;1:16014.

156. Lum, H., Roebuck, K. A. Oxidant stress and endothelial cell dysfunction. Am. J. Physiol., Cell Physiol., 280 (2001), pp. C719-C741.

157. Fortuno, A., Jose, G. S., Moreno, M. U., et al. Oxidative stress and vascular remodeling. Exp. Physiol., 90 (2005), pp. 457-462.

158. Griendling, K. K., Sorescu, D., Ushio-Fukai M. NAD(P)H oxidase: role in cardiovascular biology and disease. Circ. Res., 86 (2000), pp. 494-501.

159. Sorescu, D., Szocs, K., Griendling K. K. NAD(P)H oxidases and their relevance to atherosclerosis. Trends Cardiovasc. Med., 11 (2001), pp. 124-131.

160. Dulmovits, B. M., Herman, I, M. Microvascular remodeling and wound healing: A role for pericytes Int. J. Biochem. Cell Biol., 44 (2012), pp. 1800-1812

161. Baskaran H, Toner M, Yarmush ML, Berthiaume F. Poloxamer188 improves capillary blood flow and tissue viability in a cutaneous burn wound. J Surg Res 2001;101:56–61.

162. Bao P, Kodra A, Tomic-Canic M, Golinko MS, Ehrlich HP, Brem H. 2009. The role of vascular endothelial growth factor in wound healing. *J. Surg. Res.* 153: 347–58.

163. Hamed S, Bennett CL, Demiot C, Ullmann Y, Teot L, Desmoulière A. Erythropoietin, a novel repurposed drug: an innovative treatment for wound healing in patients with diabetes mellitus. Wound Repair Regen. 2014;22:23–33.

164. Kay J, Chow WH, Chan TM. et al. *N*-acetylcysteine for prevention of acute deterioration of renal function following elective coronary angiography and intervention: a randomized controlled trial. *JAMA.*2003;289:553-558

165. Tepel M, van Der Giet M, Schwarzfeld C, Laufer U, Liermann D, Zidek W. Prevention of radiographic-contrast-agent-induced reductions in renal function by acetylcysteine. *N Engl J Med.*2000;343:180-184.

166. Moura CC, Segundo MA, Neves JD, Reis S, Sarmento B. Co-association of methotrexate and SPIONs into anti-CD64 antibody-conjugated PLGA nanoparticles for theranostic application. Int JNanomedicine. 2014;9:4911–4922.

167. Gogali, A., Charalabopoulos, K., Zampira, I. *et al.*Soluble adhesion molecules E-cadherin intercellular adhesion molecule-1 and E-selectin as lung cancer biomarkers. Chest, 138 (2010), pp. 1173-1179.

168. Hossain Saad MZ, Jahan R, Bagul U (2012) Nanopharmaceuticals: a new perspective of drug delivery system. Asian J Biomed Pharm Sci 2(14):11–20.

169. Wang, NX.; von Recum, HA (2011). "Affinity-Based Drug Delivery". *Macromol Biosci 11: 321–332. Doi: 10. 1002/mabi.201000206.*

170. Booth, R. & Kim, H. Characterization of a microfluidic in vitro model of the blood-brain barrier (mBBB). *Lab Chip* 12, 1784–1792 (2012).

171. McKee, C. A. & Lukens, J. R. Emerging roles for the immune system in traumatic brain injury. *Front. Immunol.* **7**, 556 (2016).

172. Tomlinson, D. R. & Gardiner, N. J. Glucose neurotoxicity. *Nature Rev. Neurosci.* **9**, 36–45 (2008).

173. Harada, K., Kamiya, T. & Tsuboi, T. Gliotransmitter release from astrocytes: functional, developmental, and pathological implications in the brain. *Front Neurosci.* **9**, 499, (2015).

174. Haorah, J., Knipe, B., Leibhart, J., Ghorpade, A., & Persidsky, Y. (2005). Alcohol-induced oxidative stress in brain endothelial cells causes blood-brain barrier dysfunction. *Journal of Leukocyte Biology, 78*(6), 1223–1232. DOI: 10.1189/jlb.0605340.

175. Maskarinec SA, Wu G, Lee KY (2005) Membrane sealing by polymers. Ann N Y Acad Sci 1066: 310–320.

176. Murphy AD, McCormack MC, Bichara DA, Nguyen JT, Randolph MA, et al. (2010) Poloxamer 188 protects against ischemia-reperfusion injury in a murine hind-limb model. Plast Reconstr Surg 125: 1651–1660.

177. Walters TJ, Mase VJ, Roe JL, Dubick MA, Christy RJ (2011) Poloxamer-188 Reduces Muscular Edema After Tourniquet-Induced Ischemia-Reperfusion Injury in Rats. The Journal of Trauma: Injury, Infection, and Critical Care 70: 1192–1197.

178. Gu JH, Ge JB, Li M, Xu HD, Wu F, Qin ZH. Poloxamer 188 protects neurons against ischemia/reperfusion injury through preserving integrity of cell membranes and blood brain barrier. *PLoS One* (2013) **8**: e61641. doi: 10.1371/journal.pone.0061641.

179. Elgindy EA, El-Huseiny AM, Mostafa MI, Gaballah AM, Ahmed TA. N-acetyl cysteine: could it be an effective adjuvant therapy in ICSI cycles?. A preliminary study. Reprod Biomed Online. 2010;20(6):789–796.

180. Mokhtari, V., Afsharian, P., Shahhoseini, M., Kalantar, S. M., and Moini, A. (2017). A review on various uses of N-acetyl cysteine. *Cell J.* 19, 11–17. doi: 10.22074/cellj.2016.4872.

181. McNeil, E., Capaldo, C. T. & Macara, I. G. Zonula occludens-1 function in the assembly of tight junctions in Madin-Darby canine kidney epithelial cells. *Mol. Biol. Cell* **17**, 1922–1932 (2006).

182. Lee, B. & Newberg, A. Neuroimaging in traumatic brain injury. *NeuroRx* **2**, 372–383 (2005).

183. Bittner S, Ruck T, Schuhmann M. K, et al. Endothelial TWIK-related potassium channel-1 (TREK1) regulates immune-cell trafficking into the CNS. Nat Med. 2013; 19:1161–1165.

184. Toh YC, Zhang C, Zhang J, Khong YM, Chang S, et al. A novel 3D mammalian cell perfusion-culture system in microfluidic channels. Lab Chip. 2007; 7:302–309.

185. Ruck, T., Bittner, S. & Meuth, S.G. *Blood-brain barrier modeling: challenges and perspectives*. *Neural Regen. Res.* 10, 889–891 (2015).

186. Davis GE, Koh W, Stratman AN. Mechanisms controlling human endothelial lumen formation and tube assembly in three-dimensional extracellular matrices. Birth Defects Res C Embryo Today. 2007; 81:270–285.

187. Bayly, P.V., et al.: Magnetic resonance measurement of transient shear wave propagation in a viscoelastic gel cylinder. J. Mech. Phys. Solids **56**(5), 2036–2049 (2008).

188. Zhang, L. et al. Nanoparticles in medicine: therapeutic applications and developments. *Clin. Pharmacol. Ther.* 83, 761–769 (2008).

189. Salvador-Morales, C., Zhang, L., et al. Immunocompatibility properties of lipid-polymer hybrid nanoparticles with heterogeneous surface functional groups. *Biomaterials* 30, 2231–2240 (2009).

190. Owens, D. E. III & Peppas, N. A. Opsonization, biodistribution, and pharmacokinetics of polymeric nanoparticles. *Int. J. Pharm.* 307, 93–102 (2006).

191. Chu et al., 2011. Ultrafine PEG-coated poly (lactic-co-glycolic acid) nanoparticles formulated by hydrophobic surfactant-assisted one-pot synthesis for biomedical applications. Nanotechnology, 22 (2011), p. 18560.

192. Yoo J. W, Chambers E, Mitragotri S. Factors that control the circulation time of nanoparticles in blood: challenges, solutions, and future prospects. *Curr Pharm Des*. 2010;16(21):2298–2307.

193. Wang J, Sui M, Fan W. Nanoparticles for tumor-targeted therapies and their pharmacokinetics. *Curr Drug Metab*. 2010;11(2):129–141.

194. Rafiei, P. & Haddadi, A. Docetaxel-loaded PLGA and PLGA-PEG nanoparticles for intravenous application: Pharmacokinetics and biodistribution profile. *Int. J. Nanomedicine* 12, 935–947 (2017).

195. Li, Y., et al. Targeted delivery of intranasally administered nanoparticles-mediated neuroprotective peptide NR2B9c to brain and neuron for treatment of ischemic stroke. Nanomedicine (2018), 10.1016/j.nano.2018.10.013.

196. Naik, P. & Cucullo, L. *In vitro* blood–brain barrier models: current and perspective technologies. *Journal of Pharmaceutical Sciences* 101, 1337 (2012).

197. Gumbleton, M. & Audus, K. L. Progress and limitations in the use of *in vitro* cell cultures to serve as a permeability screen for the blood-brain barrier. *J. Pharm. Sci*, 90, 1681–1698 (2001).

198. Bickel U. How to measure drug transport across the blood-brain barrier. *NeuroRx* 2005; **2**: 15–26.

199. Del Razo, M. J. *et al*. Mourad, Randall J. Leveque, David G. Cook. Computational and *in vitro* studies of blast-induced blood-brain barrier disruption. *J. Sci. Comput.* **38**, 347–374, https://doi.org/10.1137/15M1010750 (2006).

200. Abbott, N. J., Patabendige, A. A., Dolman, D. E., Yusof, S. R. & Begley, D. J. Structure and function of the blood-brain barrier. *Neurobiol. Dis.* **37**, 13–25 (2010).

201. Antoine, E. E., Vlachos, P. P. & Rylander, M. N. Review of collagen I hydrogels for bioengineered tissue microenvironments: characterization of mechanics, structure, and transport. *Tissue Eng. Part B Rev.* **20**, 683–696 (2014).

202. Drury J.L., and Mooney D.J. Hydrogels for tissue engineering: scaffold design variables and applications. Biomaterials 24,**4337, 2003

203. Sykova E, Nicholson C. Diffusion in brain extracellular space. Physiol Rev. 2008;88(4):1277–340.

204. DeStefano, J. G., Jamieson, J. J., Linville, R. M., and Searson, P. C. (2018). Benchmarking in vitro tissue-engineered blood-brain barrier models. *Fluids Barriers CNS* 15:32. doi: 10.1186/s12987-018-0117-2

205. Yamamura N., Sudo R., Ikeda M., and Tanishita K. Effects of the mechanical properties of collagen gel on the *in vitro* formation of microvessel networks by endothelial cells. Tissue Eng 13,**1443, 2007

206. Kreger S.T., Bell B.J., Bailey J., Stites E., Kuske J., Waisner B., et al. Polymerization and matrix physical properties as important design considerations for soluble collagen formulations. Biopolymers93,**690, 2010

207. Wolf K., Alexander S., Schacht V., Coussens L.M., von Andrian U.H., van Rheenen J., et al. Collagen-based cell migration models *in vitro* and *in vivo*. Sem Cell Dev Biol 20,**931, 2009

208. Kinney JP, et al. Extracellular sheets and tunnels modulate glutamate diffusion in hippocampal neuropil. J Comp Neurol. 2013;521(2):448–64.

209. Thorne RG, Nicholson C. In vivo diffusion analysis with quantum dots and dextrans predicts the width of brain extracellular space. Proc Natl Acad Sci USA. 2006;103(14):5567–72.

210. Muelbl M. J, Slaker M. L, Shah A. S, et al. (2018). Effects of mild blast traumatic brain injury on cognitive- and addiction-related behaviors. Sci Rep 8:9941.

211. Fleminger, S. & Ponsford, J. Long term outcome after traumatic brain injury. *BMJ* 331, 1419–1420, https://doi.org/10.1136/bmj.331.7530.1419 (2005).

212. Vaishnavi, S., Rao, V. & Fann, J. R. Neuropsychiatric problems after traumatic brain injury: unraveling the silent epidemic. *Psychosomatics* 50, 198–205, https://doi.org/10.1176/appi.psy.50.3.198 (2009).

213. Ashman, T. A. *et al*. Psychiatric challenges in the first 6 years after traumatic brain injury: cross-sequential analyses of Axis I disorders. *Archives of physical medicine and rehabilitation* 85, S36–42 (2004).

214. Fann, J. R. *et al*. Psychiatric illness following traumatic brain injury in an adult health maintenance organization population. *Archives of general psychiatry* 61, 53–61, https://doi.org/10.1001/archpsyc.61.1.53 (2004).

215. Endo, H., *et al.* Glucose starvation induces LKB1-AMPK-mediated MMP-9 expression in cancer cells. Sci. Rep., 8 (1) (2018), p. 10122

216. Gonzalez-Reyes, S., Guzman-Beltran, S., et al. Curcumin pretreatment induces Nrf2 and an antioxidant response and prevents hemin-induced toxicity in primary cultures of cerebellar granule neurons of rats. *Oxid. Med. Cell Longev.* 2013, 801418 (2013).

BIOGRAPHY

Edidiong Inyang was born in Ukwok, Ikono local government area (LGA), Akwa Ibom State, Nigeria. He came to the states in few years after completing his secondary school at Etinan Institute, Etinan LGA, Akwa Ibom State, Nigeria. He attended the Fort Valley State University (FVSU), Fort Valley, GA. From January 2010 to December 2013 where he got his Bachelor of Science (BSc) with a major in Biology. He went on to receive his Master of Science (MSc) in Entomology from Florida Agricultural and Mechanical University, Tallahassee, FL on August 2015. In August 2015, he entered the Ph.D. program at the University of Texas at Arlington (UTA), Arlington, TX, where he received Ph.D. in Biomedical Engineering on August 2019. He was partly sponsored by UTA-Louis Stokes Alliances for Minority Participation (LSAMP)/NSF grants and Office of Naval Research (ONR) grant.